Determination of Natural Radioactivity Concentrations in Soil: a comparative study of Windows and Full Spectrum Analysis

by

Katse Piet Maphoto

Thesis submitted in partial fulfillment of the
requirements for the M.Sc. degree in Physics at the
University of the Western Cape

August 2004

Supervisor: Prof. R. Lindsay

Co-supervisor: Dr. R.T. Newman (iThemba LABS)

Declaration

I, the undersigned, declare that the work contained in this thesis is my own original work and has not previously in its entirety or in part been submitted at any university for a degree.

Signature:…….

Date: ……

Acknowledgements

I am greatly indebted to the following people who made this thesis possible:

Prof. Robbie Lindsay, supervisor, for the help in financing my studies and guiding me every step of the way, especially with challenging aspects such as programming.

Dr. Richard Thomas Newman, co-supervisor, for the guidance and suggestions especially during the writing up of the thesis.

iThemba LABS, for financing, and granting me the opportunity to do my study with them, and to all the staff from the library to the Human Resource for their support.

To my parents, **Magate le Baboloki**, for always being on my side whenever I needed them and for their love and patience, and my Family for their support and endless love.

Environmental Radioactivity Group**: Dawid de Villiers, Angelo Joseph**, **Raphael Damon and Lerato Sedumedi** (former Technical Officer); for their helpful discussions.

To **Prof. Rob de Meijer**, from the Kernfysisch Versneller Instituut (KVI) in the Netherlands, for helpful discussions and suggestions.

To **Peane Maleka**, former masters student at the iThemba LABS, for introducing me to the basic concepts of experimental methodologies.

UWC Physics department for making me feel at home when I felt like a stranger, and all my colleagues for their encouragement

Finally, thanks to the Almighty God, the Creator of the Universe, the Alpha and Omega, for keeping me alive and kicking all the way.

Determination of Natural Radioactivity Concentrations in Soil: a comparative study of Windows and Full Spectrum Analysis

Katse Piet Maphoto

Abstract

In this study, two methods of analysing activity concentrations of natural radionuclides (^{238}U, ^{232}Th and ^{40}K) in soil are critically compared. These are the Window Analysis (WA) and Full Spectrum Analysis (FSA). In the usual WA method, the activity concentrations are determined from the net counts of the windows set around individual γ-ray peaks associated with the decay of ^{238}U, ^{232}Th and ^{40}K. In the FSA method, the full energy spectrum is considered and the measured spectrum is described as the sum of the three standard spectra (associated with ^{238}U, ^{232}Th and ^{40}K, respectively), each multiplied by an unknown concentration. The concentrations are determined from the FSA and correspond to the activity concentrations of ^{238}U, ^{232}Th and ^{40}K in the soil. The standard spectra derived from separate calibration measurements using the HPGe detector, represents the response of the HPGe to a Marinelli sample beaker containing an activity concentration of 1 Bq/kg.

A χ^2 -minimisation procedure (for the FSA method) is used to extract the accurate activity concentrations. The results of this technique (FSA) were obtained and compared with the conventional (WA) method of analysis. Although a good correlation was found between results from these methods, the disadvantage was with the self-absorption effects, which result into poor fit (especially at the continuum). This proved to have had an impact on the measured results for FSA. This phenomenon was carefully studied and a recommendation is made in the conclusion.

Five samples having a range of activity concentrations (relative and absolute) and densities were analyzed as part of this study. In one case (that for the (stearic acid + ^{232}Th) sample) the absolute activity concentration of ^{232}Th in the sample was known. The samples were measured

for longer times (about 8 to 10 hours) and short times (about 1 hour). Activity concentrations were then calculated from each spectrum using WA and FSA. For the long measurements the ratio of WA-determined concentrations to FSA-determined concentrations varied between about 1.0 and 1.3 for ^{238}U, between 1.0 and 1.6 for ^{232}Th, and between 0.97 and 1.0 for ^{40}K. The corresponding ratio for short measurements varied between 1.0 and 1.2 for ^{238}U, between 0.7 and 1.1 for ^{232}Th, and between 0.9 and 1.0 for ^{40}K

This is with the exception of the low activity sample of the West coast sample, which gave the ratios ranging from 0.97 to 1.6 in the case of long measurement and 1.4 to 7.4 in case of the short measurements.

In the case of the (stearic acid + ^{232}Th) sample the WA and FSA determined activity concentrations deviated from the expected concentrations by 9% and 21 %, respectively.

This study demonstrated that the FSA technique could be useful for extracting activity concentrations from high-resolution gamma ray spectra in a relatively straightforward and convenient way provided that proper consideration is given to effects associated with sample volume and density in relation to the sources used to generate standard spectra.

Table of Contents

List of Tables

LIST OF FIGURES

Chapter 1

1. Introduction

In 1895, the German physicist Wilhelm Roentgen identified penetrating radiation, which produced fluorescence,[1] and which he named X-rays. In 1896 two months later, Henri Becquerel discovered that penetrating radiation, later classified as α, β and γ rays, were given off in the radioactive decay of uranium and thus opened a new field of study of radioactive substances and radiations they emit [Sha72].

Rutherford and Soddy were the first to suggest that radioactive atoms disintegrate into lighter structures as they emit radiation. This suggestion received powerful support with the discovery that the α-particle was just an ionised atom of the element helium. Many of the newly discovered elements were found in various fractions of uranium ores, and this, the heaviest naturally occurring element, was soon suspected to be the parent substance [Ral72]. It is presently known that uranium consists naturally of a mixture of ^{238}U (99.27%), ^{235}U (0.72%), and ^{234}U (0.006%); thorium and potassium were also identified as the radioactive parents with some decay products. Refer to Figures 1.1, 1.2 and 1.3 for the decay processes of natural radionuclides ^{238}U, ^{232}Th and ^{40}K into their daughter nuclei.

Soils are naturally radioactive, primarily because of their mineral content. The main radionuclides are ^{238}U, ^{232}Th and their decay products, and ^{40}K. The radioactivity varies from one soil type to the other depending on the mineral makeup and composition [Dra03]. The objective in the measurement of the radioactivity in soil is to asses the radionuclide concentrations; and these concentrations may be used to characterise substances and relate the

[1]The emission of electromagnetic radiation, especially of visible light, stimulated in a substance by the absorption of incident radiation and persisting only as long as the stimulating radiation is continued.

radiometric properties to physical properties of the material. This may be of use in mineral separation for example.

1.1 The atomic nuclei and radioactivity: an overview

This section describes the nature of atoms, their building blocks and the nature of the forces playing a role in it. In the fourth century B.C. the Greek philosopher Democritus believed that each kind of material could be subdivided into smaller and smaller bits until the limit beyond which no further division was possible. These building blocks of matter invisible to the naked eye were referred to as atoms. This speculation was confirmed by experimental scientists (Dalton, Avagadro, Faraday) over 2000 years later. Once the classification and kind of atoms have been studied according to the rules governing their combination in matter by the chemists, the next step was to study the fundamental properties of an atom of various elements. This kind of atomic physics led to the discovery of radioactivity of certain species of atoms [Kra88]. Rutherford then used these radiations of atoms as probes of the atoms themselves. In 1911 he then proposed the existence of the atomic nucleus, which was experimentally confirmed by Geiger and Marsden. A new branch of science, which is now called nuclear physics, was then born. This branch of physics is dedicated to studying matter at its fundamental level.

A nucleus X, is made up of Z protons and N neutrons (nucleons), with the notation ${}^{A}_{Z}X_{N}$, with atomic mass number A = Z + N, where X is a nuclide symbol. The mass of a nucleus is less than the sum of the individual masses of the protons and neutrons, which constitute it. The difference is a measure of the nuclear binding energy, which holds the nucleus together. This is the energy required to break it into separate neutrons and protons. If the nuclear radius is R, then the corresponding volume, $(4/3)\pi R^3$ is found to be proportional to A. This relationship is expressed in inverse form as

$$R = R_0 A^{1/3} \tag{1.1}$$

with the value of $R_0 \approx 1.2 \times 10^{-15}$m

The description of the nucleus can be understood with the aid of different models. Two of these are the liquid drop model and the shell model [Bei87, Eva55].

1.1.1 Radioactive Decay

Protons are positively charged and repel one another electrically. Therefore an excess of neutrons which produce only an attractive force, is required for stability, thus leading to N > Z for stable nuclei. There is a limit to the ability of neutrons to prevent the disruption of the nucleus by the Coulomb repulsion. This phenomenon therefore leads to instability of nuclei. The instability can also be attributed to the unstable configurations due to the filling of quantum states by the nucleon [Hew85].

1.1.2 Decay modes

Because of their instability, nuclei decay by α, β, or γ emissions. Many naturally occurring, heavy nuclei, with $82 < Z \leq 92$ decay by α emission in which the parent nucleus loses both mass and charge (A, Z) [Ral72]. The α (^{4}He-nucleus) type reaction can be represented as

$$ {}^{A}_{Z}X \rightarrow {}^{A-4}_{Z-2}Y + {}^{4}_{2}\alpha + \gamma \qquad (1.2) $$

where X represents a chemical symbol of the parent atom and Y that of the daughter. In some emissions there is no γ emission.

In β^- particle emission, a neutron (in the nucleus) is converted into a proton, electron and an anti-neutrino.

$$ {}^{1}_{0}n \rightarrow {}^{1}_{1}p + {}^{0}_{-1}\beta \; + \bar{\nu}_e \qquad (1.3) $$

Although free electrons do not exist inside the nucleus, a β particle originates there and must pass the nuclear potential barrier to escape [Ral92]. This leads to the equation

$$ {}^{A}_{Z}X \rightarrow {}^{A}_{Z+1}Y + {}^{0}_{-1}\beta \quad + \gamma + \overline{\nu}_e \,. \tag{1.4} $$

As in the α particle case, the atomic mass number and atomic number are conserved. The γ term allows for the possibility that a daughter nucleus will be formed in an excited state, while some transitions go directly to the ground state. The β^- particle emission is an example of the radioactive decay of a nuclide with neutron excess. In this case a neutron is converted to a proton according to equation (1.3).

The neutron-deficient nuclei emit a positron as they go to stability by

$$ {}^{1}_{1}p \rightarrow {}^{1}_{0}n + {}^{0}_{1}\beta^{+} + \nu_e \tag{1.5} $$

and the transformation is now

$$ {}^{A}_{Z}X \rightarrow {}^{A}_{Z-1}Y + {}^{0}_{1}\beta^{+} + \gamma + \nu_e \tag{1.6} $$

The energy of α and γ- radiation is discrete and well defined, whilst β emission gives β's with a continuous spectrum due to the varying amount of energy taken away by the neutrino.

In the case of electron capture (EC) the neutron-deficient nuclei must decay by a p → n conversion, but have daughter products whose mass is greater than the maximum acceptable for positron emission. Therefore these nuclei can only decay by the capture of one of the orbital electrons. The atomic number is then reduced by one unit, due to the negative charge acquired by the nucleus, and thus yielding the same daughter that would have been produced by the positron emission. Figure 1.1 in section 1.3.1 presents the decay scheme of ^{40}K in which

the electron capture (EC) is in competition with positron emission; in addition to β^- decay to ^{40}Ca, the decay to ^{40}Ar has two competing modes of decay, that is β^+ and EC. The electron capture is represented by the type of reaction

$$ {}^{A}_{Z}X + {}^{0}_{-1}e^{-} \rightarrow {}^{A}_{Z-1}Y + \gamma + \nu_e \, . \qquad (1.7) $$

1.1.3 Decay rates

The radioactive decay rate of a nucleus is measured in terms of the decay constant λ, which is the probability per unit time that a given nucleus will decay, and this is related to its half-life[2]. Each radioactive nucleus has its own characteristic half-life. If there are N radioactive nuclei in a sample, the rate of decay will then be given by

$$ \frac{dN}{dt} = -\lambda N \qquad (1.8) $$

where the minus sign indicates that N is decreasing with time. The solution of this equation is

$$ N(t) = N(0)e^{-\lambda t} \qquad (1.9) $$

with N(0) being the number of nuclei present at t = 0. The half-life, $t_{1/2}$, may be expressed in terms of λ from equation (1.13) as

$$ t_{1/2} = \frac{\ln 2}{\lambda} \, . \qquad (1.10) $$

The activity A is defined as the number of decaying nuclei per unit time and it can be represented by

[2] The time needed for half of the radioactive nuclei of any given quantity to decay

$$A \equiv -\frac{dN}{dt} = \lambda N \tag{1.11}$$

The unit is the Becquerel (Bq) with the historical unit being the Curie (Ci) where: 1 Ci = 3.7 x 10^{10} decays per second and 1 Bq = 1 decay per second. In this study the results are given in terms of activity concentrations, which are expressed in units of Bq/kg.

1.2 Types of environmental radioactivity

Radioactivity on the earth can be categorized according to three different types, namely those of primordial, cosmogenic and anthropogenic nature [Mer97].

- **Primordial radionuclides** – these have half-lives sufficiently long that they have existed since the formation of the earth, and from the radioactive decay of these, secondary radionuclides are produced (e.g. ^{40}K, ^{232}Th, and ^{238}U).

- **Cosmogenic radionuclides** – primary radiation (protons and other heavier nuclei), originating from outer space, called cosmic rays continuously bombard stable atoms in the atmosphere and create radionuclides (e.g. ^{22}Na, ^{7}Be and ^{14}C). When cosmic rays strike the atmosphere, they produce a nuclear cascade or a shower of secondary particles. Most of these are eventually stopped before they reach the surface of the earth except for energetic muons (μ), and neutrons (n), which may penetrate all the way into the earth.

- **Anthropogenic radionuclides** – these are man-made radionuclides released into the environment through, for example, the testing of nuclear weapons, nuclear reactor accidents (e.g. Chernobyl) and in the radio-isotope manufacturing industry (^{137}Cs, ^{90}Sr and ^{131}I).

1.3 Review of primordial radioactivity

Some of primordial radionuclides that now exist are those that have half-lives comparable to the age of the Earth (e.g. ^{238}U, ^{232}Th and ^{40}K). Naturally occurring radionuclides can be divided into those that occur singly and those that are components of chains of radioactive decay.

1.3.1 Decay series of natural radionuclides

In this study the focus is on gamma-ray emitting daughter nuclei in the decay series of ^{2238}U, ^{232}Th and ^{40}K. The decay series of ^{238}U and ^{232}Th are characterised more or less by the initial part dominated by alpha decay and a part dominated by gamma-ray emission. This contributes to the difficulty in the radioactive measurements [Hen01]. During a series of radioactive decays, the original radioactive (parent) nucleus N_1 decays to another radioactive (daughter) nucleus until the end of the series, where a stable nucleus is formed (^{206}Pb in the case of ^{238}U series and ^{208}Pb for ^{232}Th), see Figures 1.2 and 1.3. The number of parent nuclei N_1 decreases according to the form

$$dN_1 = -\lambda_1 N_1 dt \qquad (1.12)$$

as discussed in section 1.1.3. The number of daughter nuclei increases as a result of the decay of the parent nuclei and decreases as a result of the decay of its own, which leads to

$$dN_2 = (\lambda_1 N_1 - \lambda_2 N_2)dt \qquad (1.13)$$

After a long time, equilibrium is reached where the production and the decay rates in the series are the same [Kra88] so that $dN_2 = 0$. Therefore the activities of all the radionuclides in the chain must be equal

$$(\lambda_1 N_1 = \lambda_2 N_2 = \lambda_3 N_3), \qquad (1.14)$$

and this phenomenon is referred to as secular equilibrium. This is usually a very accurate assumption except when daughter nuclei escape, for example when the radioactive gas ^{222}Rn escapes in the decay series of ^{238}U.

Sir Humphry Davy discovered the potassium element in 1807. The element is the seventh most abundant and makes up about 2.4% by weight of the earth's crust. Ordinary potassium is composed of three isotopes, one of which is ^{40}K (0.0118%); a radioactive isotope with a half-life of 1.28 x 10^9 years [www01], see Figure 1.1.

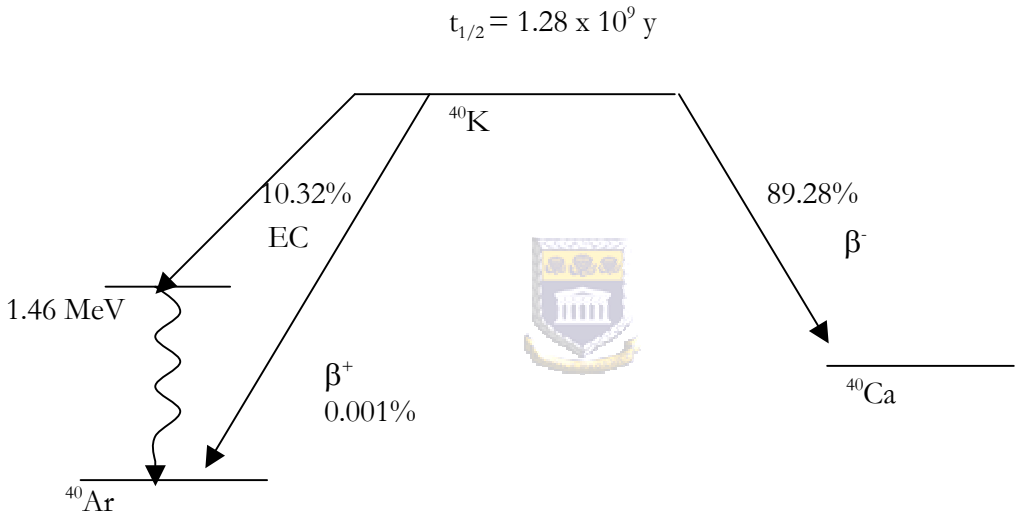

Figure 1.1 ^{40}K decays by β^+ and electron capture to ^{40}Ar and by β to ^{40}Ca.

The above figure shows two competing decay modes (β^+-decay and EC) to the stable ^{40}Ar, while on the other hand there is 89% chance of decaying by β^- to ^{40}Ca. The half-life ($t_{1/2}$) for this nuclide is 1.28 x 10^9 years.

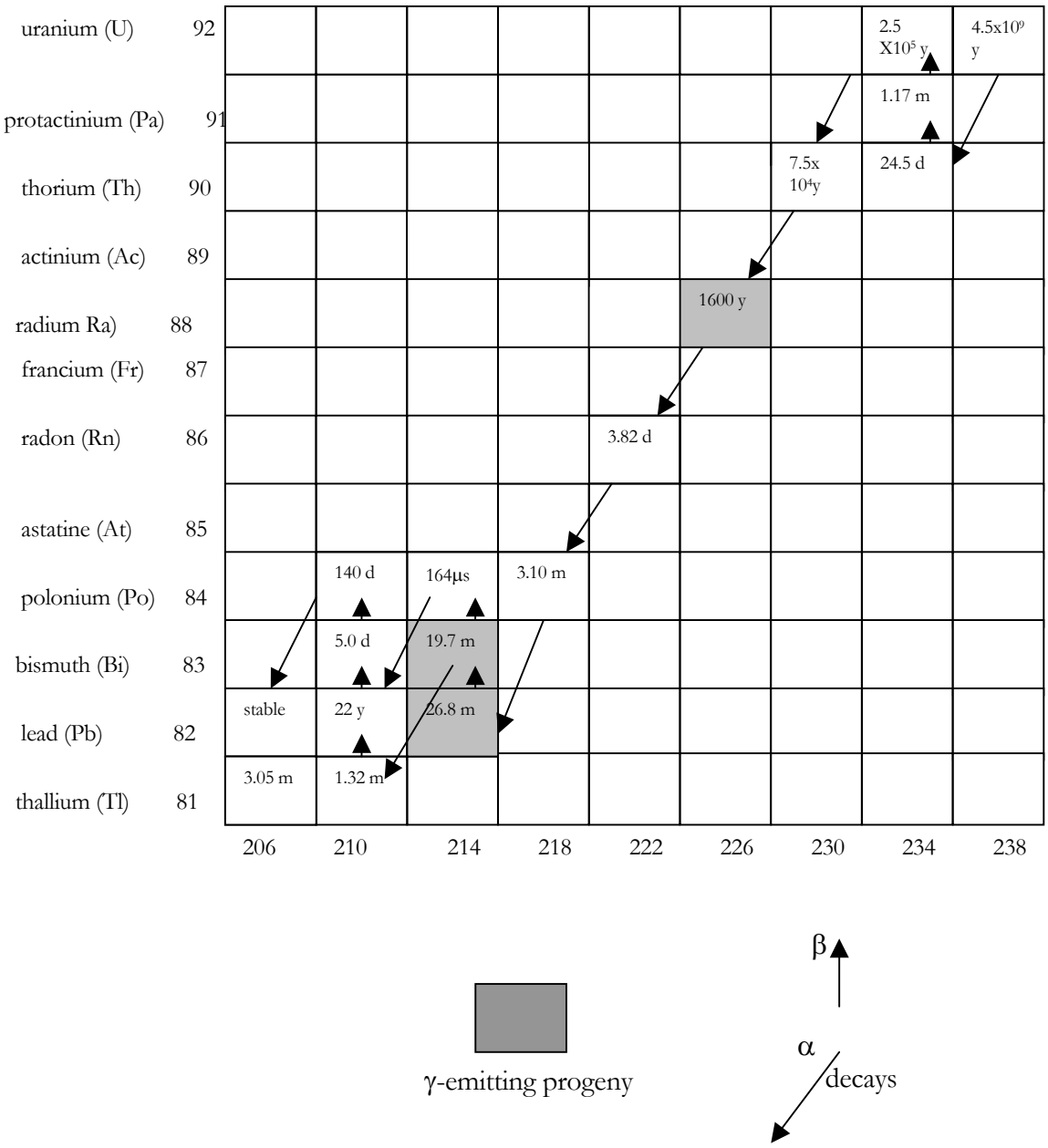

Figure 1.2: A Z-A Plot indicating how the ^{238}U nucleus decays, the half-lives for the respective nuclides are indicated.

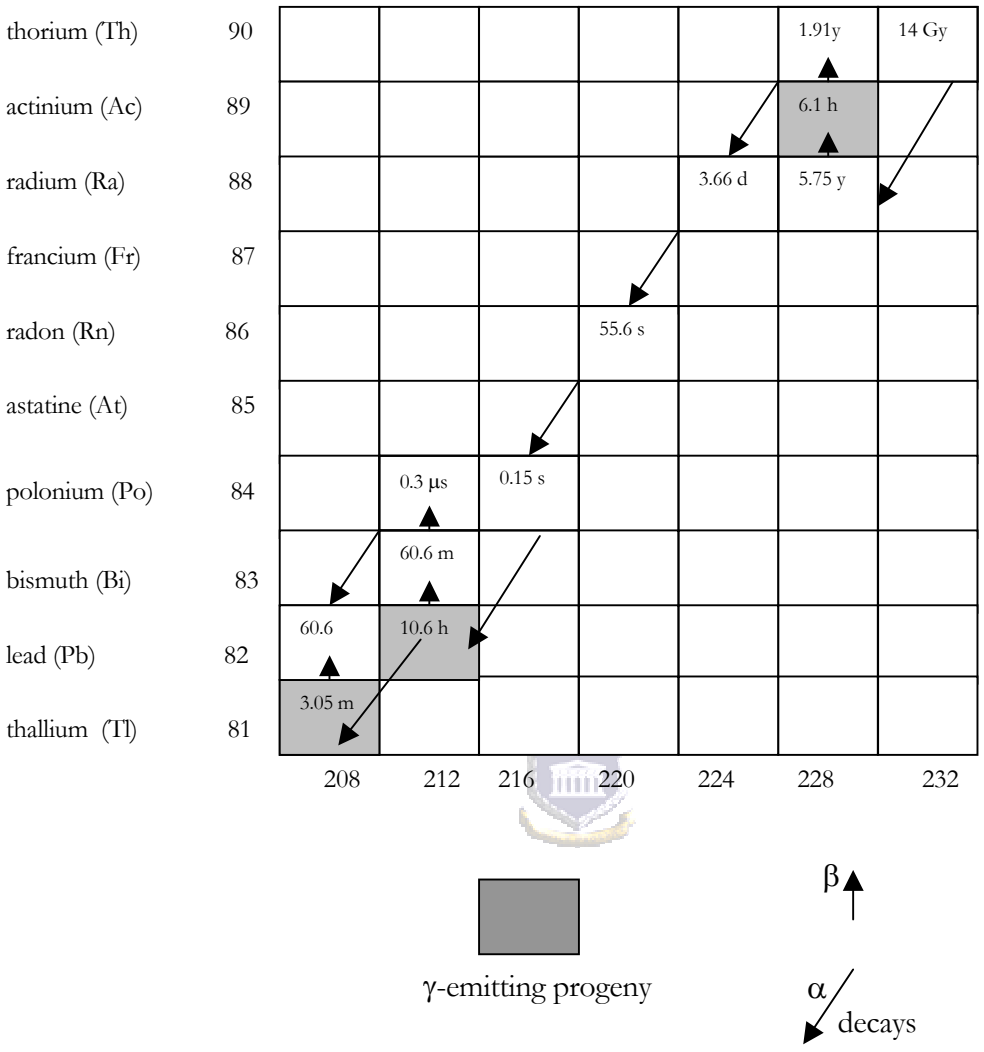

Figure 1.3: A Z-A Plot indicating how the ^{232}Th nucleus decays, the half-lives for the respective nuclides are indicated.

Most of the radioactivity associated with uranium in nature is due to its progeny that are left behind in mining and milling. The gamma radiation detected by exploration geologists looking for uranium actually comes from associated elements such as radium (^{226}Ra) and bismuth (^{214}Bi), which over time have resulted from the radioactive decay of uranium. Uranium constitutes about 2 parts per million (ppm[3]) of the Earth's crust [www02]. See Figure 1.2 for the decay process associated with this nuclide.

In the decay series of, for example, ^{238}U, the parent nucleus ^{226}Ra decays to the daughter ^{222}Rn by an α decay, and ^{222}Rn decays further to ^{218}Po and consequently to ^{214}Pb. Since ^{222}Rn is a gas, it might escape the matrix and thus disturbing the secular equilibrium. In this event the activities of the ^{222}Rn progeny will not be the same as their parent's, and this is an indication of a disturbance of the secular equilibrium. Therefore to obtain secular equilibrium samples are generally sealed for the radon not to escape. This implies that the activity concentrations are the same for all members of the decay chain. When secular equilibrium is reached in the decay of ^{238}U or ^{232}Th it means that the activity concentrations of these nuclei can be determined by measuring activity concentration of their γ-emitting progeny. The disturbance of secular equilibrium due to ^{220}Ra (thoron) is less significant due to its short half-life that is 55.6 seconds, implying that the thoron build up will be negligible.

^{232}Th is a naturally occurring, radioactive element discovered in 1828 by the Swedish chemist Jons Jakob Berzelius. It is found in small amounts in most rocks and soils, where it is about three times more abundant than uranium. Soil commonly contains an average of around 6 parts per million (ppm) of this nuclide. The main pathways of exposure are ingestion and inhalation. It was found to be present in the highest concentrations in the pulmonary lymph nodes and lungs, indicating that the principal source of human exposure is inhalation of suspended soil particles [www02]. Figure1.3 shows the decay process of this nuclide.

[3] 1 ppm U =12.25 Bq/kg ^{238}U, 1ppm Th = 4.10 Bq/kg ^{232}Th , 1000ppm = 302 Bq/kg ^{40}K [Mer97]

1.4 Literature review: natural radionuclide activity concentration in soil

Soil consists of mineral and organic matter, water and air arranged in a complicated physiochemical system that provides the mechanical foothold for plants in addition to supplying their nutritive requirements [Mer97]. The inorganic portion of the surface soils may fall into a number of textural classes, depending on the percentage of sand, silt and clay. Sand consists largely of primary minerals such as quartz and has particle size ranging from 60 μm to about 2 mm. Silt consists of particles in the range of 2 to 60 μm, while clay particles are smaller than 2 μm in diameter [Van02a].

The Table 1.1 shows the values of natural radioactivity in typical soil of volume 1 km × 1 km, and 1 m deep. The soil density was assumed to be 1.6 g.cm^{-3}.

Nuclide	Typical crustal activity concentration (Bq/kg)	Mass in 10^6 m^3	Activity in10^6 m^3
^{238}U	25	2800 kg	40 GBq
^{232}Th	40	15200 kg	65 GBq
^{40}K	400	2500 kg	630 GBq
^{226}Ra	48	2.2 g	80 GBq
^{222}Rn	10	14 μg	9.5 GBq

Table 1.1: Amount of naturally occurring radionuclides in typical soil of a volume 1 km × 1 km, and 1 m deep [Van02b].

Substantial amounts of radionuclides are found in the earth's crust. In fact the natural radioactivity is largely responsible for the fact that the interior of the earth is hot and molten [Van02b].

The term radiometric fingerprinting describes the identification of mineral species based on the difference in radionuclide concentrations [Dem97]. In soil measurements a correlation between activity concentrations and grain size has been determined in previous studies. While

^{40}K activity concentration varies slightly with grain size, ^{238}U and ^{232}Th concentrations increased with an increase in grain size [Van02a]. For example, Table 1.2 presents results found in one case of the difference in activity concentrations for ^{238}U and ^{232}Th, which are used to fingerprint the sediments. See also Table 1.3 for an example of radionuclide fingerprinting with regard to different minerals.

Sediment type	^{238}U-series (Bq/kg)	^{232}Th-series (Bq/kg)
Sand (> 63μm)	9.3 ± 0.9	9.7 ± 0.9
Mud(< 63 μm)	46.2 ± 1.9	45.6 ± 1.9

Table 1.2: Characteristic radiometric fingerprints of sand and mud. The values are derived from ^{238}U and ^{232}Th activity concentrations of untreated total samples [Van02a].

1.4.1 Methods used to determine activity concentrations in soil

There are different methods used in the measurements of activity concentrations in soil. These include laboratory-based measurements using γ-ray methods of analysis and in-situ type of measurements. Examples of these methods will be briefly described in section 1.4.3. The focus in this study is on γ-ray measurements in the laboratory, which is based on the principle of interaction of γ-rays with matter, a subject to be discussed in the next section. These interactions need to be well understood in order to clarify results obtained in Chapter 4.

1.4.2 Interaction of gamma rays with matter

There are three primary processes by which γ-rays interact with matter. These are photoelectric absorption, Compton scattering and pair production.

1.4.2.1 Photoelectric absorption

Photoelectric absorption takes place when there is an interaction of a γ-ray photon with one of the bound electrons in an atom as shown in Figure 1.4. All the energy of the photon is transferred to the electron. The electron is ejected from its shell with a kinetic energy E_e, given by:

$$E_e = E_\gamma - E_b \qquad (1.15)$$

where E_γ is the gamma ray energy and E_e the binding energy of the electron in a shell. The atom is left in an excited state with an excess of energy E_b and recovers its equilibrium by de-exciting and thus redistributing its energy between the remaining electrons in the atom. This may result in the release of further electrons from the atom, a process called Auger cascade [Gil95]. A vacancy left by the ejection of the photoelectron may be filled by a higher energy electron falling into it with the emission of characteristic X-rays (as in Figure 1.5).

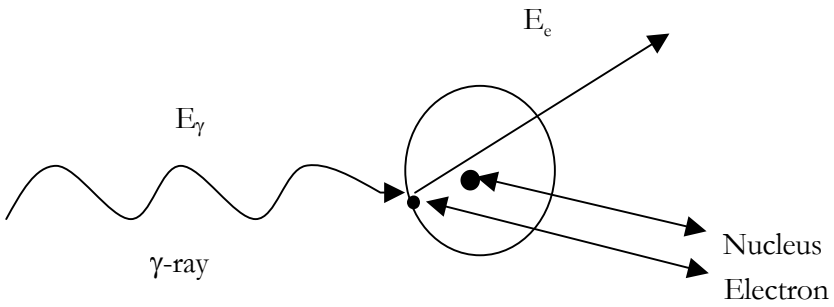

Figure 1.4: A schematic representation of the mechanism of photoelectric absorption, where a γ-ray with energy, E_γ, interacts with a bound electron.

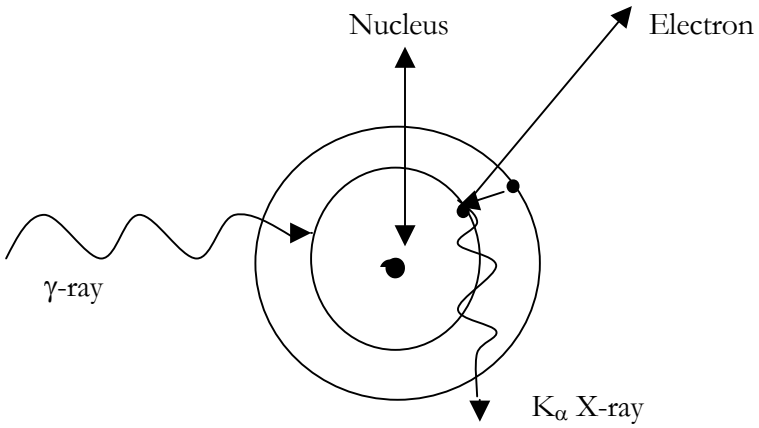

Figure 1.5: The diagrammatic representation of emission of fluorescent X-rays.

The cross-section for photoelectric absorption is dependent on the atomic number Z. This varies somewhat depending on the energy of the photon. At MeV energies; this dependence goes as Z to the 4^{th} or 5^{th} power. The lower the photon energy and the higher the Z of the material in which this photon interacts, the higher the probability of absorption and this becomes an important consideration when it comes to choosing γ-ray detectors [Leo87].

1.4.2.2 Compton Scattering

The incident γ-ray interacts with an electron of an absorbing material. Part of the γ-ray energy is then transferred to this electron. The energy imparted to the recoil electron is given by

$$E_e = E_\gamma - E'_\gamma \tag{1.16}$$

where E_γ is the energy of the incoming photon with E'_γ being the energy of the deflected photon.

or

$$E_e = E_\gamma \{1 - \frac{1}{(1 + E_\gamma [1 - \cos\theta] / m_0 c^2)}\} \quad (1.17)$$

where m_0 is the mass of an electron and c is the speed of light. The incoming γ-ray is then deflected through an angle θ with respect to its original direction. Putting different values of θ into this equation provides a response function with energy. Thus with θ =0°, that is scattering directly forward from the interaction point, E_e is found to be 0 and no energy is transferred to the electron. At the other extreme when the gamma ray is backscattered and θ =180°, the term within curly brackets is still less than 1 so only a proportion of the gamma-ray energy will be transferred to the recoil electron, which gives rise to the Compton edge. This corresponds to maximum energy transferred to recoil electron. At intermediate scattering angles the amount of energy transferred to the electron must be between those two extremes [Gil95]. Figure 1.6 shows Compton scattering:

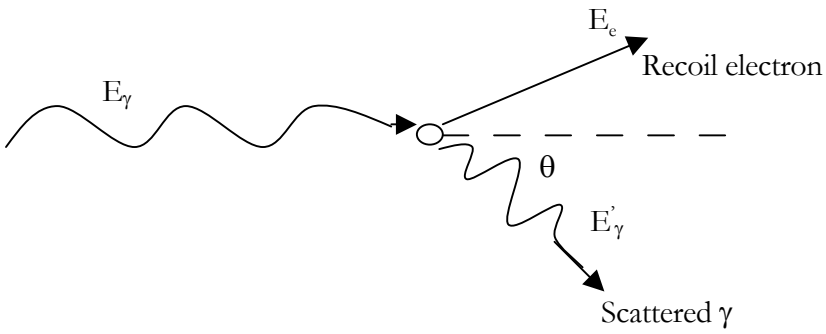

Figure 1.6 : The diagrammatic illustration of the mechanism of Compton scattering.

1.4.2.3 Pair Production

This process, as shown on the diagram in Figure, 1.7 is energetically possible if the γ-ray energy exceeds twice the rest mass of an electron that is 1.02 MeV. The entire energy is converted in the field of an atom into an electron-positron pair. The pair production cross-section does not become significant until E_γ exceeds several MeV. The positron is an anti-electron and after it slows down and almost comes to rest, it will be attracted to an ordinary electron. Annihilation then takes place in which the electron and positron rest masses are converted into two γ-rays, each with energy of 0.511 MeV. These annihilation γ -rays are emitted in opposite directions to conserve momentum and they may in turn interact with the absorbing medium by either photoelectric absorption or Compton scattering [Lil01].

In this study the focus is on γ-rays of energies less than 3 MeV, thus pair production does not play a major role. The cross sections for this process are higher at energies above 3 MeV, as is confirmed in Figure 1.8.

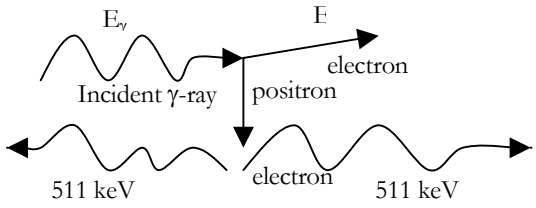

Figure 1.7: The diagrammatic illustration of pair production.

1.4.2.4 Attenuation Coefficients

The attenuation coefficient is defined as a measure of the reduction in the gamma-ray intensity at a particular energy caused by an absorber [Gil95]. Photoelectric interactions are dominant at low energy, Compton scattering at mid-energy ranges while pair production is dominant at high energies. In the low-energy region, discontinuities in the photoelectric curve appear at gamma-ray energies, which correspond to the binding energies of electrons in the various shells of the absorber atom. The edge lying highest in energy corresponds to the K shell electron. For gamma-ray energies slightly above the edge, the photon energy is just sufficient to undergo a photoelectric interaction in which the K electron is ejected from the atom. For gamma rays below the edge this process is no longer energetically possible, and therefore the interaction probability drops abruptly. Similar absorption edges occur at lower energies for the L, M,… electron shells of the atom [Kno79].

The total cross section σ_{tot} for the photon atom interaction may be written as

$$\sigma_{tot} = \sigma_{pe} + \sigma_{pp} + \sigma_{c}\,, \tag{1.18}$$

where σ_{pe} , σ_{pp} and σ_{c} are respectively the cross-sections for photoelectric absorption, pair production and Compton scattering [Cre87].

Present tabulations of the mass attenuation coefficient μ/ρ rely on theoretical values for the total cross section per atom, which is related to μ/ρ according to

$$\mu/\rho\left[\frac{cm^2}{g}\right] = \sigma_{tot}\left[\frac{cm^2}{atom}\right]/(u[g].A) \tag{1.19}$$

u (= 1.67 x 10^{-24} g) is the atomic mass unit and A is the relative atomic mass of the target element.

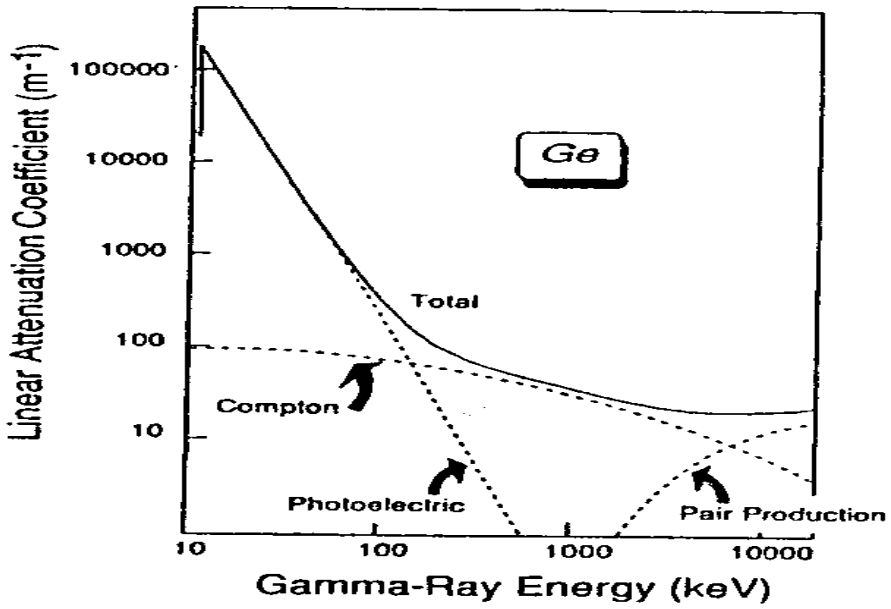

Figure 1.8: The linear attenuation coefficient of germanium and its component parts on a log-log scale [Gil95].

On multiplying the mass attenuation coefficient μ/ρ by the density ρ of the material the result will be the linear attenuation coefficient μ. This phenomenon is an important part of this study, and will therefore be discussed in more detail in the Appendix D under the discussion on self-absorption effects.

1.4.3 Examples of gamma-ray spectrometry systems

- **In-situ**

The successful demonstration of the in-situ γ-ray spectroscopy for the rapid and accurate assessment of radionuclides in the environment has been witnessed over time. This allows for the measurement of γ-ray intensities in the soil without any soil sampling and treatment. Although soil sampling and subsequent laboratory analysis is still needed for confirmation of results, the number of samples required can be reduced considerably.

The accuracy of in-situ measurements in determining radionuclide activity concentrations in soil relies on two primary elements: the detector calibration and source geometry of the site. The field calibration can be expressed in terms of measured full absorption peak count rate, N (the subscript "o" represents the response at the normal incidence and the subscript " f " represents the integrated response over all angles), the fluence rate, Φ, and the activity concentration in the medium, A [Mil94]. The ratio of these quantities is then expressed as:

$$\frac{N_f}{A} = \frac{N_f}{N_O} \bullet \frac{N_O}{\Phi} \bullet \frac{\Phi}{A} \qquad (1.20)$$

where N_f/A is the total absorption peak count rate (cps) at some energy E, for a particular radionuclide per unit concentration of that radionuclide in soil . N_f/N_O is the angular correction factor for radionuclide distribution in the soil. N_O/Φ is the full energy peak count rate to flux density for parallel beam of photons at energy E that is normal to the detector face. Φ/A is the photon flux density from un-scattered photons arriving at the detector per unit radionuclide activity for a given radionuclide distribution in the soil.

The source geometry is evaluated as a volume source at a fixed height of one metre above the ground. The source geometry is primarily controlled by the depth profile of the radionuclide being measured.

A typical example of a field γ-ray measurement is a conventional portable coaxial HPGe detector with a 12% relative efficiency and a resolution of 1.9 keV (relative to the 1332 keV for ^{60}Co). A tripod supports the detector, with the front part being 1 meter above the ground. The dewar has a capacity of 7.0 liters of liquid nitrogen (LN_2) and holding time of five days. The detector is orientated in a downward facing way. Detector calibrations for field γ-ray spectrometry are performed by calculations and by using point like γ-ray sources [Fül99].

- **Laboratory based gamma ray spectroscopy**

γ-radiation is a penetrating form of radiation, and therefore can be used for non-destructive measurements of samples of any form and geometry as long as standards of the same form are available and are counted in the same geometry to calibrate the detector. Various detector types are used to measure γ-rays. The one used in this study is the HPGe, which has the advantage of high-energy resolution.

Most γ-ray spectrometry systems are calibrated with commercially mixed standards; ideally the matrix and geometric form of standards needs to match that of sample as closely as possible. However this is often difficult because one does not for example know the composition of the sample to be analysed. There is commercially available software for the analysis of the γ-ray spectra. Adjustments to the calibration for the corrections of density and effects such as self-absorption need to be done. This study utilises this method of analysis.

1.5 The motivation for this study

The research interests in the Environmental Radiation Laboratory (ERL) at iThemba LABS (South Africa) are as shown in the diagram below:

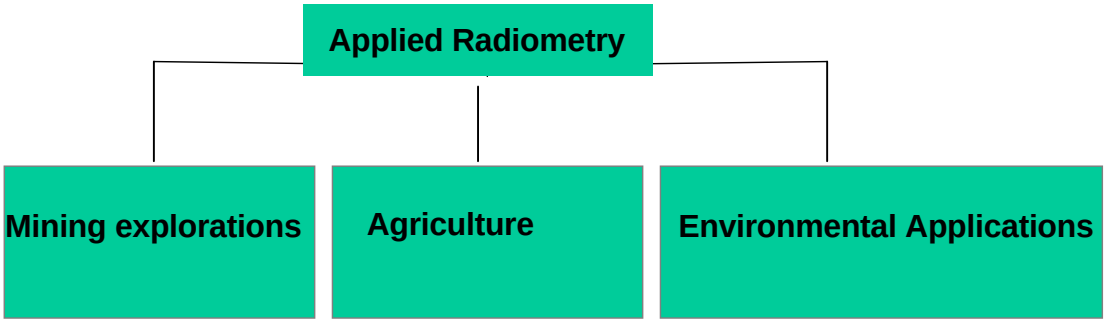

Figure 1.9: Application of Radiometric methods in different fields.

A connection between radiometry and minerals has been established and a method called radiometric fingerprinting was the result [Dem98]. In principle, characterisation of samples is based on the mineral's percent composition of natural radionuclides such as ^{238}U, ^{232}Th and ^{40}K by detection of the gamma rays from such minerals. Samples are collected from the area of surveillance and brought to the laboratory for analysis.

Table 1.3 shows the results of a study on radiometric fingerprint of minerals associated with heavy minerals deposits conducted in South Africa [Dem98].

Mineral	^{40}K	^{214}Bi	^{232}Th
Quartz	116 (8)	2 (2)	< 9
Silt/clay minerals	218 (10)	49.4 (1.1)	127 (3)
Ferricrete	95 (7)	130 (3)	160 (4)
Magnetite	< 10	120 (120)	200 (200)
Ilmenite	2.8 (0.5)	18 (2)	27 (9)
Rutile	13 (3)	460 (70)	< 60
Zircon	< 18	3280 (120)	444 (16)
Monazite	1600 (600)	42000 (2000)	181000 (2000)

Table 1.3: Radiometric fingerprint given as activity concentrations ($Bq.kg^{-1}$) associated with heavy minerals in South Africa [Dem98]. Uncertainties are given in brackets.

The table shows that the values of natural radioactivity concentrations can be used to characterise minerals according to grain size and composition.

The Environmental Radioactivity Laboratory (ERL), has embarked on measurement of natural and anthropogenic radionuclides in soil and liquid samples. For this purpose a high purity germanium detector (HPGe) housed in a lead castle is being used for laboratory-based measurements, while a MEDUSA (Multi Element Detector System for Underwater Sediment Activity) scintillation-based detector is being used for in-situ measurements [Hen01]. This study will discuss a new method called the Full Spectrum Analysis (FSA) method in addition to the conventional Window Analysis (WA) method to measure activity concentrations in soil samples (see the next section) in the laboratory.

1.6. The aim and scope of this study

Traditionally activity concentrations in soil samples are determined using what is called a Windows Analysis (WA) procedure. This involves analysing the spectrum measured (normally in the laboratory) using windows or regions of interest (ROI) set around prominent γ-ray peaks associated with the decay of ^{238}U, ^{232}Th and ^{40}K. The windows are used to determine the net counts (that is after an appropriate background subtraction) in the peak of interest. By using these counts with the branching ratio (associated with a particular γ-decay path), measurement live time, sample mass and full energy peak detection efficiency, it is possible to calculate the activity concentrations.

A new technique for measuring primordial radionuclide activity concentration in soil samples with HPGe is introduced in this study. This technique called Full Spectrum Analysis (FSA), uses the full spectral shape and 'standard' spectra to calculate the activity concentrations of, ^{238}U, ^{232}Th and ^{40}K present in a geological matrix [Hen01].

The FSA technique was first used in conjunction with the MEDUSA detector by the KVI Nuclear Geophysics Division [Hen01]. The MEDUSA detector, which detects γ-radiation by

means of a scintillator (BGO or CsI), is used to perform in-situ measurements of natural activity concentrations on seabeds [Ven00] and on land [Hen01].

FSA involves the fitting of a measured γ-ray spectrum (~200 keV to 3 MeV) by means of a linear combination of the three so-called standard spectra and a background spectrum. Each standard spectrum corresponds to the response of the detector in a particular geometry (normally that of a flat bed) for a sample containing 1 Bq/kg of a particular nuclide (^{238}U, ^{232}Th and ^{40}K). These standard spectra are normally obtained via measurement or by means of Monte Carlo simulations. The measured spectrum S is considered to be a superposition of weighted standard spectra, where the factors $C_{k,}$ $C_{U,}$ and C_{Th} are the activity concentrations of each nuclide in the sample [Dem97]. Mathematically it can be expressed as:

$$S\ (i) = C_K S_K (i) + C_U S_U (i) + C_{Th} S_{Th} (i) + S_B (i) \qquad (1.21)$$

The spectrum deconvolution was applied and the coefficients C_K, C_U, and C_{Th} were determined using the χ^2 minimisation technique.

In this study the results from FSA and WA of HPGe spectra of a variety of sediment samples are critically compared after which the advantages and disadvantages of each method are established

1.7 Thesis outline

The next chapter will talk about the experimental techniques. The HPGe detector system used will be described in detail in chapter 2, while associated experimental work and data analysis are discussed in chapter 3. The results will be presented and discussed in chapter 4. Finally a summary and conclusion will be given in chapter 5.

Chapter 2

Experimental Methods

Various types of detector differ in their operating characteristics, but all are based on the same fundamental principle: the transfer of part or all the radiation energy to the detector mass where it is converted into an electrical pulse. The form in which the converted energy appears depends on the detector and its design [Leo87]. In this study a high purity germanium (HPGe) detector is used. The operation of this detector involves the following: first, the photon energy is completely or partly converted into kinetic energy of electrons (and positrons) by *photoelectric absorption*, *Compton scattering* or *pair production;* second, the production of electron-hole pairs; third, the collection and measurement of charge carriers.

The various components of the HPGe detector used will be discussed in this chapter. The process followed in executing measurements will also be described. The performance characteristics of the detector will also be presented.

2.1 The HPGe gamma-ray detection facility

The facility is used to measure natural and anthropogenic activity concentrations in soil and liquid samples (though in this study the focus is on soil samples). The gamma ray spectroscopy is mainly used for the analysis of natural gamma rays from potassium and the progenies of uranium and thorium. It can also be used to measure artificial radioactivity such as the activities from cesium, strontium etc. The available equipment in the laboratory includes an HPGe detector, lead (Pb) shielding, Marinelli beakers (for sample holding), PC-based data acquisition system, digital weighing balance, and standards.

2.1.1 Physical layout

Figure 2.1 shows experimental set up used in the present study (the picture was taken in the Environmental Radiation Laboratory (ERL)).

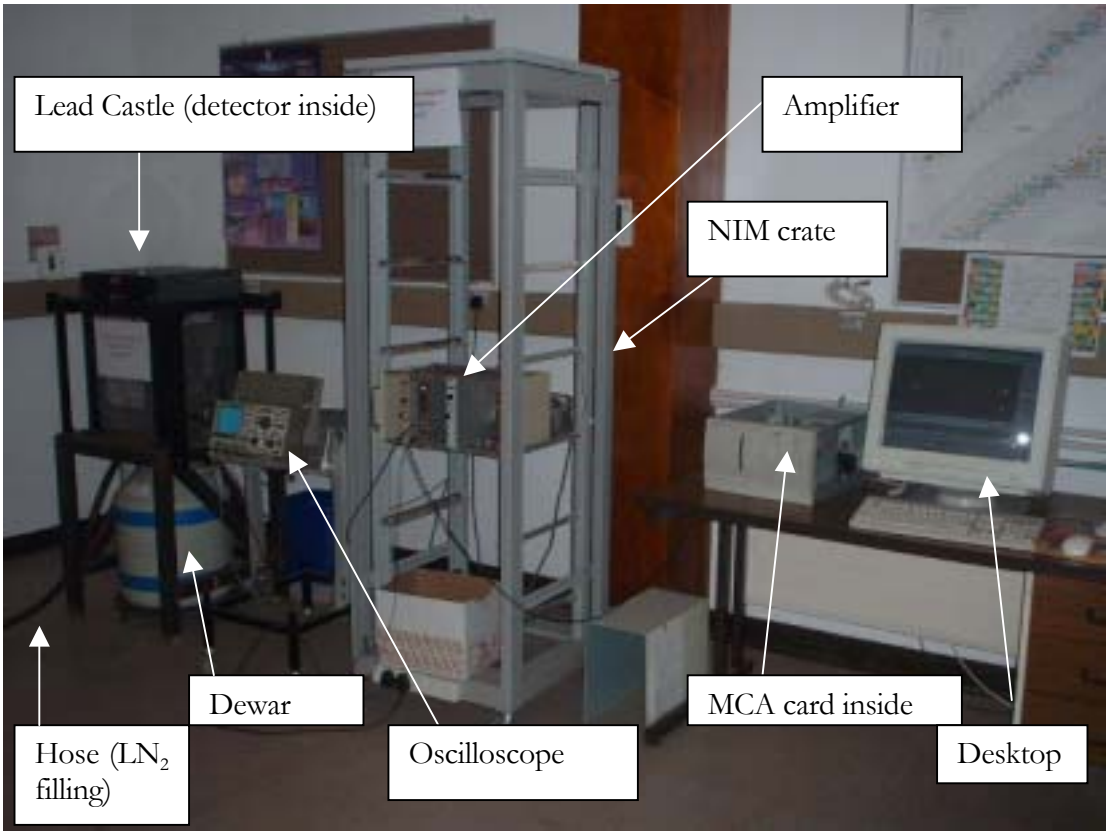

Figure 2.1: The picture showing the setup of the Environmental Radioactivity Laboratory at iThemba LABS.

The lead castle, which opens from the top, shields the detector; and the dewar underneath is for holding liquid nitrogen (LN_2). The oscilloscope is used to set and monitor the pulse properties while the NIM crate carries the amplifier. After amplification the signal is processed in the MCA card in the PC, and then displayed to the desktop.

All radioactive sources are kept in the storeroom far away from the set up (approximately 5 meters) in order to avoid the contribution of such sources to the background during counting.

The laboratory has an air conditioning facility that ensures the maintenance of the normal temperatures around 18 °C.

- **Lead Castle**

Lead is the material employed in the shielding of the detector used in this study. It makes a good shielding material due to its high density and large atomic number. A standard 25% (relative efficiency) detector measurement in a 10 cm thick lead shield will reduce the environmental background by a factor of 1000; thus enabling one to measure $\sqrt{1000} \approx 30$ times weaker sources with the same statistical accuracy [Ver92].

In this study a 10 cm thick lead castle was used. The inside of the castle was lined with a copper layer of 2 mm thickness. The copper layer is there to attenuate the X-rays from the lead (see the Figures 2.2, and 2.3). A typical background spectrum measured with the ERL HPGe is shown in Appendix C.

Figure 2.2: The picture shows the lead castle supported by a metallic frame surrounding the HPGe detector.

The black hose shown in Figure 2.2 is for the filling of the detector dewar with liquid nitrogen.

A B

Figure 2.3: The open top view showing the detector (A) and a Marinelli beaker on top of the detector (B).

2.1.2 HPGe technical specifications

The detector used is a closed end-coaxial Canberra p-type (model GC4520), with a relative efficiency of 45%. The germanium crystal is located inside the lead shield. The vertical dipstick cryostat (model 7500SL), which is cooled by liquid nitrogen, is contained inside a dewar (see Figure 2.7). The detector crystal has a diameter of 62.5 mm and a length of 59.5 mm.

2.1.3 Electronics

The electronic system for this semiconductor detector (HPGe) is shown schematically in Figure 2.4. The system consists of a detector bias supply (SILENA model 7716), preamplifier (model 2002CSL), amplifier (model ORTEC 572), multi channel analyser (OXFord-Win) and a desktop computer.

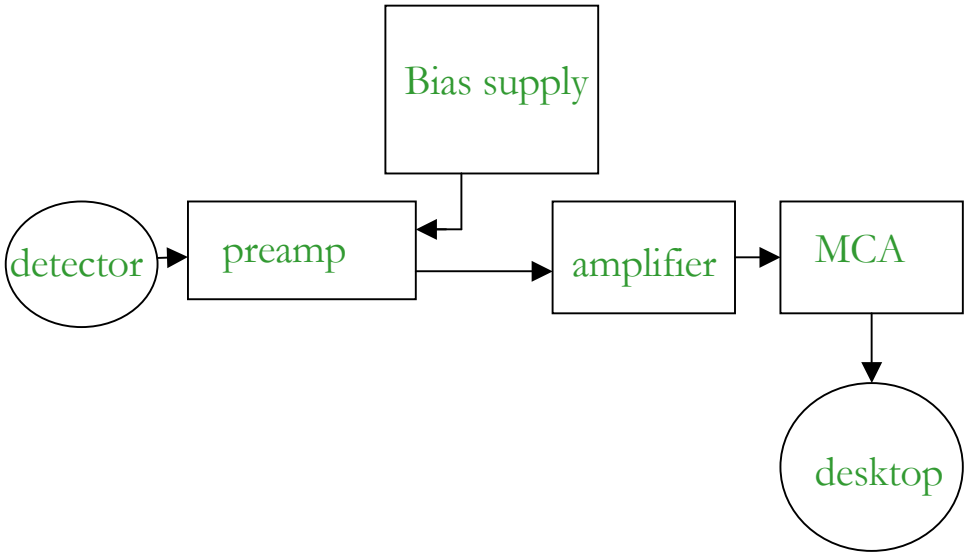

Figure 2.4: Schematic diagram illustrating the electronic setup used to acquire the HPGe data.

- **Detector**

The detector is a cylinder of germanium with an n-type contact on the outer surface, and the p-type contact on the surface of an axial well see Figure 2.5. The n and p contacts are diffused lithium and implanted boron respectively [USR98]. The germanium detector, like other semiconducter detectors, is a large reverse biased p-n junction diode. The germanium has a net impurity level of about 10^{10} atoms/cm^3 so that with the moderate reverse bias the entire volume between the electrodes is depleted and the electric field extends across this region [USR98].

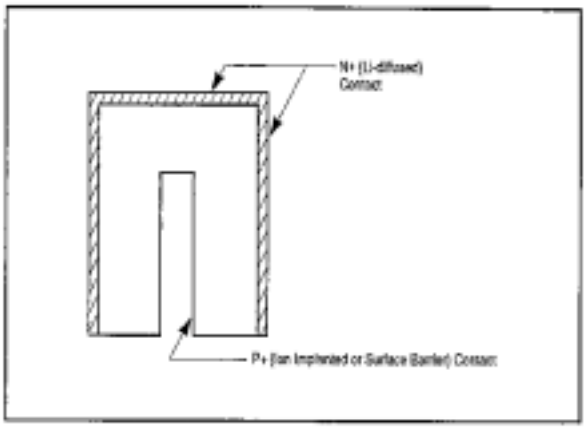

Figure: 2.5 Coaxial Ge Detector Cross Section [USR98].

The radiation energy is transferred to the detector crystal by an interaction process (photo electric interaction), which then creates electron-hole pairs.

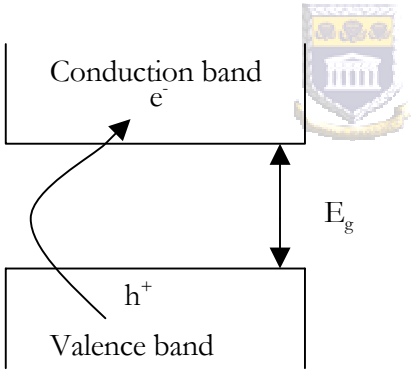

Figure 2.6: A diagram showing a typical semiconducter with band gap E_g.

The mobile electrons in the conduction band were promoted under an influence of an electric field from the valence band, the holes in the valence band are also mobile, but the mobility of the latter is in the opposite direction to the former. This movement of electron hole pairs (e^- /h^+) in a semiconducter constitutes a current. If these arrive at their respective electrodes, the

result is a current proportional to the energy deposited in the crystal or a pulse [Lil01]. This is a small signal requiring amplification.

The energy required to create an electron-hole pair across the Ge band gap (E_g) is approximately 3 eV, thus an incident gamma ray, with an energy of several hundred keV, produces a large number of such pairs, leading to good resolution and low statistical flactuations. These are desireable properties of a detector. HPGe detectors are operated at temperatures of around 77 K, in order to reduce noise from electrons which may be thermally excited across the small band gap at standard temperatures [Lil01]. There are weekly fillings of the ERL HPGe liquid nitrogen dewar (capacity of about 20 liters) to provide for such low temperatures.

The following is a cross sectional diagram of a germanium detector with a dewar:

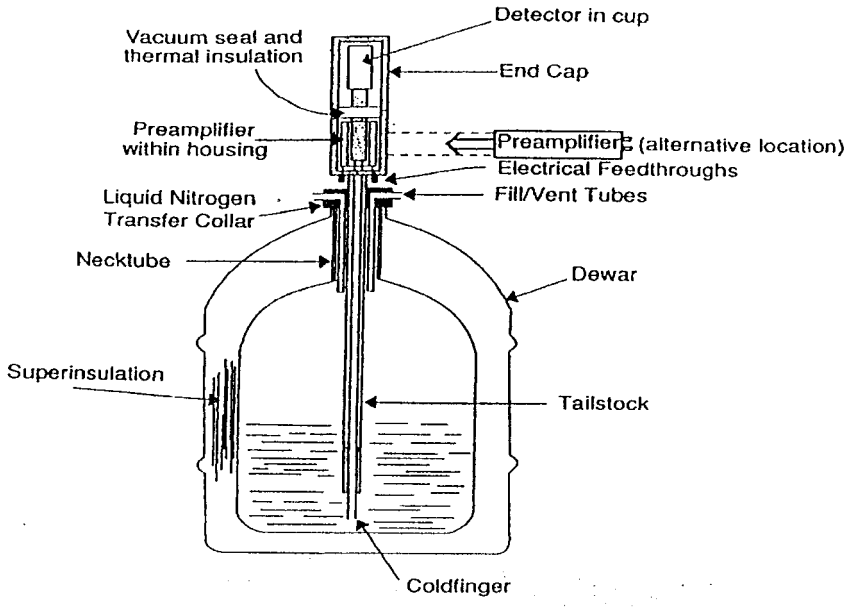

Figure 2.7: A typical germanium detector, cryostat and liquid nitrogen reservoir(dewar)[Gil95].

- **Detector bias**

Radiation detectors require the application of an external high voltage for their proper operation. This voltage is normally referred to as detector bias, and the high voltage supplies used for this task are often called detector-bias supplies [Leo87]. The SILENA model 7716 detector bias supply was used in this study. A bias voltage of approximately 3.5 kV was supplied and as photon interaction takes place within the depleted region; charge carriers are swept by the electric field to their collecting electrodes. The specified depletion voltage for the HPGe used is in fact 3 kV.

- **Preamplifiers**

The main function of the preamplifier is to amplify the weak signal and send it through to the cable that connects the preamps with the rest of the equipment. The preamps are mounted as close as possible to the detector to minimise the length of the cable, since the input signal is very small. The longer the length of the cable the more the capacitance and that reduces the signal-to-noise ratio [Leo87]. Therefore the manufacturing of the built-in preamplifiers minimises this effect. Furthermore, when the detector system is cooled the preamplifier also indirectly gets cooled, thus reducing the chances for thermal excitation of charge, which could bring about leakage current[4]. A charge sensitive preamplifier will convert the charge into a voltage pulse proportional to the energy deposited in the detector crystal. The preamplifier used in this study is of the model 2002CSL.

- **Amplifier**

The amplifier (model ORTEC 572), then further amplifies the pulse from the preamplifier to a bigger size. The pulse needs to be shaped to a more convenient form; therefore the amplifier's

[4] The unwanted current leaking between two electrodes under voltage.

frequency response is set by a shaping time constant τ, which is 6 μs for the amplifier [USR98]. Should a second signal arrive within the given period τ, it will ride on the tail of the first and its amplitude will be increased. The energy information will therefore be distorted, resulting in a phenomenon called pile-up, which is when pulses are too close together to be separated [Leo87]. This is not a problem in this study, since the detector system dead time was always less 1%. Pulse shaping can also be used to optimise the signal to noise ratio.

- **Multi Channel Analyser (MCA)**

The operation of the multi channel analyser is based on the principle of converting an analog signal, which is basically the pulse amplitude into an equivalent digital number usually referred to as a channel. After this is done the digital information will be stored in the memory to be displayed on the monitor. This activity is in principle carried out by the Analog to Digital Converter (ADC) [Kno00]. The pulses are collected, sorted according to pulse height in the ADC and a γ-ray spectrum is generated. Therefore the performance of the MCA is primarily dependent on the ADC. The results discussed in this thesis were measured using an MCA card (OXFord-Win) in a PC using the OXWIN software program. The MCA diagram is shown below:

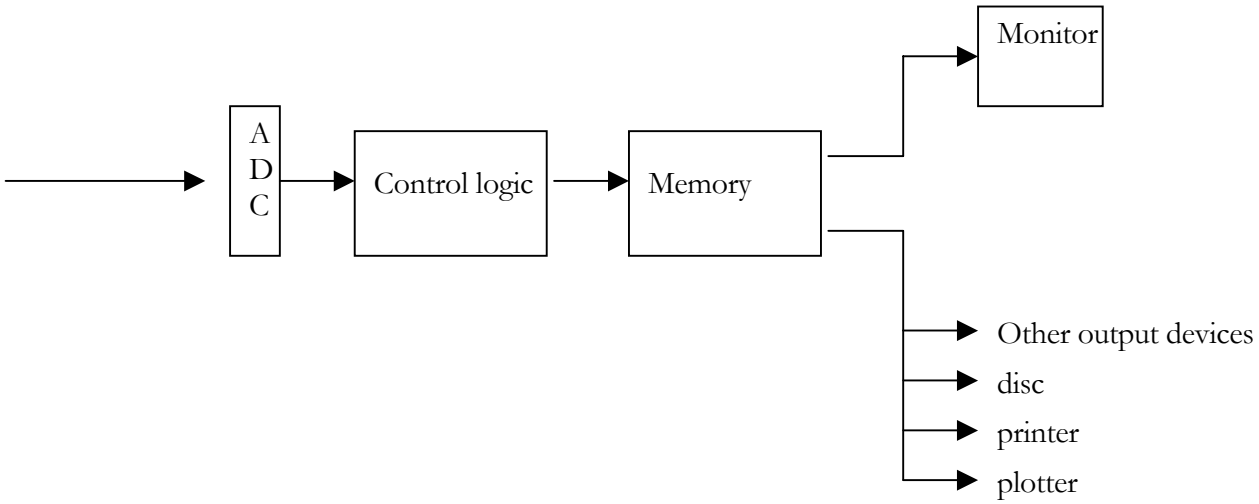

Figure 2.8: Basic architecture of a MCA.

2.1.4 Figure of merit

To keep track of the performance and reliability of the detector it is imperative to keep on checking our results based on the detector specifications. This can be achieved by doing the energy calibration, checking the Full Width at Half Maximum (FWHM)**,** and determining the peak to Compton ratio. The background measurements were done in each case to ensure derivation of proper concentrations. These concepts are discussed in this section.

- **Energy calibration**

Prior to acquisition of the data, energy calibration has to be performed as part of the setting up procedure. Various techniques of determining the energy at a particular channel are implemented, as this is a requirement by most nuclear applications. In some MCAs, a simple two-point energy calibration is used to determine both the offset and slope by the equation

$$E = A(ch) + B \qquad (2.1)$$

where E is the energy and ch is the channel number and A and B are constants; thus the energy as a function of channel number can be directly read out. The MCA systems in use allows the user to choose between first-order (linear) or second order (quadratic) equations that use a least square fit to data points. In this study a second order equation was used, because the detection and amplification are not always exactly linear, and this can be written as follows:

$$E = A(ch)^2 + B(ch) + C \qquad (2.2)$$

Any source whose peaks are known can be used to do the energy calibration. In our study sources such as a mixed liquid source was used (^{152}Eu, ^{60}Co and ^{137}Cs mixture). ^{232}Th and ^{238}U sources were also often used. The following is a particular case in which a mixture of ^{40}K, ^{232}Th and ^{238}U was used as a source. The energies of prominent γ-ray lines are presented in Table 2.1 below.

Decay series	Decaying nucleus	Energy (keV)	FWHM (keV)
^{238}U	^{226}Ra/^{235}U	186.1	1.51
^{232}Th	^{212}Pb	238.6	1.54
^{238}U	^{214}Pb	295.1	1.57
^{232}Th	^{228}Ac	338.4	1.60
^{238}U	^{214}Pb	352.0	1.60
^{232}Th	^{208}Tl	583.0	1.73
^{238}U	^{214}Bi	609.3	1.74
^{232}Th	^{212}Pb	727.3	1.81
^{232}Th	^{228}Ac	911.2	1.91
^{238}U	^{214}Bi	1120.3	2.03
^{40}K	^{40}K	1460.8	2.21
^{238}U	^{214}Bi	1764.5	2.38
^{238}U	^{214}Bi	2204.1	2.62
^{232}Th	^{208}Tl	2614.4	2.85

Table 2.1: γ-ray energies with associated Full Width at Half Maxima (FWHM) for γ-ray lines associated with decay of ^{40}K and the series of ^{238}U, ^{232}Th; the energies are taken from [EML97]

The objective here is to derive a relationship between peak position in the spectrum and the corresponding gamma-ray energy. The mixture of three sources with well-known energies was made to ensure that the calibration covers the entire energy range over which the spectrometer is to be used. The data on energies were taken from [EML97].

Figure 2.9 shows the spectrum for the mixture of materials used.

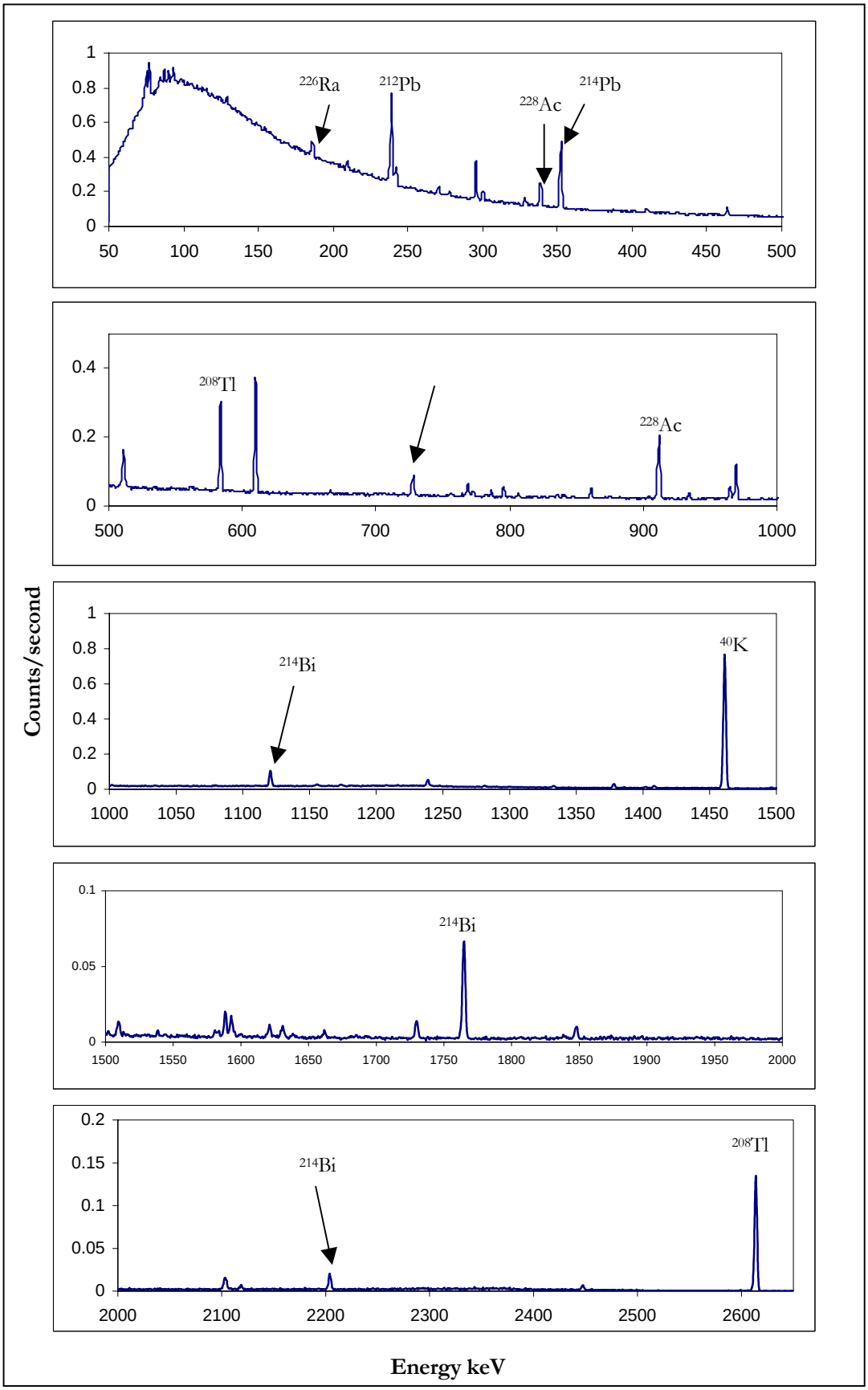

Figure 2.9: The energy calibration spectrum showing the lines (labelled) used to perform energy calibrations; a mixture of ^{40}K, ^{232}Th and ^{238}U was used as a source.

The spectrum has to be measured for long enough in order to determine the peak properties with sufficient accuracy for the peaks to be used for the calibration. The calibration process involves marking the peaks to be used and their true energy; see section 3.1 for the region of interest (ROI) discussion. The set ROI is used by the Oxwin software to calculate, amongst others, the peak centroid.

The relationship between energy and channel number is shown in Figure 2.10.

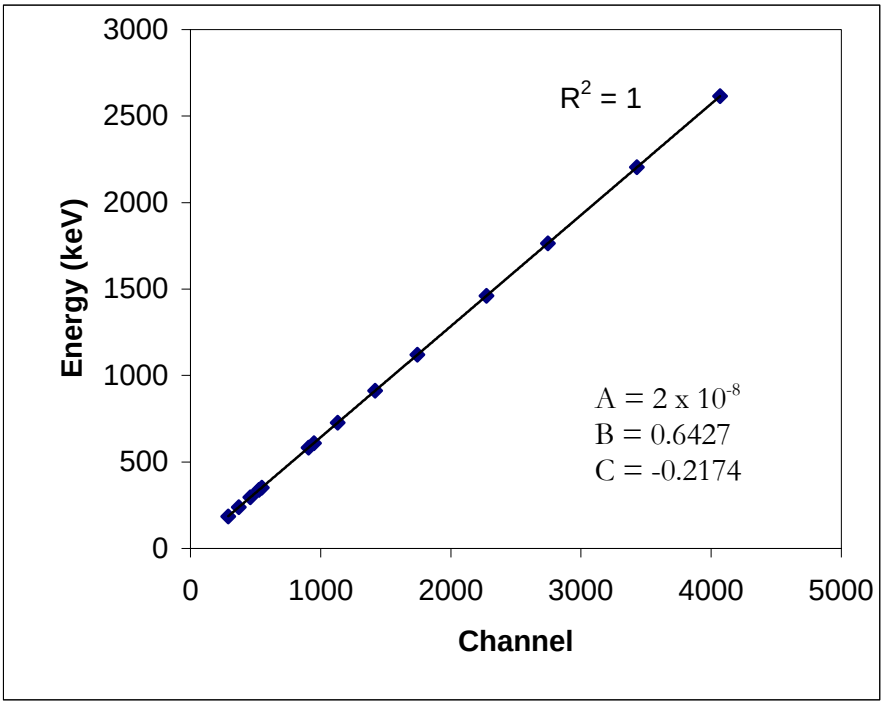

Figure 2.10: A typical fit to data points used to energy calibrate the HPGe detector system. The energies used are also given in Table 2.1.

- **Energy resolution**

The energy resolution of the HPGe detector system as a function of γ-ray energy was calculated after the energy calibration. The energy resolution of the detector (at a particular γ-ray energy) is conventionally defined as the full width-to-half maximum (FWHM) of the peak divided by the peak energy. Therefore the energy resolution, which is a dimensionless fraction, is conventionally expressed in percentages. Small percentage resolution of a peak implies good resolution [Kno79].

In principle one should be able to resolve peaks at two energies, which are separated by more than one value of the detector FWHM at that energy.

In order to parameterize the dependence of FWHM on γ-ray energy, the FWHM data for the lines given in Table 2.1 were fitted using a linear function. The fit to the data are shown in Figure 2.11. The results for the FWHM calibration shown in the Table 2.1, were obtained from the following equation:

$$FWHM = AE + B \tag{2.3}$$

where A and B are constants deduced by the OXWIN software program and E is the γ-ray energy. The graph in Figure 2.11 was then plotted from these results.

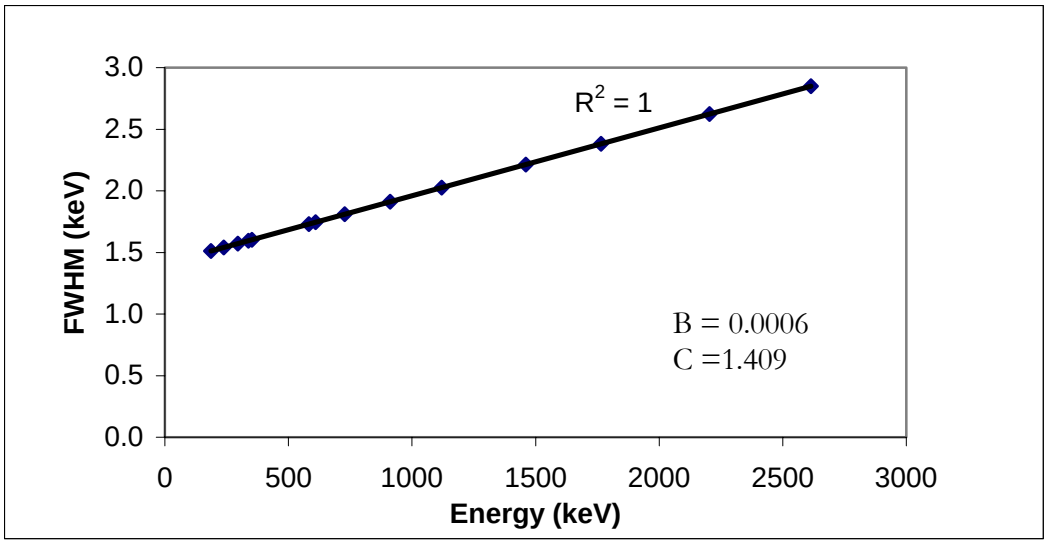

Figure 2.11: A Full Width at Half Maximum calibration graph with a line of best fit.

According to the specifications of the detector, the resolution should be 2 keV for the 1332 keV line for ^{60}Co. On interpolation, the value of 2.2 keV was found for this value in this work, implying a deviation by 9% from the specified value.

- **Peak to Compton Ratio**

The Peak-to-Compton ratio is an important quantity defined as the ratio of the counts in the channel corresponding to the highest number of counts per channel in the photo-peak (photo-peak centroid) to the counts in the 'typical channel' of the Compton continuum. This 'typical channel' is defined as the region of interest between 1040-1094 keV for a ^{60}Co source [Kno00]. The Compton continuum results from the Compton scattering in which the gamma rays entering the detector will not deposit their full energy on interaction with matter. This partial energy event appears in the spectrum as an event below the full energy peak in the Compton continuum. The Peak-to-Compton ratio ranges from 30 to 60 for coaxial germanium detectors when using the 1332 keV line associated with the ^{60}Co decay [Kno00].

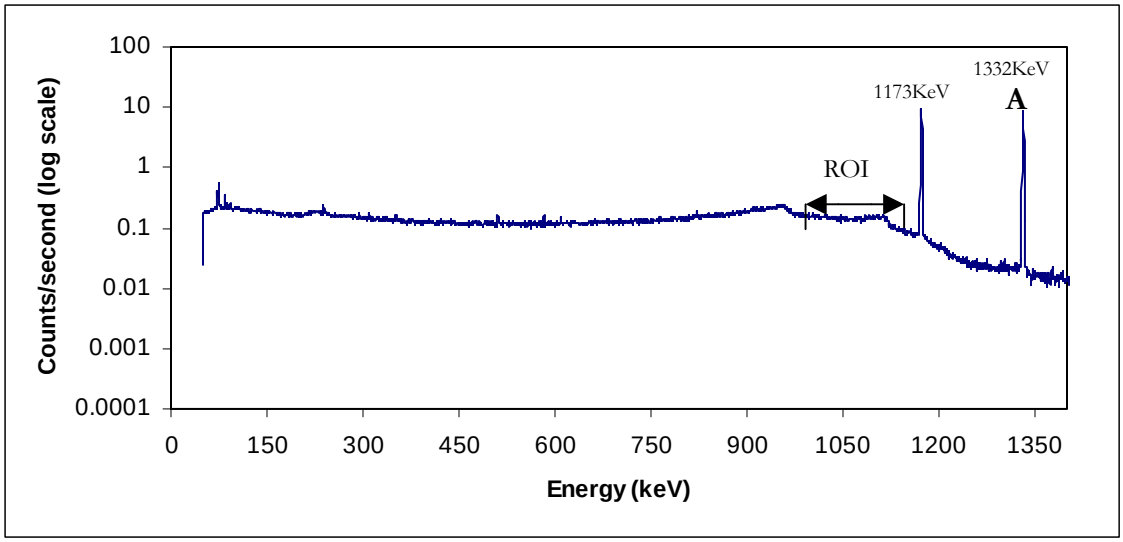

Figure 2.12: A spectrum of ^{60}Co for peak to Compton ratio determination.

A region of interest ROI (1040–1096) keV was established along the Compton continuum, and then the ratio of the number of counts in the photo peak to the continuum was determined. The Table 2.2 shows the data required for such a measurement.

A	ROI	C	G
30394	511	87	44482

Table 2.2 A table of counts in the chosen region of interest with number of channels along the ^{60}Co Compton continuum and in the channel corresponding to the highest number of counts in the full energy peak. A = Number of counts in the channel corresponding to the highest number of counts per channel in the full energy peak, ROI = Counts per channel in the region of interest, C = Number of channels in the region of interest. G = Gross counts in the region of interest.

Counts per channel in the region of interest ROI = G / C = 511 = Gross counts divided by the number of channels within the region. Therefore peak to Compton ratio = A/ROI = 59 :1

This value is very close to the one specified by the manufacturer, which is 58:1 [USR98]. The higher the value the more efficient the detector is, and thus the value should preferably be high.

2.2 Sample Selection, Preparation and Measurement

The types of samples studied were mainly soil taken from mine dumps, in particular from Kloof mine in Westonaria south west of Johannesburg (RSA) and beach sand from the west coast of South Africa. The samples were packed in plastic bags from the areas of surveillance and brought to the laboratory at iThemba LABS. At the laboratory the soil samples were put in an oven (Labotech) and set to 105ºC to allow for drying overnight. After drying the samples were crushed and sieved with a mesh having a hole diameter of 2 mm in order to remove organic materials, stones and lumps. The information about treatment of samples can be obtained from the general guide [ISO03]. The samples were weighed on a digital weighing balance (Sartørius, model BP2100S) with a precision of ± 0.01g; and after sealing with silicon sealant in Marinelli beakers, the samples were allowed to stand for several days (about 21 days) for secular equilibrium to be reached. The following is a table of sample information.

Sample ID	Mass(kg)	Livetime (s)	Volume (ml) (Estimated)	Density (g/cm^3)	Sealed Yes/No
Kloof sample #6B	1.21477	35924	1000	1.21	Yes
Westonaria Sand # 17A	1.26737	74357	800	1.58	Yes
West Coast sand # (3)	1.42652	28796	900	1.59	Yes
Brick Clay #(6)	1.15201	28776	860	1.34	Yes
Thorium+stearic acid #5	0.67734	28740	1000	0.677	Yes

Table 2.3: The table of the samples collected at different sites.

- **Marinelli beaker**

Environmental samples of low-level radioactivity are often measured in Marinelli beakers specially designed to provide good detection sensitivity. Full Energy Peak Efficiency (FEP) variations are observed in this geometry for different sample types [Sim92]; this is due to self-attenuation effects, a concept that is discussed later with results (see also Appendix D). See Figure 2.13 and D.1 for Marinelli beaker photo and a drawing of its dimensions respectively.

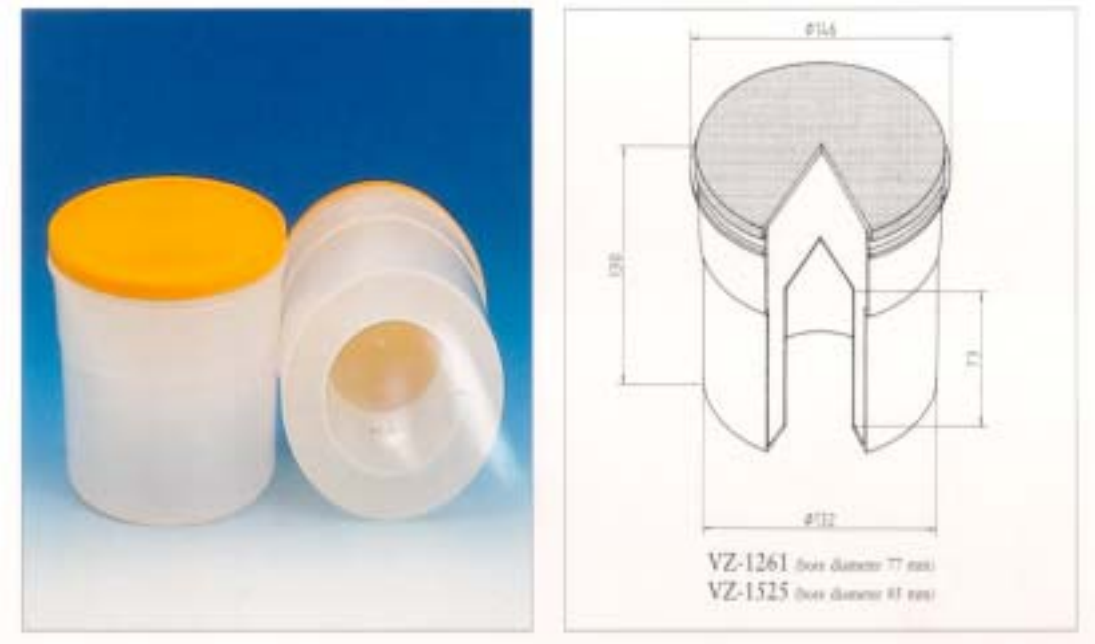

Figure 2.13 Photo of Marinelli beaker and the design of its geometry. The bottom part shows its re-entrant hole [Ame00].

In the Environmental Radiation Laboratory (ERL) at iThemba LABS the 1-liter Marinelli beaker (Model VZ-1525) made of polypropylene material, manufactured by Amersham [Ame00] was used. The precision with which the activity can be determined with this Marinelli geometry is limited by the effect of self-absorption for which correction must be made [Dry89]. Self-absorptions effects were verified through the use of the Sima model [Sim92].

This was done on the basis of the difference in the samples' density and volume in this study. The results for this will follow in chapter 4.

In window analysis, if the standard source has the same physical dimensions, density, chemical composition, and radionuclides present as in the sample, the radioactivity of the sample is simply determined by comparison of the count rates in the corresponding full energy peak of the measured pulse height gamma ray spectrum [Par95].

2.3 Reference sources

The two reference sources IAEA-RGU-1 and IAEA-RGTh-1, prepared by the Canada Center for Minerals and Energy Technology on behalf of the International Atomic Energy Agency, were used in this work [RL148]. The ERL Laboratory at iThemba LABS bought the ^{40}K (KCl powder) reference.

- **WA**

The reference source used in this case was KCl of 99% purity; this was used specifically for the efficiency calibration. The advantage of this standard source is the fact that it is easier to handle and is not that hazardous. The method of calibrating detector efficiency using this standard is described in the next chapter. The activity of this is given in the Table 2.4 below. This standard was also used in the FSA method of analysis.

- **FSA**

The information of the reference sources used in the FSA method of analysis is tabulated in Table 2.4. The full details regarding the preparation of these are given by [RL148] except for the ^{40}K reference source, in which KCl was used instead of K_2SO_4 as used by the IAEA (reference manual [RL148]) for example.

Nuclide	Used in which method?	Source Supplied in what form?	Mass (kg)	Volume (ml)	Density (g/cm^3)	Activity Concentration (Bq/kg)
^{238}U	FSA	IAEA (RGU)	0.4873	400	1.2	4940
^{232}Th	FSA	IAEA (RGTh)	0.5157	400	1.3	3250
^{40}K	FSA/WA	KCl (99%purity)	1.2721	1000	1.3	16258

Table 2.4: The table shows the data of reference materials used.

The energy calibration was done independently for each source and the sample to be measured. It is seen in Table 2.4 that the volumes of the reference sources for uranium and thorium differ significantly from those for the sample. The effects of this on the results presented below are discussed in chapter 4.

2.4 Data acquisition

Each time a measurement is done energy calibration has to be done as part of the setting up procedure, before any data acquisition. The counting time was preset on the Oxford-Oxwin software used.

Information regarding the spectra acquired with reference sources, samples and background (Marinelli filled with tap water) are given in Tables 2.5 and 2.6

Source type	Measurement date	Elapsed Real time (s)	Elapsed Live time (s)
KCl	15/08/02	16516	16436
RGU	4/06/02	16200	15996
RGTh	6/05/02	16200	16026

Table 2.5: Spectral information on reference sources (see Table 2.4 for information on Sources).

Sample Code	Long Measurement		Short Measurement	
	Elapsed real time(s)	Elapsed live time(s)	Elapsed real time(s)	Elapsed live time(s)
Kloof #6B	36000	35925	3600	3594
Westonaria #17A	74500	74357	4053	4046
West Coast Sand #D3	28800	28796	3600	3599
Brick clay #D6	28800	28776	3600	3594
Thorium+ stearic acid #5	28800	28740		
Marinelli filled with tap water (Background)	116322	116312		

Table 2.6: Spectral information on Samples and background (see Table 2.3 for more information on the samples)

Chapter 3

Data Analysis

In this chapter the two methods used in this work for determining the activity concentration of ^{238}U, ^{232}Th, and ^{40}K in sediments, namely the Window Analysis (WA) and Full Spectrum Analysis methods (FSA) are described.

3.1 Window Analysis

In the Window Analysis method, the activity concentrations A (Bq/kg) in sediments are calculated using the equation

$$A(Bq/kg) = \frac{C_{Ni}'}{r_{Bi}.M.L_t.\varepsilon_E}, \quad (3.1)$$

where C_{Ni}' is the net counts in the *ith* γ-ray peak associated with the nucleus of interest (^{238}U, ^{232}Th, or ^{40}K). L_t is the live time associated with the sample spectrum; M is the mass of the sample, ε_E the full energy peak detection efficiency at a particular energy E and r_{Bi} the branching ratio of the energy line used (see Table 3.1 for branching ratios used in this study).

C_{Ni}' is obtained from an analysis of the peak of interest using a region of interest (ROI) or window set around the peak, hence the term Window Analysis. An example of a window set is shown in Figure 3.1 where the 1461 keV line (^{40}K) is focused on. In this case the window starts at an energy K (~1455 keV) and ends at an energy Q (~1466.5 keV). The region below line P is due to the Compton continuum.

In this study C_{Ni} was determined using the Oxwin MCA software. The software calculates the gross counts C_g in the window of interest (starting at channel s and ending at channel e) according to the equation 3.2.

$$C_g = \sum_{i=s}^{i=e} C_i \tag{3.2}$$

where C_i is the counts in channel i. The counts in the continuum are calculated using the equation:

$$C_c = \sum_{i=s}^{i=e} C_{Ci} \tag{3.3}$$

where C_{Ci} is the continuum counts in channel i.

The software can therefore calculate the net counts C_{Ni} in a particular photopeak, from

$$C_{Ni} = C_g - C_c \tag{3.4}$$

Even when a sample is not being counted by the HPGe, counts are registered in the spectrum due to room background (see Figure 3.2 for a sample and background spectra). The contribution to C_{Ni} from room background has to, therefore, be subtracted. A room background spectrum was measured by using a Marinelli beaker filled with a 1 liter of tap water. This spectrum is shown in Appendix C. The windows used in the analysis of the sample spectra were used to determine C_{bi} the net background counts in the peaks of interest.

The background subtracted net counts, C_{Ni}' in the *ith* peak was calculated using the expression

$$C_{Ni}' = C_{Ni} - \left(\frac{L_C}{L_B}\right) C_{bi} \tag{3.5}$$

where L_C and L_B are the detector live times during the measurement of sample and room background respectively.

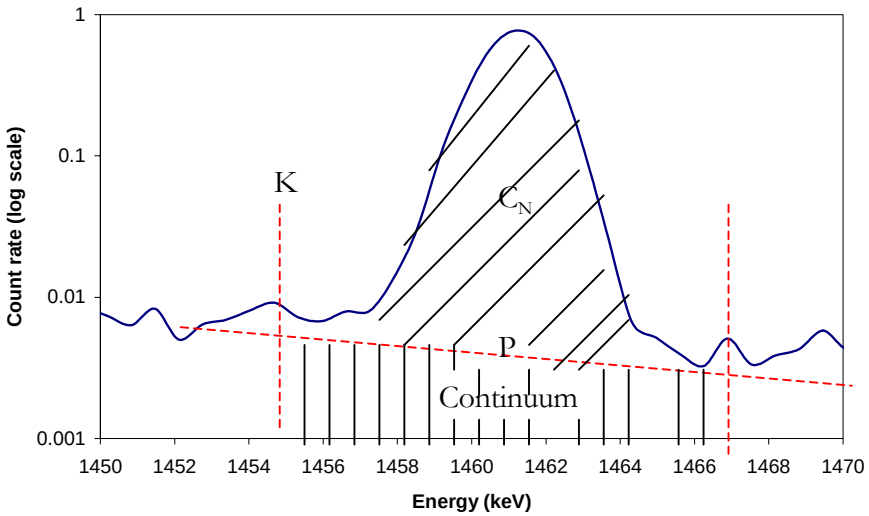

Figure 3.1: A graphical representation of the region of interest with window setting around the ^{40}K peak.

As can be seen from equation 3.1 the full-energy peak (also termed photo peak) detection efficiency as a function of γ-ray energy is needed in order to calculate activity concentrations and is discussed in the next section.

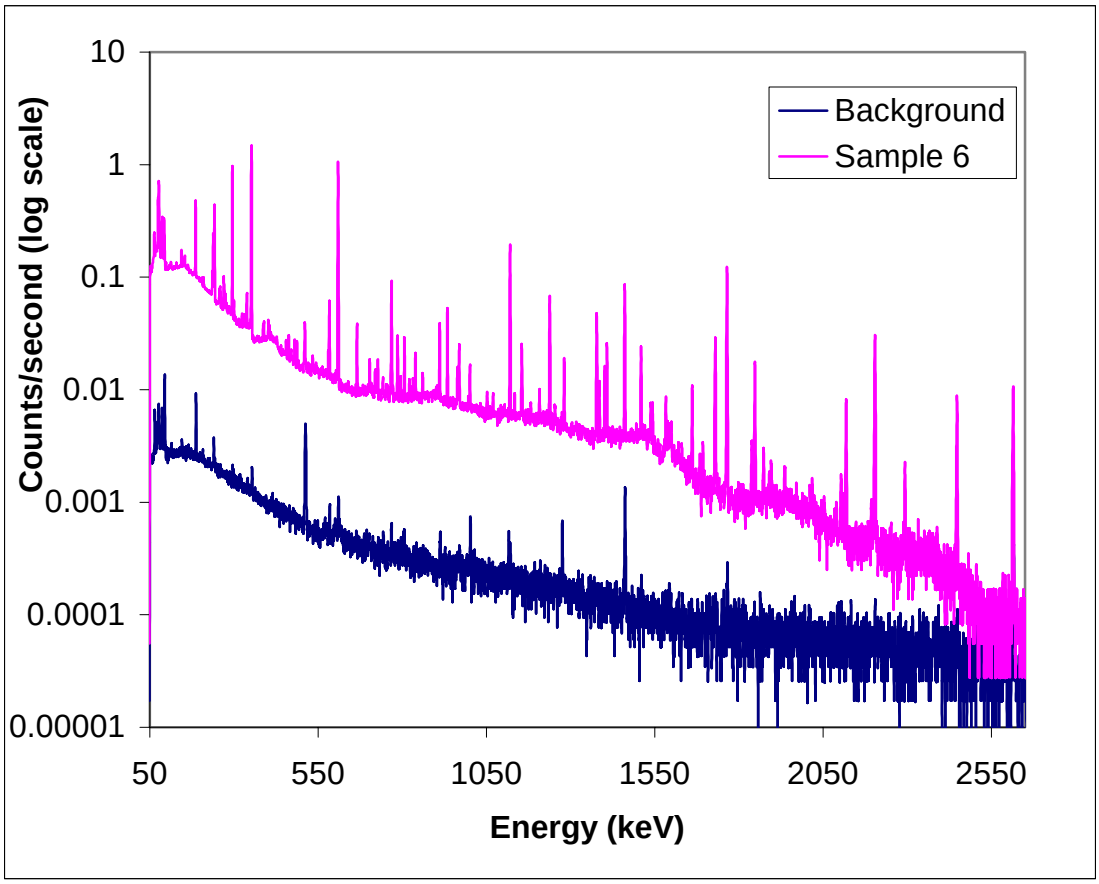

Figure 3.2: A typical representation of sample (number 6b Kloof sample) spectrum with superimposed background spectrum, (measured using a Marinelli filled with 1litre of water) on a log scale.

3.1.1 Determination of γ-ray detection efficiency

The method for determining the efficiency curve used in this work involves two steps. The first step involves the measurement of the relative detection efficiency using ^{238}U and ^{232}Th lines as observed in the sample spectrum measured after secular equilibrium is achieved. The second step entails placing the curve on an absolute scale by using the 1461 keV (^{40}K) line. This is done by calculating the absolute efficiency at 1461 keV for a Marinelli beaker filled to 1 litre with KCl. This is similar to the technique described in reference [Fel92].

One advantage of this approach is that the self-absorption effects are automatically taken into consideration [Fel92]. The other advantage is the fact that the KCl source is more convenient in the sense that it is easier to handle from a safety point of view.

It is assumed that the two decay chains are in secular equilibrium.
The relative efficiency data were fit with a function of the form

$$\varepsilon = a\left(\frac{E}{E_0}\right)^b \tag{3.6}$$

where ε is the efficiency, E is the γ-ray energy in keV, (E_0 = 1) with a and b being fit parameters [Dry89].

On taking the logarithm of equation (3.6) one obtains:

$$\ln \varepsilon = \ln a + b \ln \frac{E}{E_0} \tag{3.7}$$

A flow-chart illustrating the steps used in more detail is given in Figure 3.3.

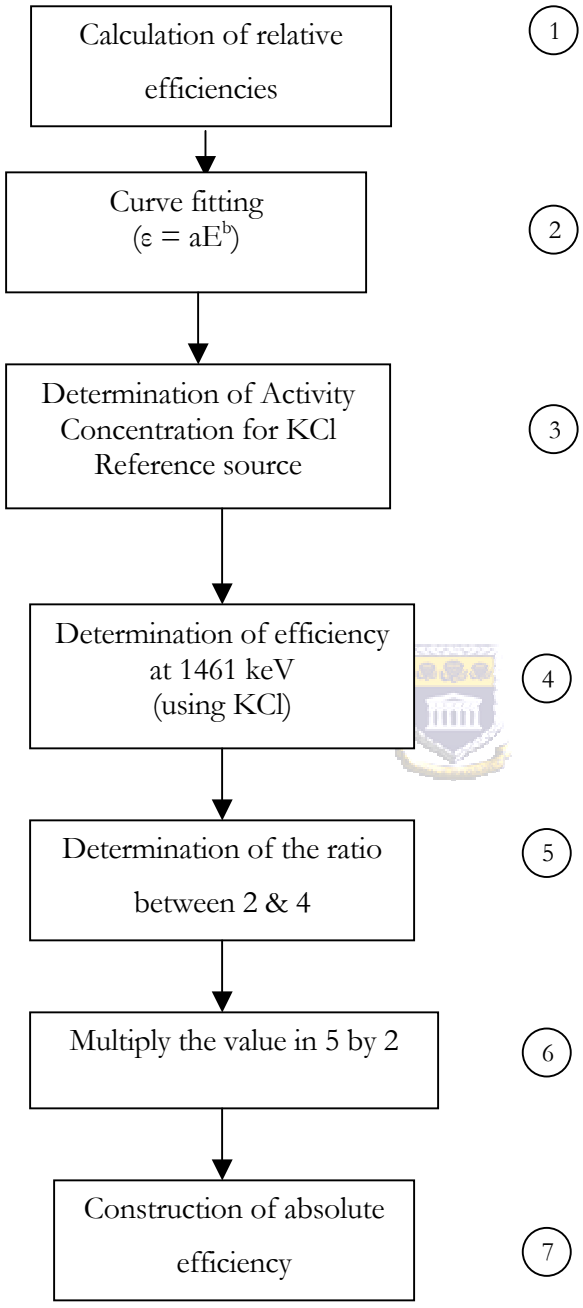

Figure 3.3: A flow chart showing the steps followed in constructing the absolute efficiency curve.

The ^{238}U and ^{232}Th γ-ray lines used to construct the relative efficiency curves along with other properties are given in Table 3.1. Generally the lines used have large branching ratios. However some lines such as the 609 keV and 583 keV lines associated with the decay of ^{214}Bi and ^{208}Tl respectively were omitted since they are prone to coincidence summing [Gar01]. Furthermore lines overlapping with others were not used with the only exception being the 186 keV line (doublet due to lines $^{238}U/^{235}U$) and the 967 keV line due to ^{228}Ac. The γ-ray lines from the radionuclide lines used in the efficiency calibration are shown on the Table 3.1 (and Figure 3.3):

Nuclide	Energy (keV)	Branching ratios
^{238}U Series		
^{226}Ra	186.1	0.05789
^{214}Pb	295.1	0.185
^{214}Pb	352.0	0.358
^{214}Bi	768.4	0.05
^{214}Bi	934.0	0.032
^{214}Bi	1120.3	0.15
^{214}Bi	1238.1	0.059
^{214}Bi	1377.7	0.04
^{214}Bi	1764.5	0.159
^{214}Bi	2204.1	0.05
^{232}Th Series		
^{228}Ac	338.4	0.124
^{212}Bi	727.3	0.067
^{228}Ac	794.8	0.046
^{208}Tl	860.3	0.043
^{228}Ac	911.2	0.29
^{228}Ac	966.8	0.232
^{40}K Series		
^{40}K	1460.8	0.1066

Table 3.1: The gamma ray lines used and their associated branching ratios; the branching ratios are taken from [EML97], branching ratio for ^{226}Ra was corrected for the fact that it is doublet with a 185 keV peak due to ^{235}U.

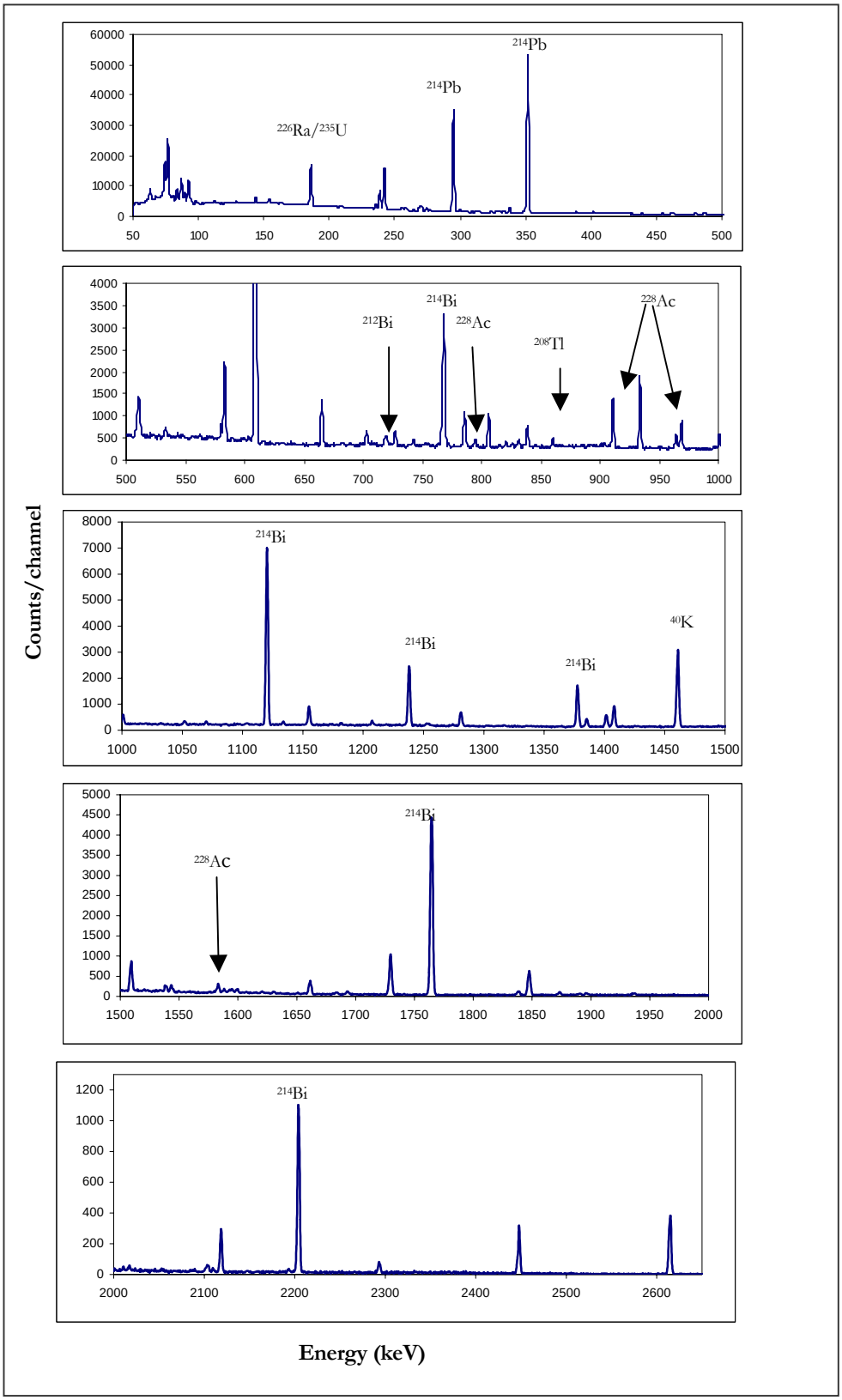

Figure 3.4: The spectrum of Kloof sand sample showing the lines used (see Table 3.1) during detection efficiency calibration.

From the uranium series, fit parameters (a and b) were determined using equation 3.7. These parameters are used to determine the factor that is needed to join the thorium content to the uranium content line using the equation 3.6. Calculations of the relative efficiencies for all the lines including the 1461 keV were done and at this point the relative efficiency curve is determined. The fit parameters generated for a particular sample (Kloof sample) are presented in the graph below:

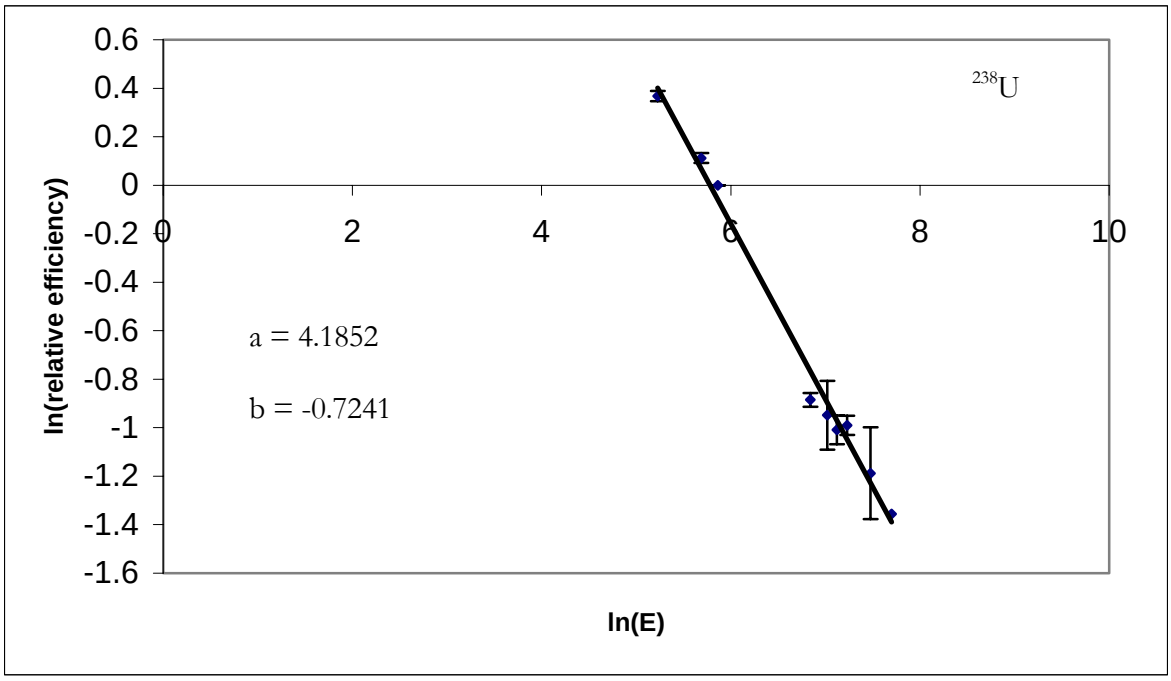

Figure 3.5: Fit *of relative efficiency (with parameters a & b), as determined from lines associated with the decay of ^{238}U (for a Kloof sample number 6). Values were normalised relative to the 352 keV line.*

The Figures 3.6 and 3.7 depict the relative efficiency curve from thorium points and the curve from a combination of both ^{238}U and ^{232}Th points, respectively. From the relative efficiency curve in Figure 3.7, a normalization factor (step five from the flow chart in Figure 3.3) is needed to multiply all the values corresponding to the points in Figure 3.8 to obtain the absolute efficiency curve. The absolute efficiency curve for this sample is shown in Figure 3.9.

The KCl sample was used as a standard source and the absolute efficiency calibration was determined using this sample. The activity of ^{40}K was calculated as follows:

From equation (1.15) $\quad A = \lambda N$

where A is the activity, with λ as the decay constant and N the number of ^{40}K nuclei in KCl. In order to obtain N, one needs to find the number of moles in the KCl, and therefore multiply that with the Avagadro's number N_A = 6.022 x 10^{23}. This brings us to the number of moles n as in the equation (3.8):

$$n = \frac{m}{M} \tag{3.8}$$

with m as the mass of the KCl (1000 g) source and M the molar mass (74.551 g/mol).

Since $\quad N = n \times N_A \times a$ (3.9)

with *a* being the abundance, and that

$$\lambda = \frac{\ln 2}{t_{1/2}} \quad \text{from equation (1.14)}$$

where $t_{1/2}$, the half life for ^{40}K is 1.277 x 10^9y.

Multiplying N by the activity constant λ, and the abundance *a* of ^{40}K in KCl which is equals to 1.17 x 10^{-4}, gives the activity 16256 Bq/kg .

The KCl spectrum measured is shown in Figure 3.15 (section 3.2.1).

The absolute full-energy peak detection efficiency was then calculated using the expression in equation 3.10.

$$\varepsilon_{1461} = \frac{C_{1461}}{r_B . M . L_t . A} \qquad (3.10)$$

where C_{1461} is the nett counts in the 1461 keV line (after background subtraction) and the other symbols are as determined from equation 3.1. ε was found to be 0.00940 ± 0.00007. The uncertainty quoted is that associated with counting statistics.

This efficiency divided by the relative efficiency at 1461 keV yields a coefficient needed to convert all the relative efficiencies to absolute efficiencies. The absolute efficiency curve in Figure 3.9 was generated using this procedure for the Kloof sample. In the same manner absolute efficiency curves were generated for the other samples. The parameterisation of absolute efficiencies $(\varepsilon = a E^b)$ is given in each relative efficiency plot.

The graphs of ln(Energy) versus ln(Relative efficiency) for other samples follow from Figures 3.10 to 3.13.

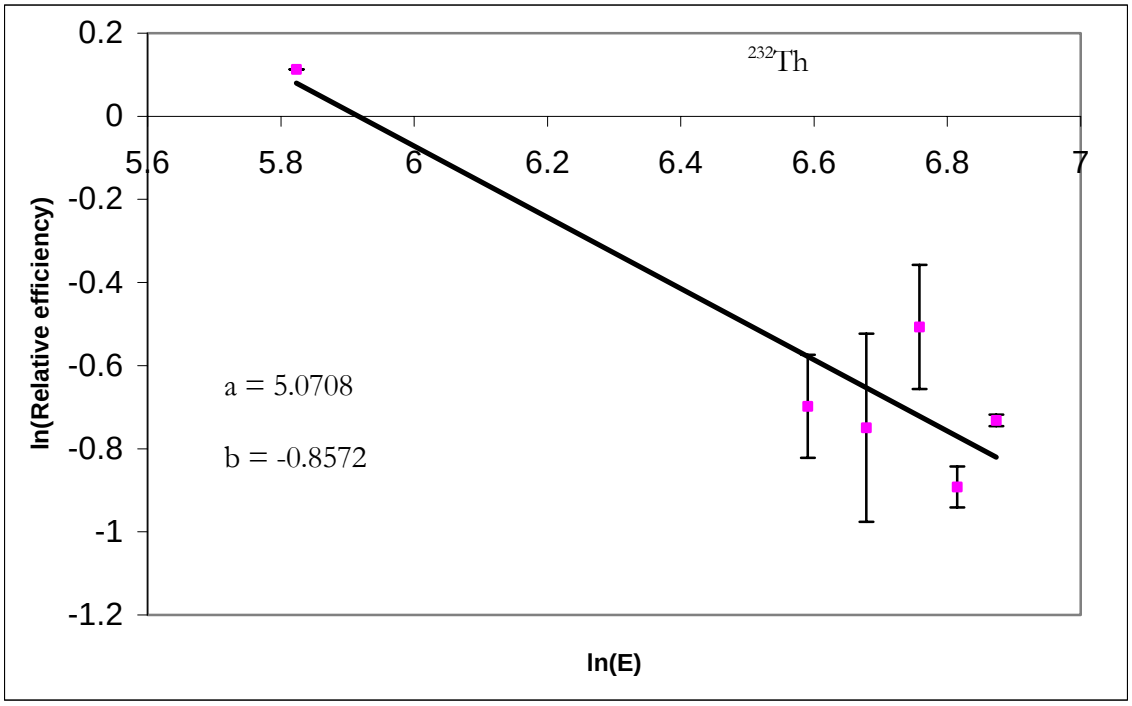

Figure 3.6: Fit *of relative efficiency, with parameters a & b generated (for a Kloof sample), as determined from lines associated with the decay of ^{232}Th. Values were normalized relative to the 338 keV line.*

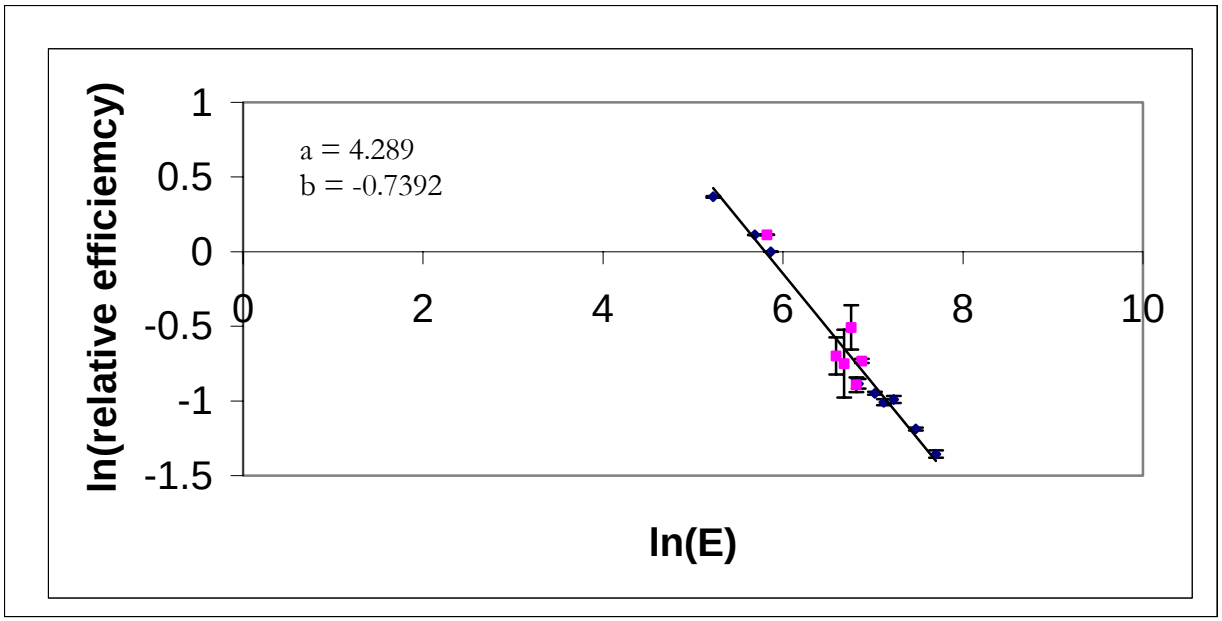

Figure 3.7: A fit of relative efficiency data with parameters a & b generated, as determined from lines associated with ^{238}U and ^{232}Th decay (Kloof sample number #6).

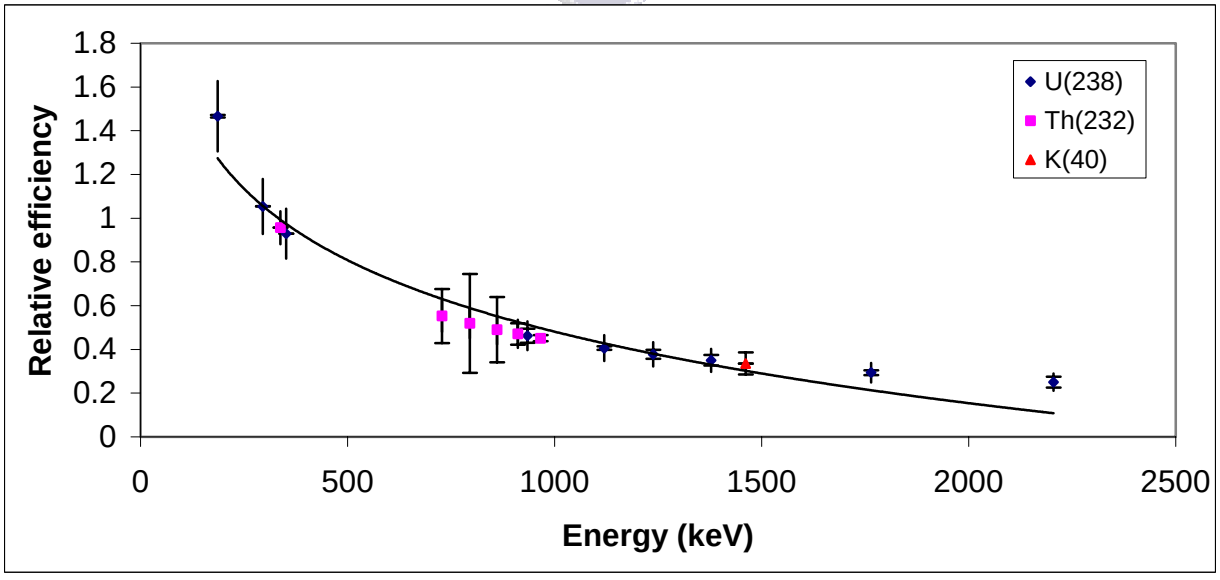

Figure 3.8: A relative efficiency curve for the sample number # 6 (Kloof sample).

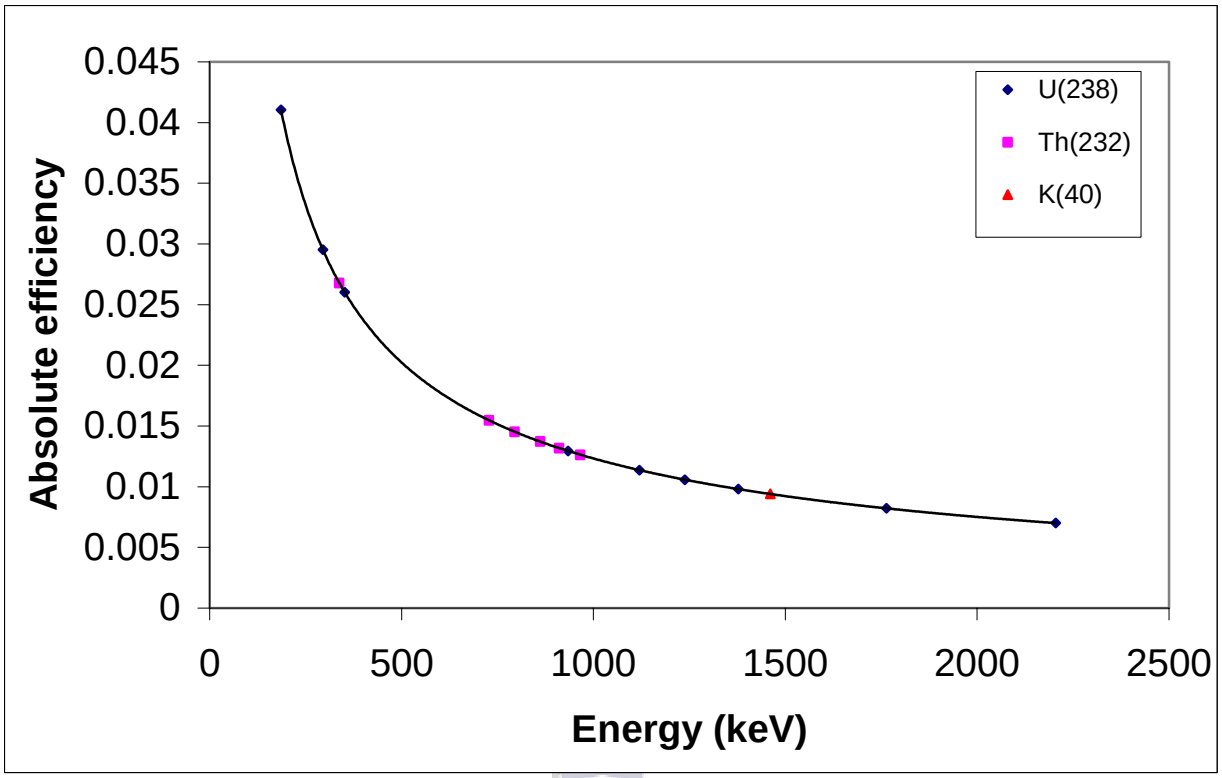

Figure 3.9: A typical absolute efficiencies versus energy graph for various selected lines associated with nuclides ^{238}U, ^{40}K and ^{232}Th, for sample number 6b (Kloof sample)

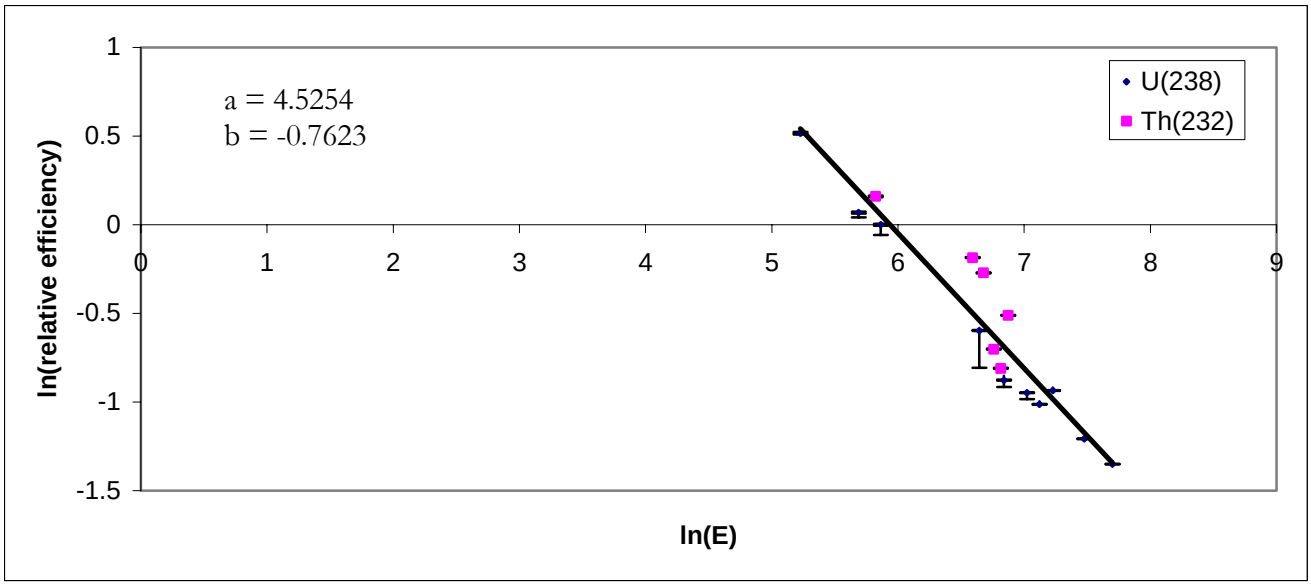

Figure 3.10: *A fit of relative efficiency data with parameters a & b generated, as determined from lines associated with ^{238}U and ^{232}Th decay (Westonaria sand sample number 17A).*

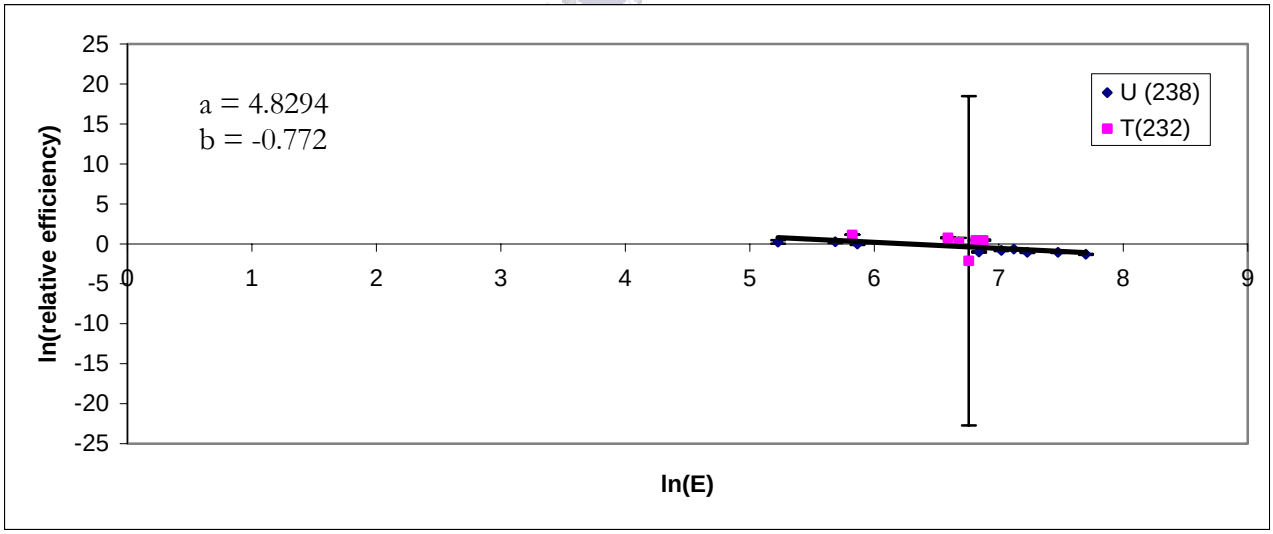

Figure 3.11: A fit of relative efficiency data with parameters a & b generated, as determined from lines associated with ^{238}U and ^{232}Th decay (West coast sand sample).

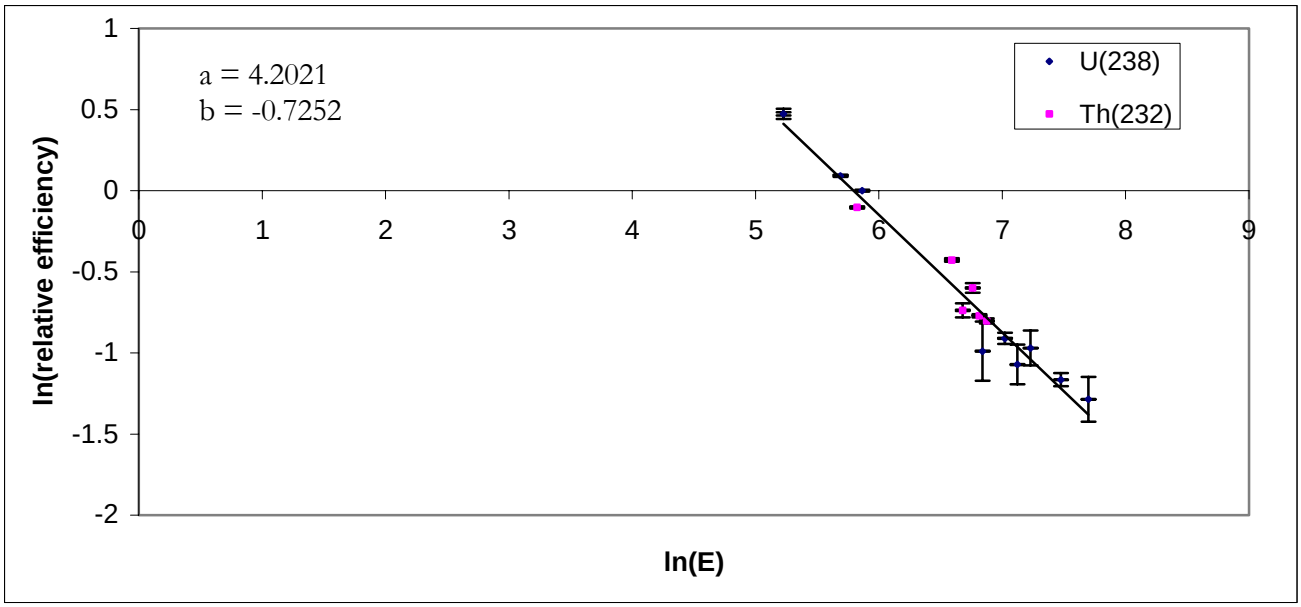

Figure 3.12: A *fit of relative efficiency data with parameters a & b generated, as determined from lines associated with* ^{238}U *and* ^{232}Th *decay (Brick clay).*

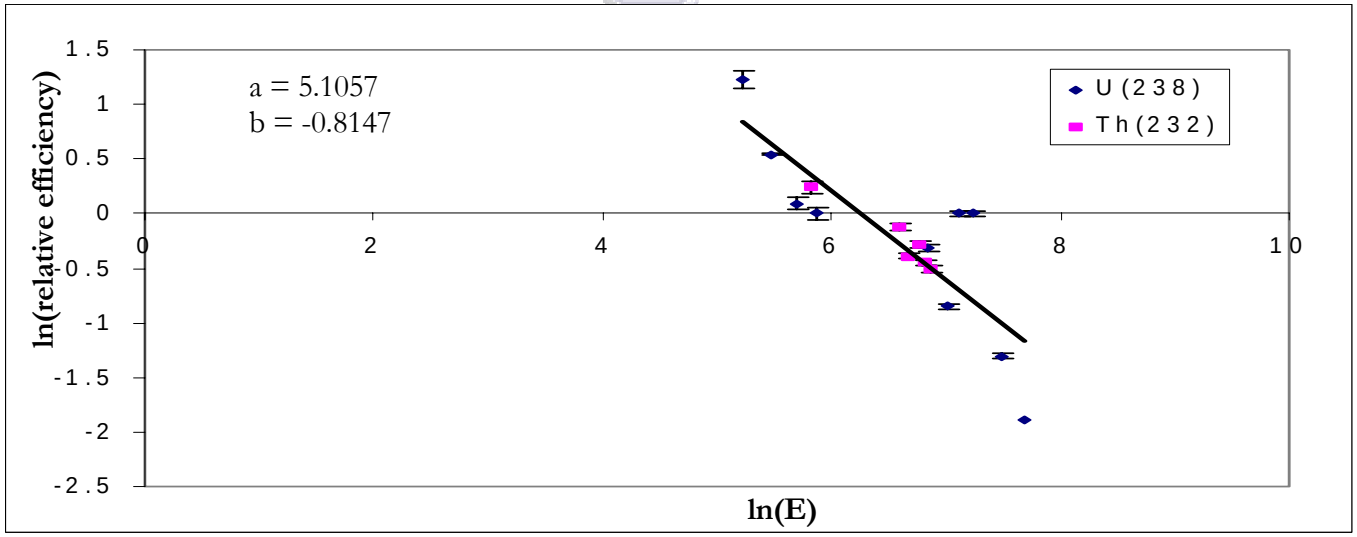

Figure 3.13: A *fit of relative efficiency data with parameters a & b generated, as determined from lines associated with* ^{238}U *and* ^{232}Th *decay (thorium + stearic sample).*

3.1.2 Treatment of uncertainties in WA

The uncertainties contributing to the results in this method were propagated throughout by adding them all in quadrature combinations. An example of the uncertainty due to background subtraction is as follows:

from equation 3.5, it follows that

$$C_{Ni}{}' = C_{Ni} - C_{bi} \pm \sqrt{(\Delta C_{Ni})^2 + (\Delta C_{bi})^2}$$

where
$$\Delta C_{Ni}{}' = \sqrt{(\Delta C_{Ni})^2 + (\Delta C_{bi})^2}\,, \tag{3.11}$$

$\Delta C_{Ni}{}'$ is an uncertainty in the background subtracted net counts. ΔC_{Ni} and ΔC_{bi} are uncertainties due to counting statistics for net and background counts.

Now to get to the relative efficiency, the background subtracted net counts will be divided by the branching ratio, (which also has its specified uncertainty from the manual [EML97]). This now yields the following:

$$\varepsilon_{rel} = \frac{C_{Ni}{}'}{r_b} \tag{3.12}$$

Therefore, the uncertainty in 3.12 will then be given by

$$\Delta\varepsilon_{rel} = \varepsilon_{rel}\sqrt{\left(\frac{\Delta C_{Ni}{}'}{C_{Ni}{}'}\right)^2 + \left(\frac{\Delta r_b}{r_b}\right)^2} \tag{3.13}$$

The uncertainties from the live time and the sample mass were almost negligible and therefore were treated as constants.

Furthermore from equation 3.6,

$$\varepsilon = aE^b$$

the relative uncertainties include the uncertainty in parameters a and b as follows:

$$\Delta\varepsilon^2 = \left(\frac{\partial\varepsilon}{\partial a}\right)^2 \Delta a^2 + \left(\frac{\partial\varepsilon}{\partial b}\right)^2 \Delta b^2 \qquad (3.14)$$

This reduces to

$$\Delta\varepsilon = \varepsilon\sqrt{(E^b)^2\Delta a^2 + \left[E^b(\ln E)a\right]^2 \Delta b^2} \qquad (3.15)$$

which is the uncertainty in the relative uncertainties (ignoring co-variances).

Although the uncertainties in a and b were determined, these uncertainties were not propagated in this study.

The activity concentrations presented in chapter 4 by this method are calculated from intensities of several γ-rays emitted by parent nucleus, and therefore grouped together to produce a weighted average activity per nuclide.
These weighted average activity concentrations in the samples analysed (using the WA method) are presented in Tables 4.1 to 4.9 in chapter 4.

The equations in appendix A were used in the treatment of uncertainties for this method, see also the statistics of counting described in Appendix A.2 to find out how weighted averages are arrived at.

3.2 Full Spectrum Analysis

The important aspects to consider in this method are the use of its full-spectral shape and the so-called 'standard spectra' in the calculation of the activity concentrations of natural radionuclides ^{238}U, ^{232}Th and ^{40}K [Hen01]. The total spectrum comprises a background spectrum and the responses to the activity concentrations of the natural radionuclides. These responses are considered to be proportional to the activity concentrations and require detailed knowledge of the 'standard spectra'. Each of the spectra corresponds to the response of the detector in a particular geometry for a sample containing 1Bq/kg of each nuclide [Hen03].

All the spectral features including the inclusion of the Compton continuum in the spectrum makes this method a good one in the data analysis; and this contributes to the reduction of the statistical uncertainty in the data, especially for relatively short measurements, since in principle more time is required for the accumulation of data with small uncertainties.

3.2.1 Derived standard spectra

Energy calibration was done according to the calibration process already discussed in section 2.1.4. These energy calibrations were done independently for each standard spectrum.

In general the relation between energy and channel number of the sample spectra measured deviates from that of the standard spectra. These deviations can be attributed for example to temperature variations, which consequently result in the varying in time of the relation between energy and channel number [Kno79].

To take the differences in amplifications for samples taken at different times into account, all spectra were re-binned[5] using the energy calibration parameters so that each spectrum has the same channel/energy relationship, chosen as 1 keV per channel for convenience.

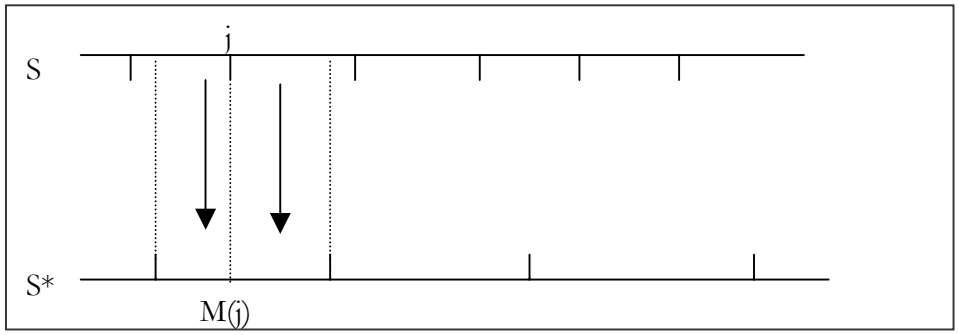

Figure 3.14: The contents of channels of the measured spectrum S redistributed to the re-binned spectrum S.*

The channel i of the re-binned spectrum S* can be mapped onto the channels j of the measured spectrum S with a function i = M(j) ; and the contents of the channels of the measured spectrums can then be redistributed over the channels of the re-binned spectrum S* [Sta97]. A small FORTRAN program was developed to execute such a task see (appendix B).

The re-binning exercise is needed to try and correct for the small differences in the energy calibration between the standard and sample spectra.

The spectra were normalized by dividing each channel by the product of source mass, live time and activity concentration. The flow chart in Figure 3.15 shows a summary of how standard spectra were obtained.

[5] channels converted to equivalent energy values per bin

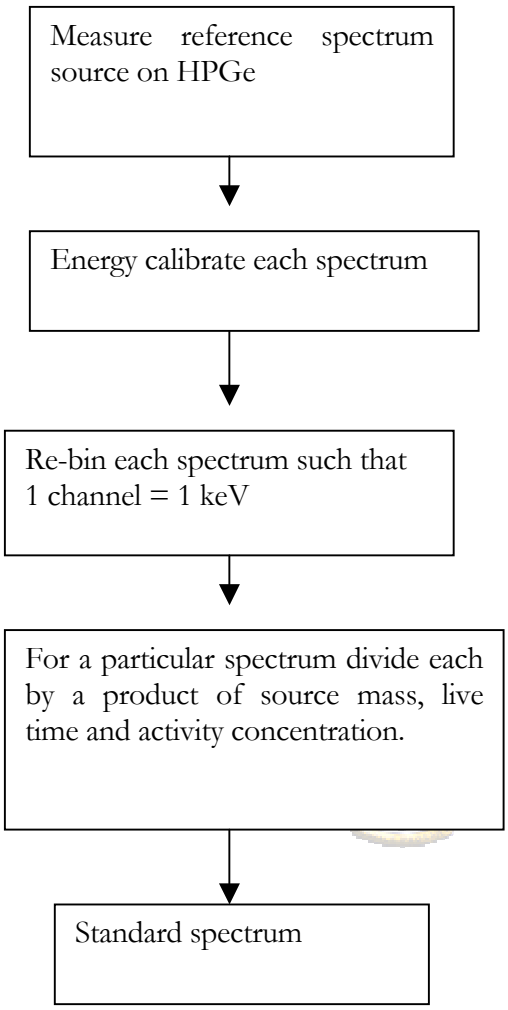

Figure 3.15: Flow chart showing how a standard spectrum was obtained.

Figures 3.16, 3.17 and 3.18 show the re-binned spectra for the three standard sources used, which are those for the ^{238}U, ^{232}Th and ^{40}K, respectively.

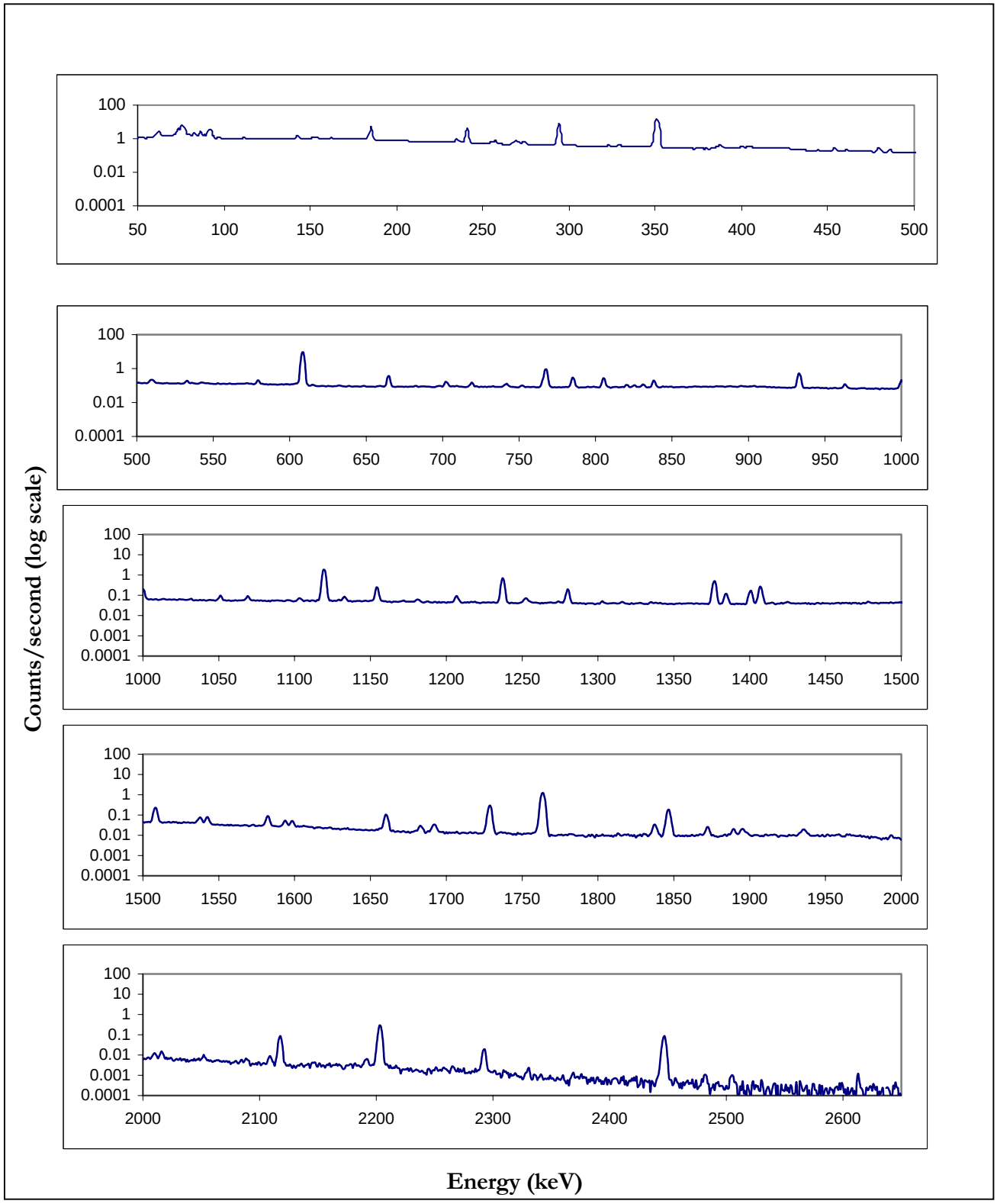

Figure 3.16: The background subtracted re-binned standard spectrum for uranium.

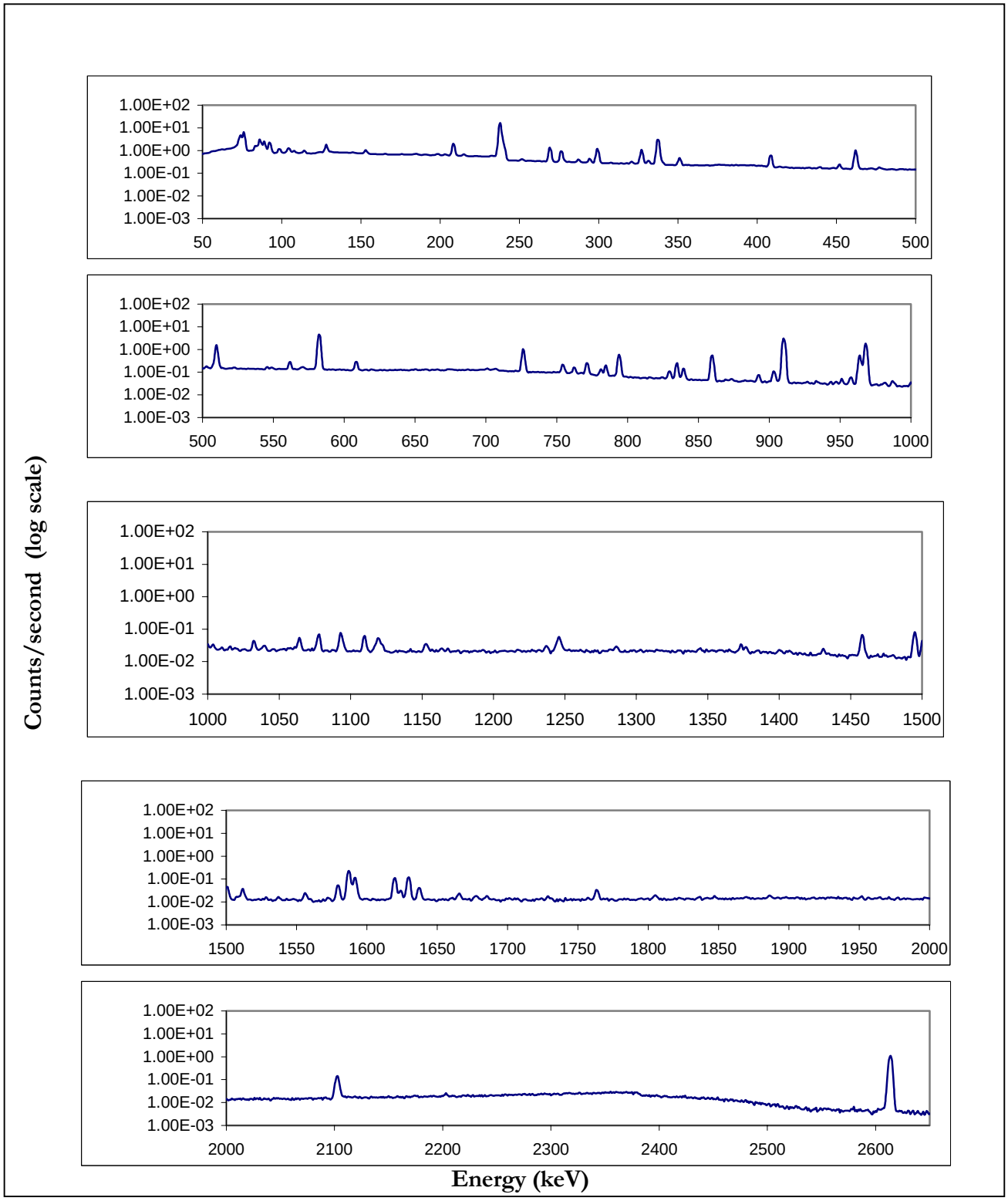

Figure 3.17: The background subtracted re-binned standard spectrum for thorium.

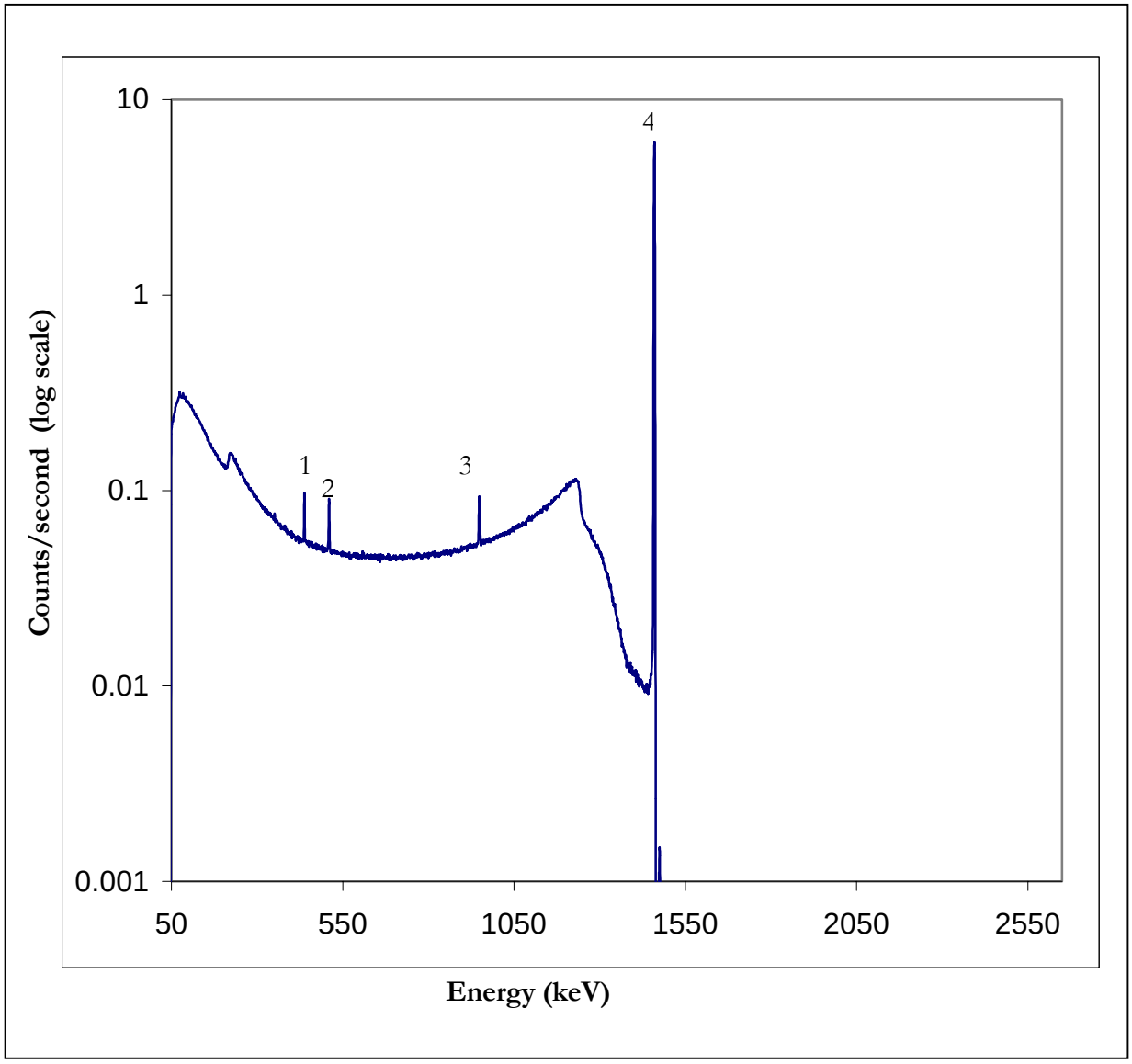

Figure 3.18: The background subtracted re-binned standard spectrum for potassium. (Peaks labeled 1, 2, 3 and 4 are the full-energy peaks 438 keV due to second escape peak, the annihilation peak (511 keV), the first escape peak (950 keV) and the 1461 keV due to ^{40}K respectively.

3.2.2 Chi-square minimization technique

Once the fixed relation between energy and channel number has been obtained, the least-square method is used to find the optimal activity concentrations using the Physica software [Chu94]. In this method the activity concentrations will follow from a fit of the calculated standard spectrum to the measured one [Hen01]. In the FSA the measured spectrum Y is described as the sum of the standard spectra X_j multiplied by the activity concentrations C_j for the individual radionuclides. The background was subtracted from the individual spectrum in each measurement before fitting.

If a complex spectrum has to be decomposed into j known components, the intensity C_j of each component relative to that of its standard is determined by the requirement that

$$\chi_{red}^{2} = \frac{1}{n-m} \sum_{i=lec}^{n=hec} w(i) \left[Y(i) - \sum_{j} C_j X_j(i) \right]^2 \qquad (3.16)$$

should be a minimum [Qui72,Pre92,Hen10]. *Y (i)* and $X_j(i)$ are counts in channel *i* recorded under the same experimental conditions. *j* represents the number of standard spectra used, with j_{max}= 3 since three standards sources (^{238}U, ^{232}Th, and ^{40}K) were used in this study; *i* = lec and n = hec are low energy and high energy cut-offs used during the minimization procedure. The factor n-m represents the number of degrees of freedom where n is the number of data points and m the number of free parameters. The choice of n-m assumes all the channels to be independent [Hen03]. The weight $w(i)$ factor is given as the inverse of the square of the standard deviation. The standard deviations for each source were added in quadrature combinations to the sample's standard deviation.

The important part of equation 3.16 for FSA is in the definition of the weights *w(i)* and this will be discussed next.

Definition of weights:

Let

$$A_i \pm \sqrt{A}_i = \Delta A$$

and

$$\mathrm{B}_i \pm \sqrt{B}_i = \Delta B$$

represent gross counts in the ith channel of the sample and background spectrum respectively.

Now the **real count rate** obtained after background subtraction is given by

$$CR = \left(\frac{A_i}{t_A} - \frac{B_i}{t_B}\right) \pm \sqrt{\left(\frac{\Delta A}{t_A}\right)^2 + \left(\frac{\Delta B}{t_B}\right)^2} \tag{3.17}$$

Were t_A and t_B are live times for the measured sample and background respectively. The uncertainty in the background-subtracted count rates is given by

$$\sigma_i = \sqrt{\left(\frac{\Delta A_i}{t_A}\right)^2 + \left(\frac{\Delta B_i}{t_B}\right)^2} \tag{3.18}$$

The errors in (3.16) were added in quadrature combinations to give the total standard deviation,

$$\sigma_i^{\,2} = C^2{}_K \frac{\Delta A_K^{\,2}}{t_K^{\,2}} + \frac{\Delta A_S^{\,2}}{t_S^{\,2}} + C^2{}_{Th} \frac{\Delta A_{Th}^{\,2}}{t_{Th}^{\,2}} + C^2{}_U \frac{\Delta A_U^{\,2}}{t_U^{\,2}} + \left(\frac{\Delta B_i}{t_B}\right)^2 \left(1 + C_K^2 + C_U^2 + C_{Th}^2\right) \tag{3.19}$$

where the subscripts S, K, Th and U are the sample, potassium, thorium, and uranium spectra respectively, and with t being the live time associated with the spectra. The background B was subtracted from each spectrum, that is in all three standard spectra plus the sample one.

The weighting is then given by the inverse of the square of the standard deviations as follows:

$$w(i) = 1/\sigma_i^2 \tag{3.20}$$

$$\text{Therefore } w(i) = \frac{1}{[\sigma_S(i)]^2 + \sum_{j=1}^{3}\left[C_j \sigma_{X_j}(i)\right]^2} \tag{3.21}$$

where σ_S is the standard deviation for the sample measurement

The minimization is such that

$$\frac{\partial \chi^2}{\partial c_j} = 0 \qquad (\text{for all j}). \tag{3.22}$$

Several measurements on different samples were made with both methods and the Tables 2.3 and 2.6 show the information regarding such samples.

The fit is reasonably good in general, except for low energy cut-off energies less than about 300 keV. This is due to the self-absorptions at lower energies as discussed later in chapter 4. The $\chi^2_{reduced}$ has been calculated for low energy cut-off energies ranging from 50 keV up to 300 keV (in steps of 50 keV) and with a high energy cut-off of 2650 keV. These $\chi^2_{reduced}$ values obtained are shown in Figure 3.19 for the different cut-off energies.

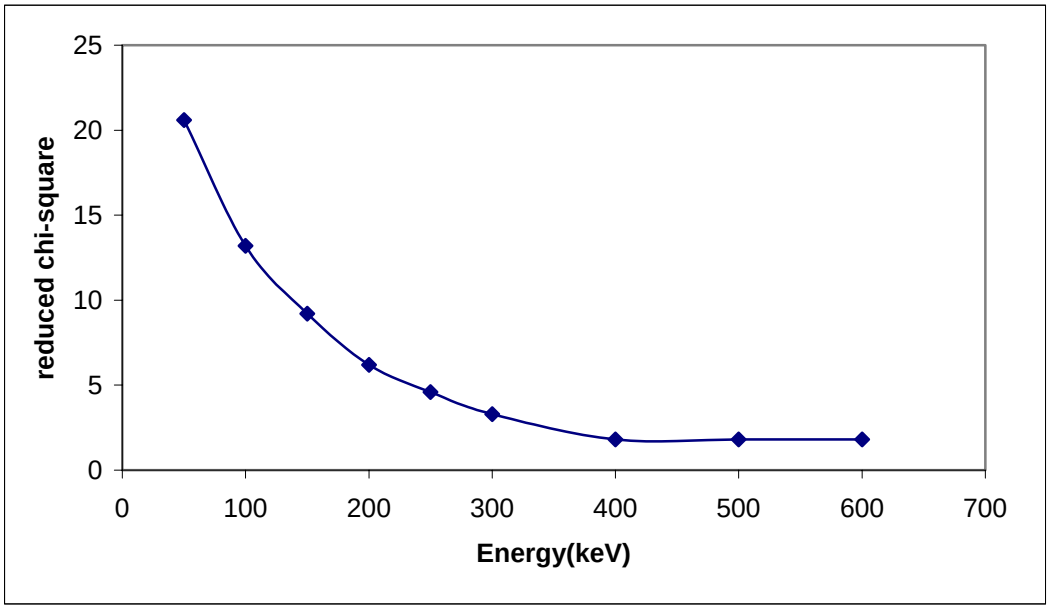

Figure 3.19: Reduced chi-square (measure of the goodness of fit) for FSA fit of Westonaria sample as a function of lower energy cut-off (lec), (see equation 3.16).

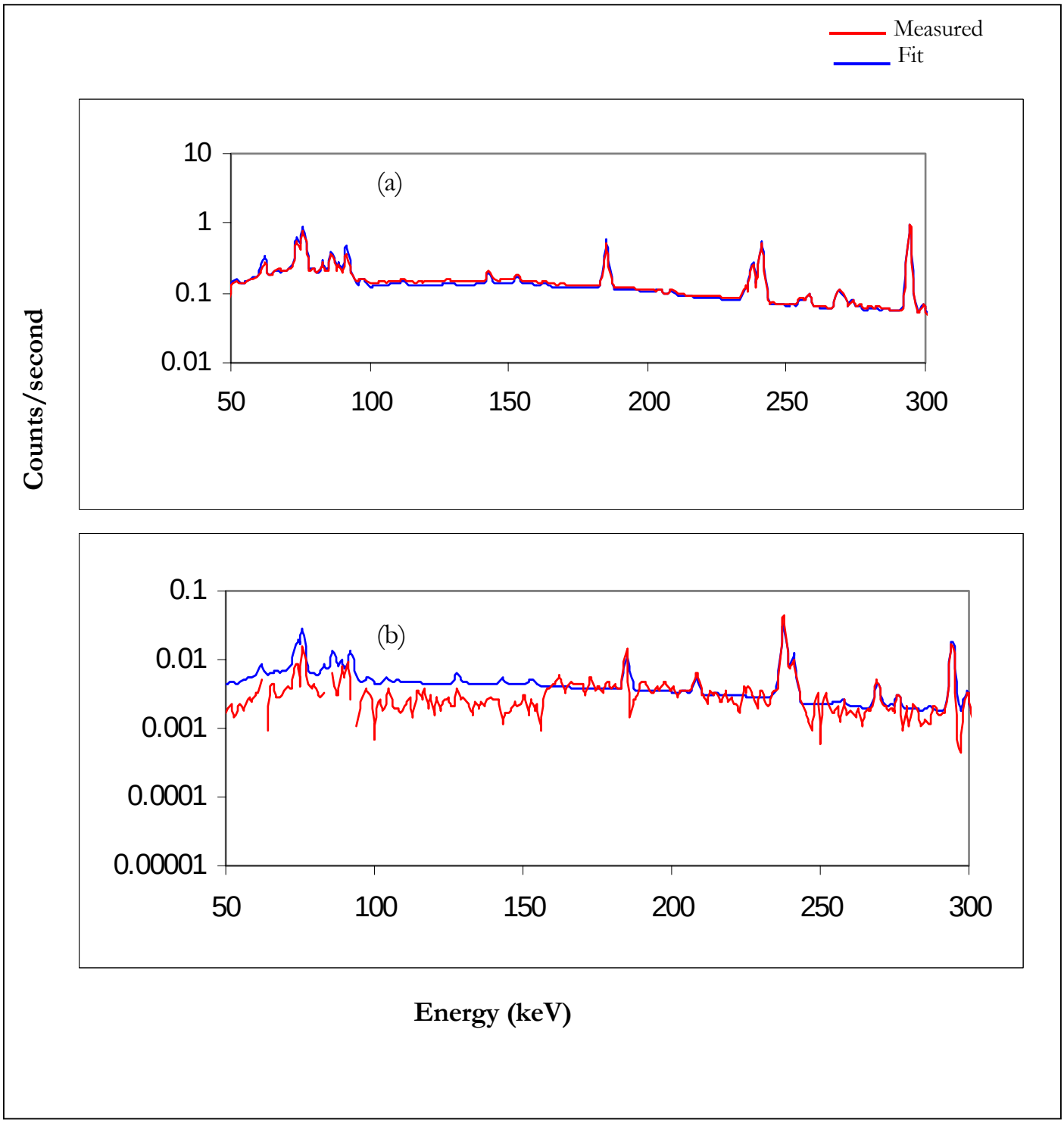

Figure 3.20: The background subtracted Kloof (a)and West Coast(b) sample spectra and their fit ***for a long measurement*** *(below 300 keV)*

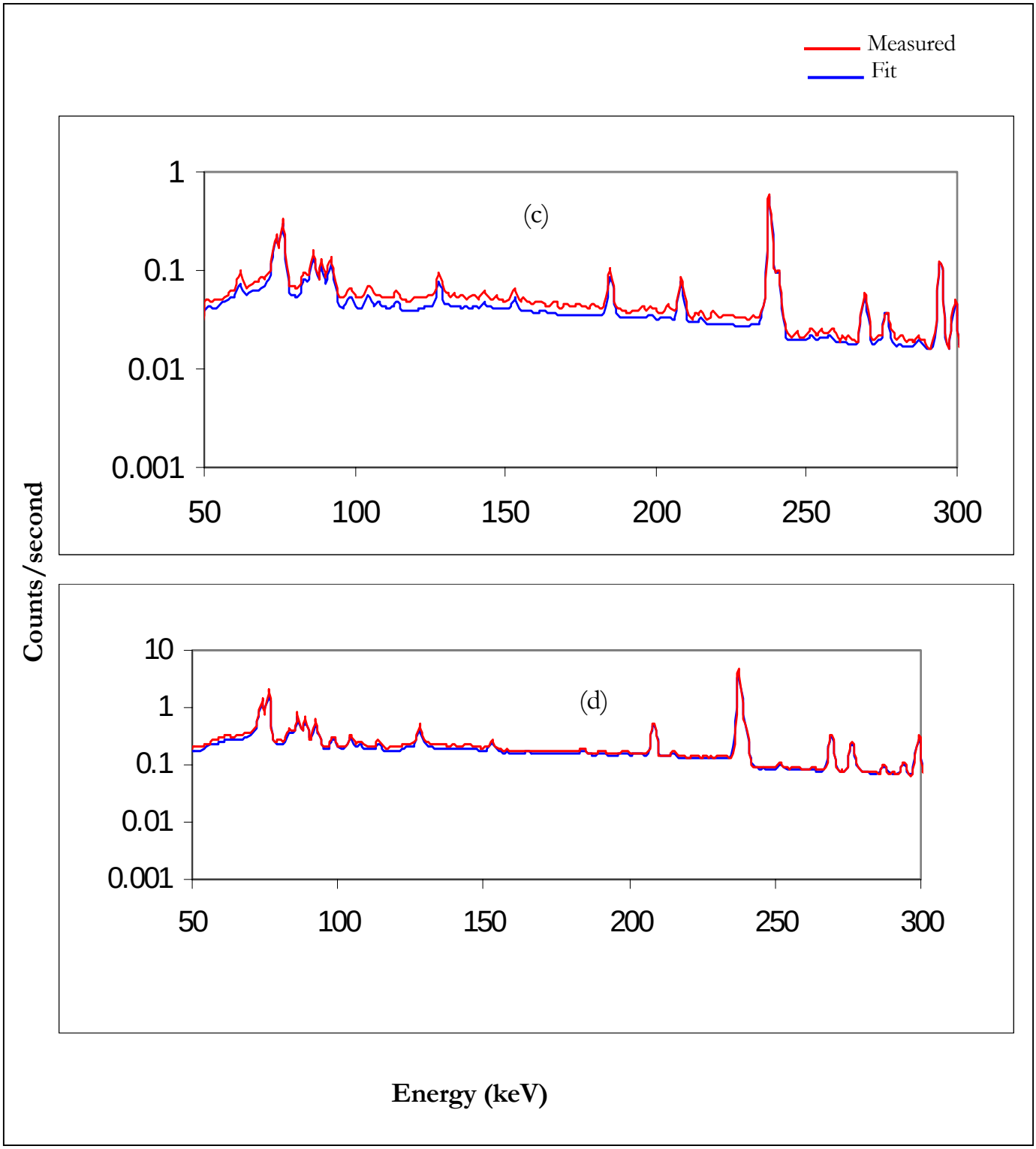

Figure 3.21: The background subtracted Brick clay (c) and thorium sample(d) spectra and their fit ***for a long measurement*** *(below 300 keV).*

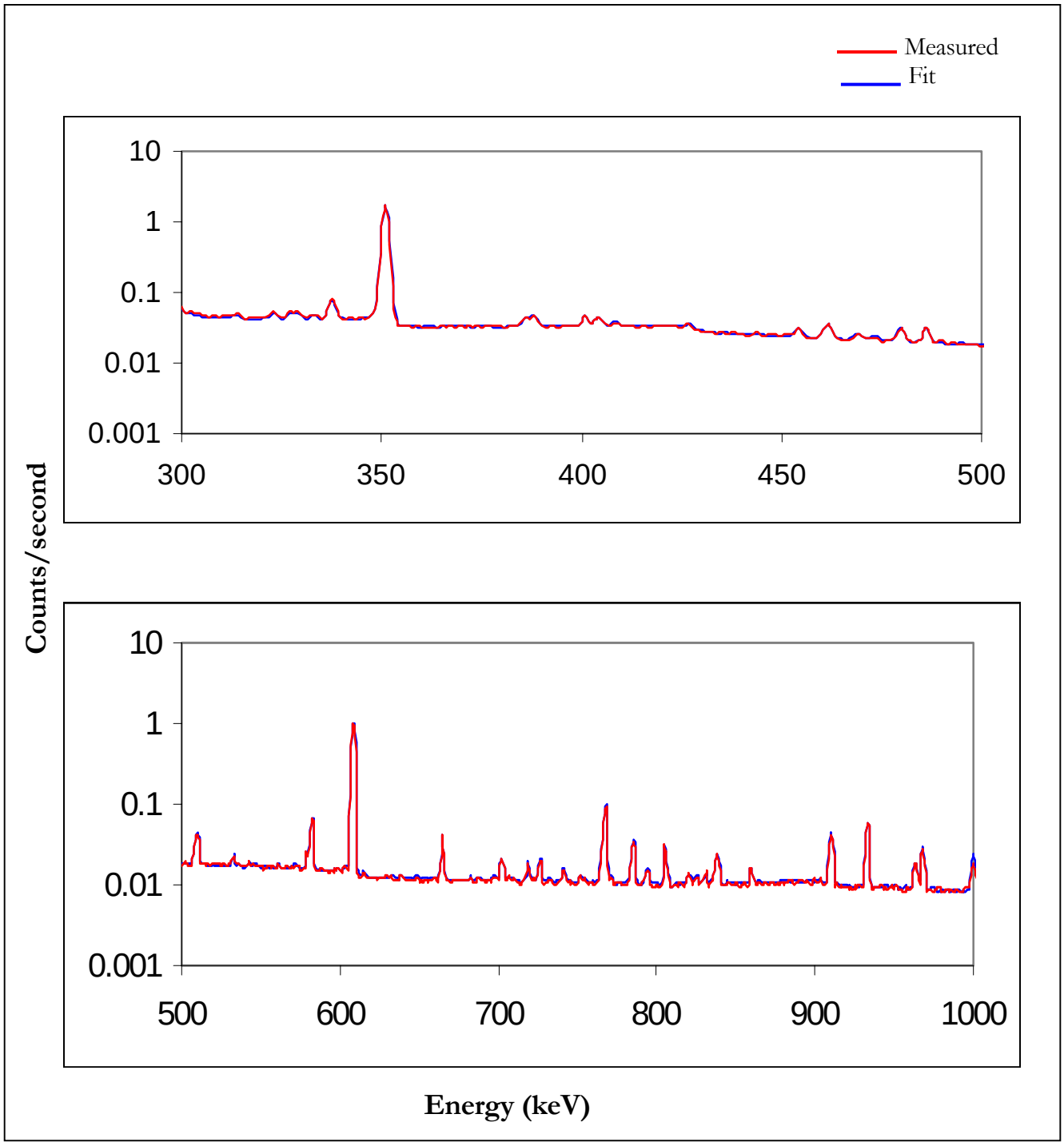

Figure 3.22: The background subtracted Kloof sample spectrum ***for a long measurement*** *and the fit (for energies between 300 and 1000 keV).*

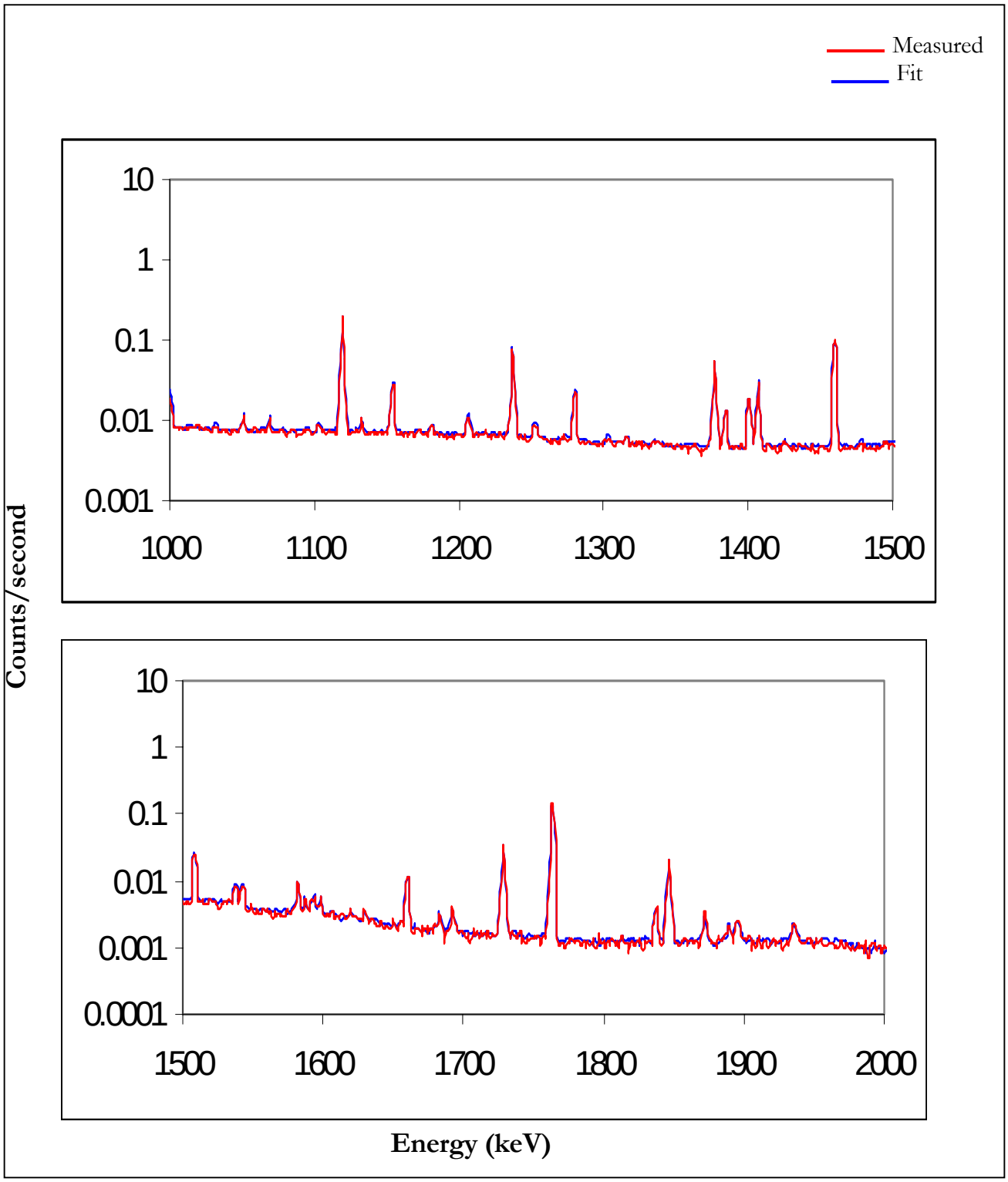

Figure 3.23: The background subtracted Kloof sample spectrum ***for a long measurement*** *and the fit (for energies between 1000 and 2000 keV).*

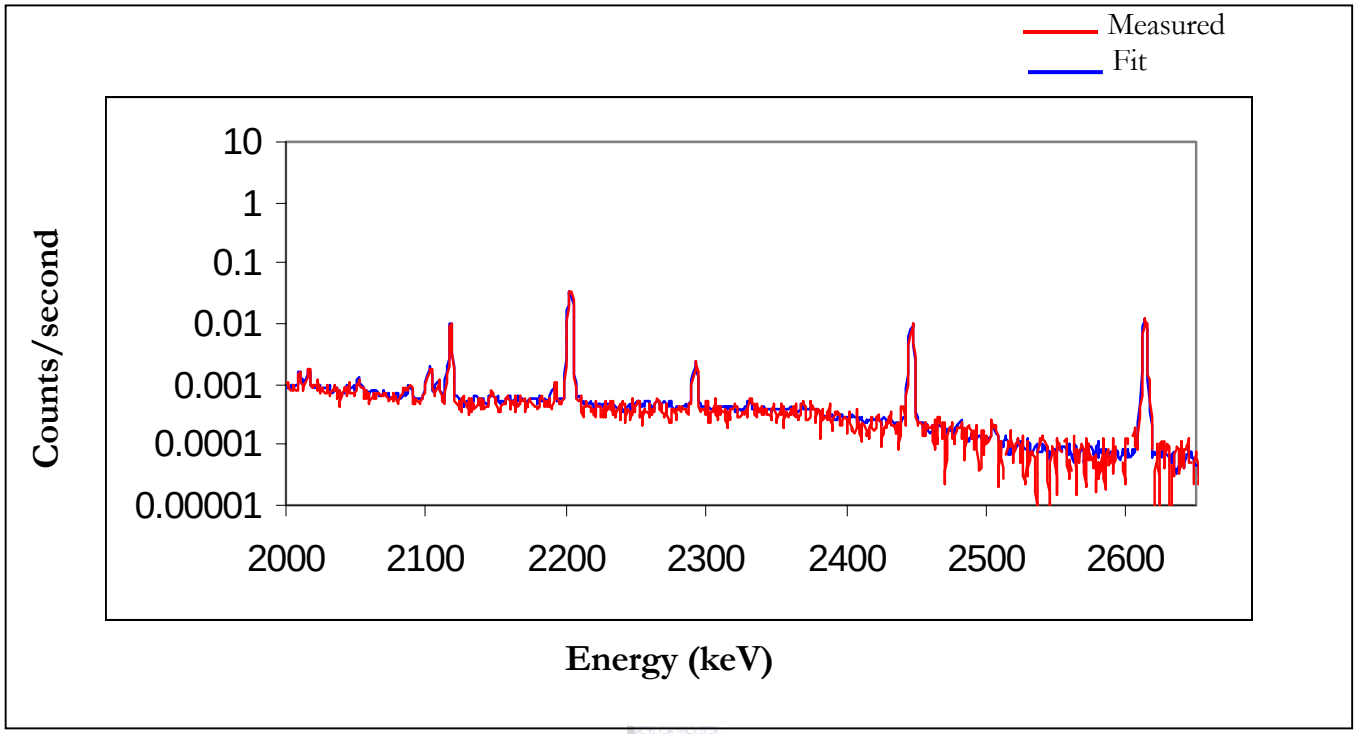

Figure 3.24: The background subtracted Kloof sample spectrum ***for a long measurement*** *and the fit (for energies between 2000 and 2650 keV).*

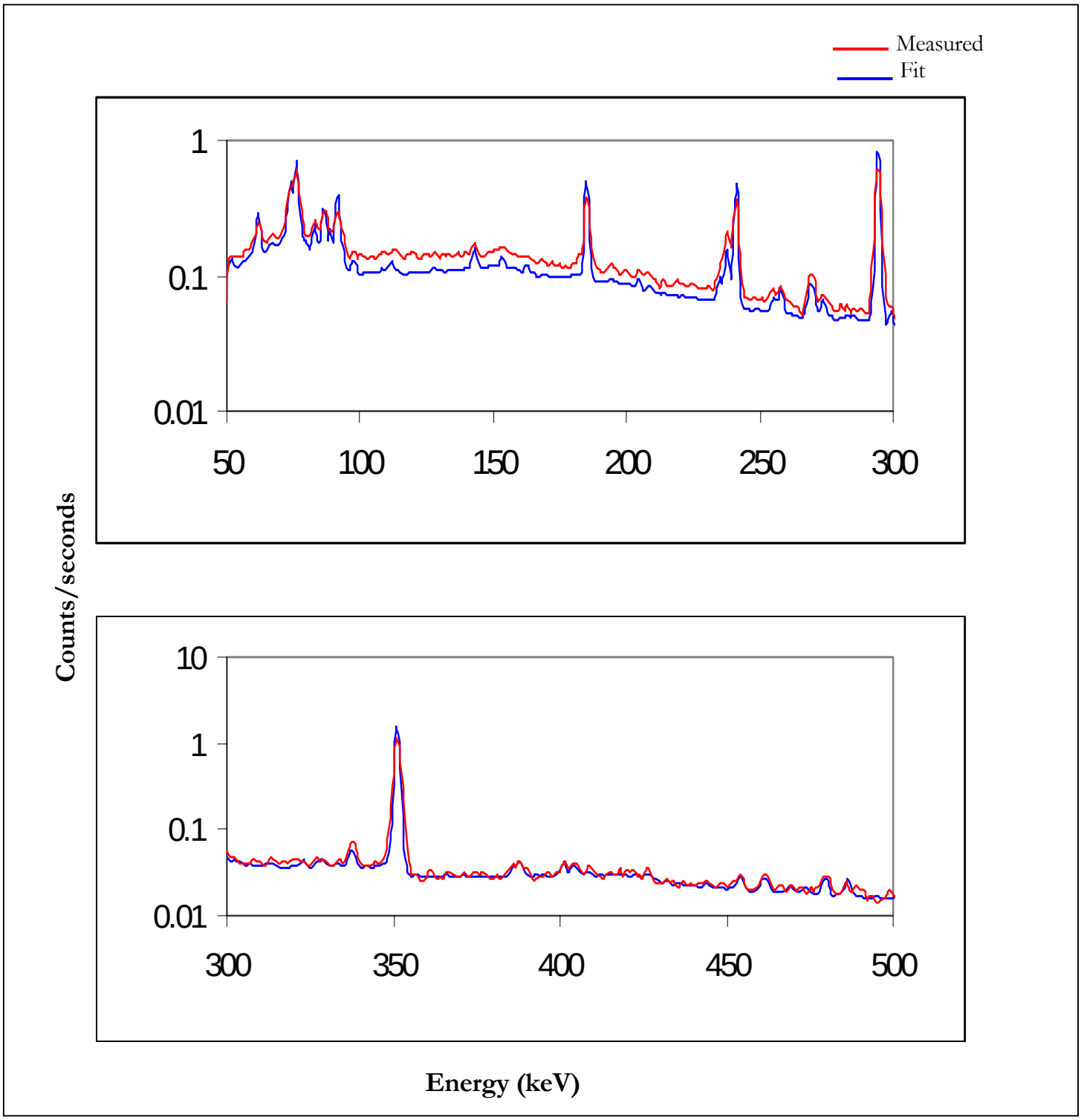

Figure 3.25: The background subtracted Kloof sample spectrum for a ***short measurement*** *and the fit (for energies between 50 and 500 keV).*

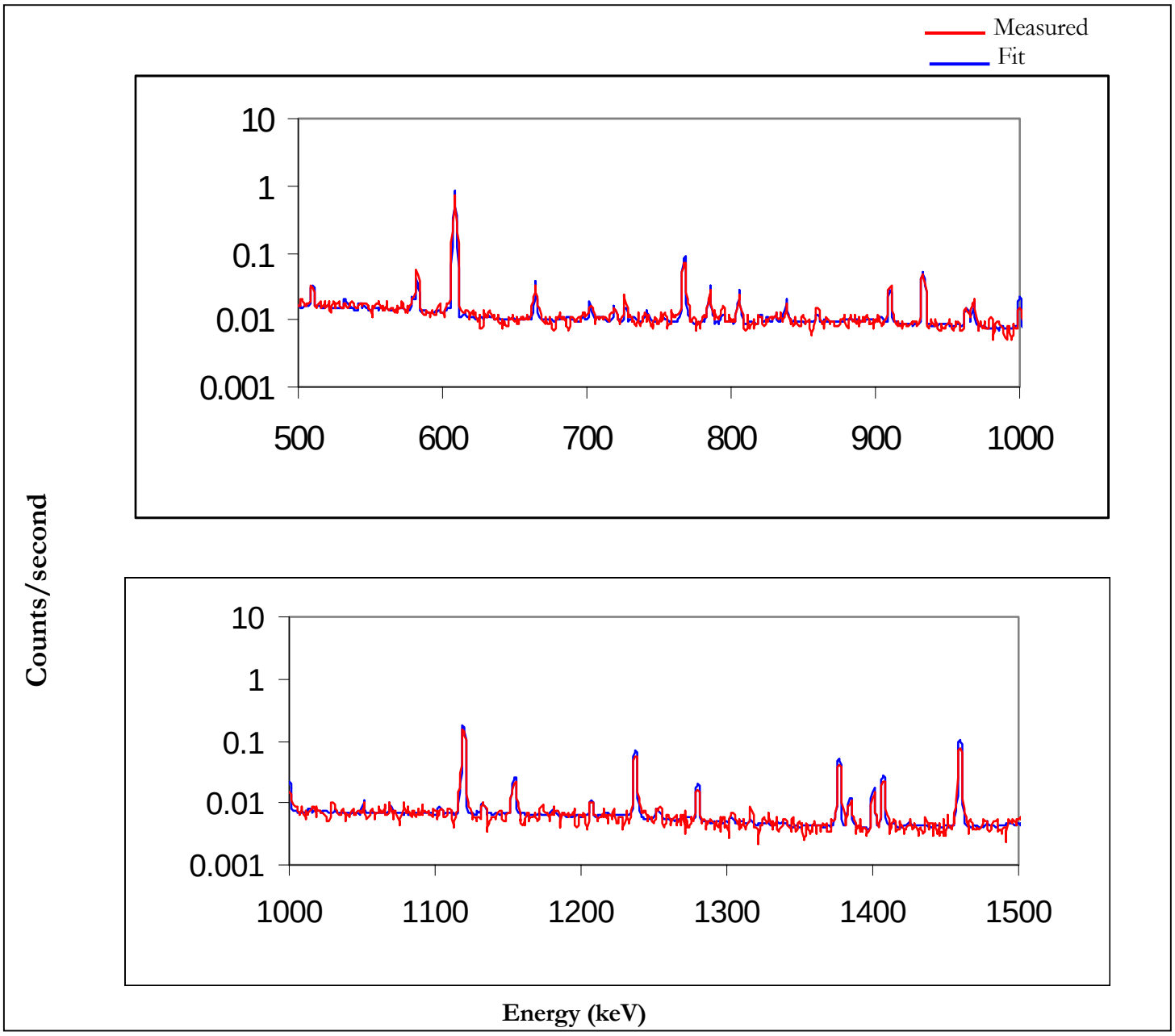

Figure 3.26: The background subtracted Kloof sample spectrum for a ***short measurement*** *and the fit (for energies between 500 and 1500 keV).*

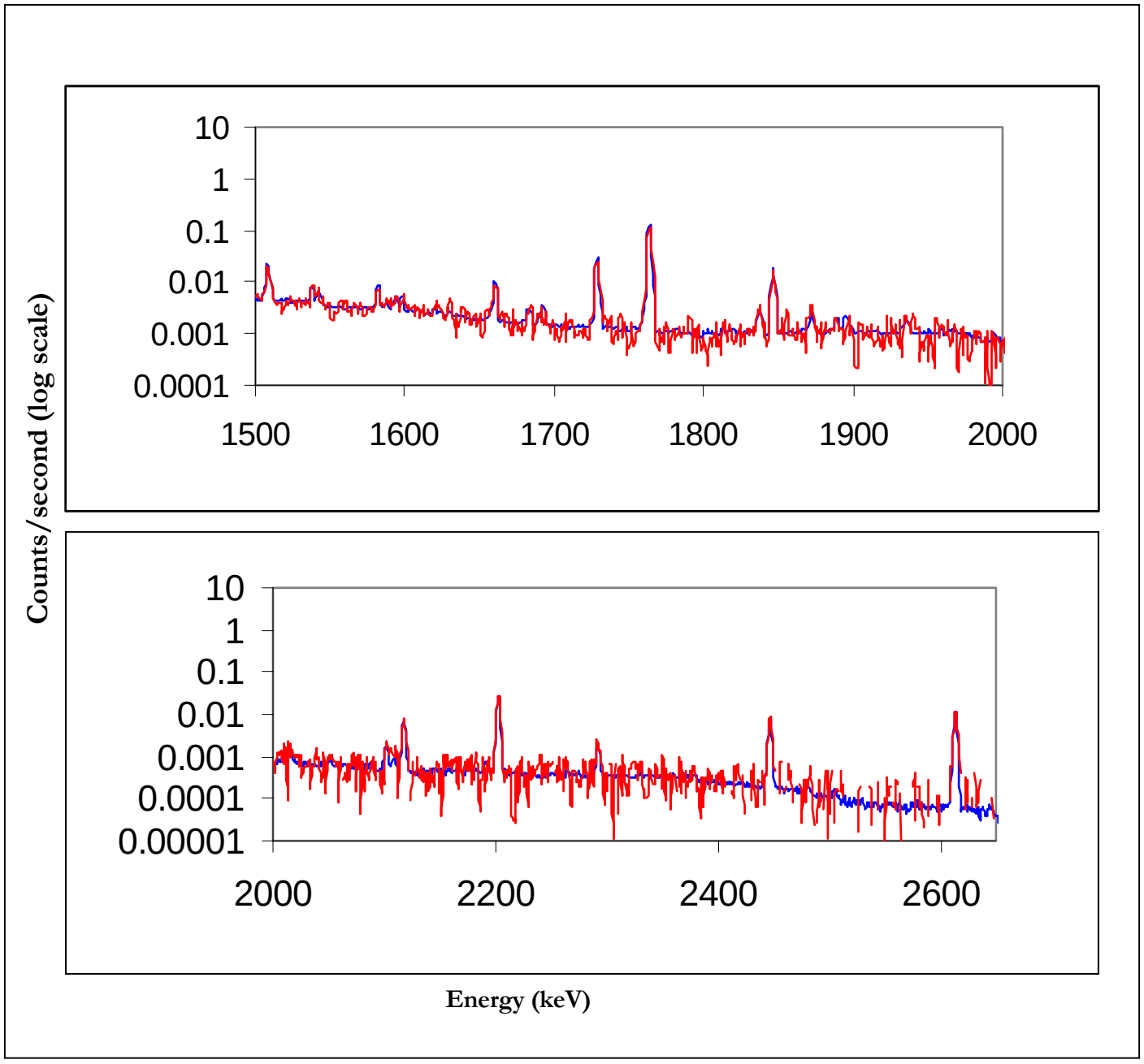

Figure 3.27: The background subtracted Kloof sample spectrum for a ***short measurement*** *and the fit (for energies between 2000 and 2650 keV).*

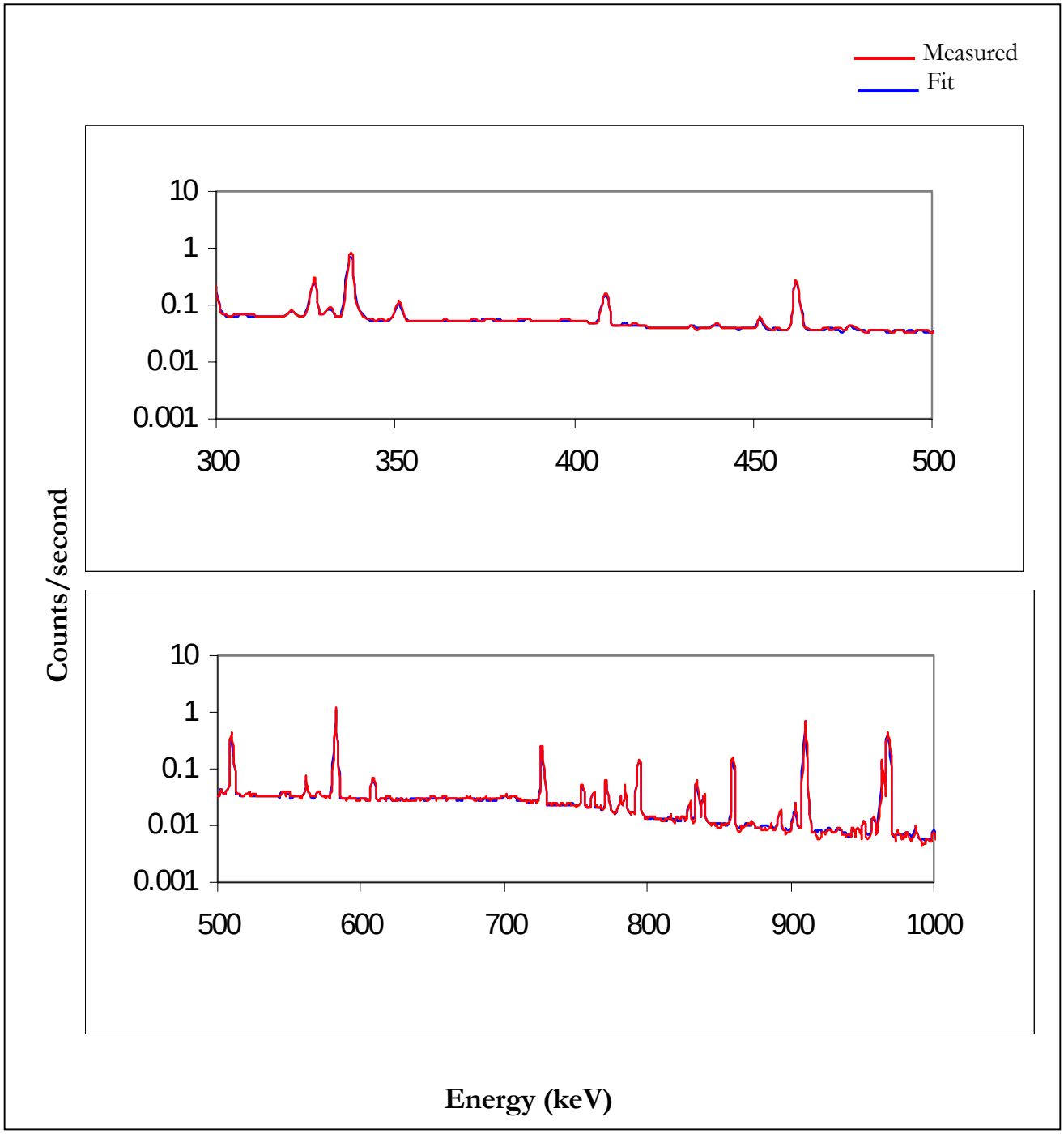

Figure 3.28: The background subtracted thorium + stearic acid sample spectrum and the fit for a ***long measurement*** *(for energies between 300 and 1000 keV).*

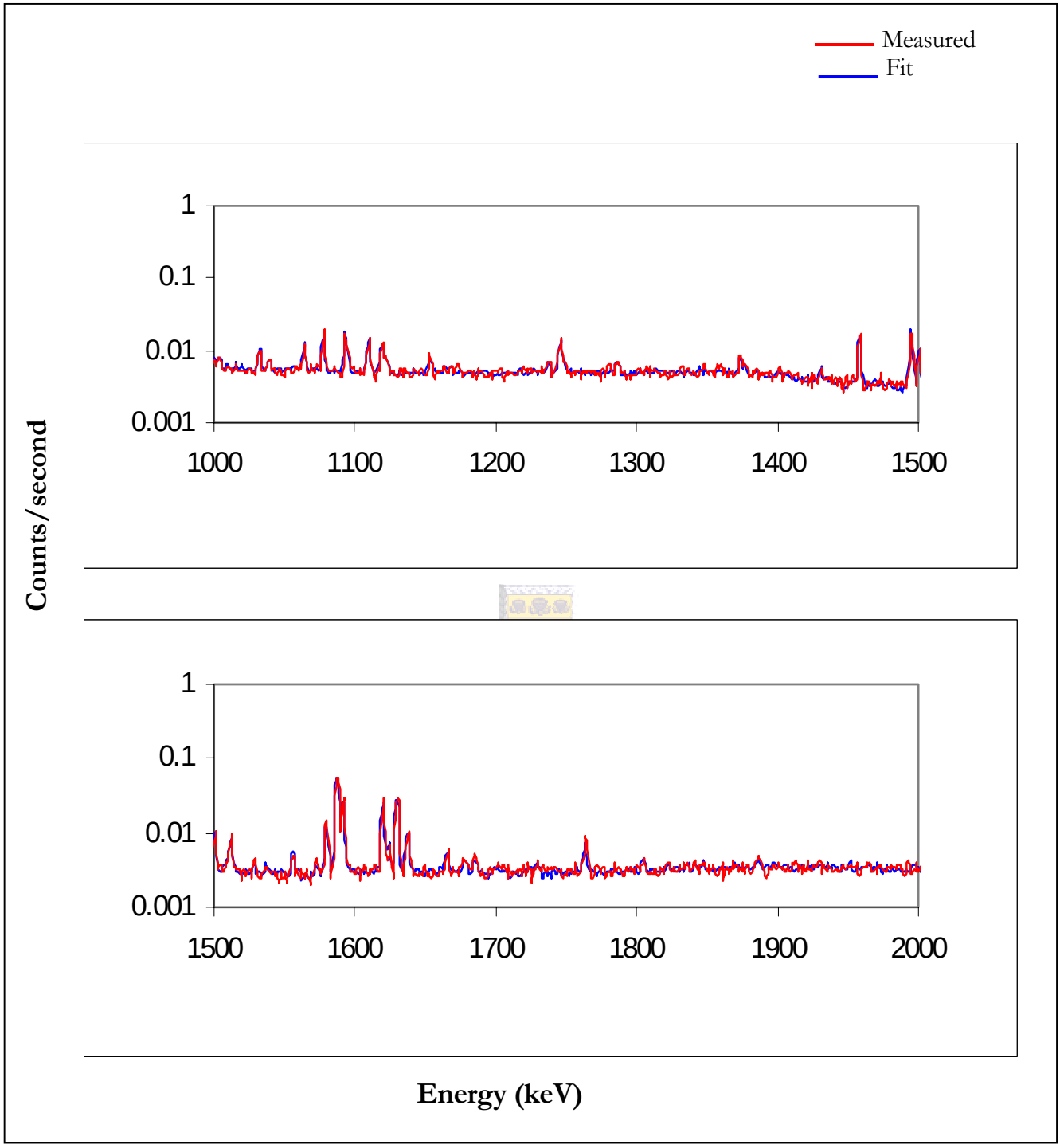

Figure 3.29: The background subtracted thorium + stearic acid sample spectrum and the fit for a ***long measurement*** *(for energies between 1000 and 2000 keV).*

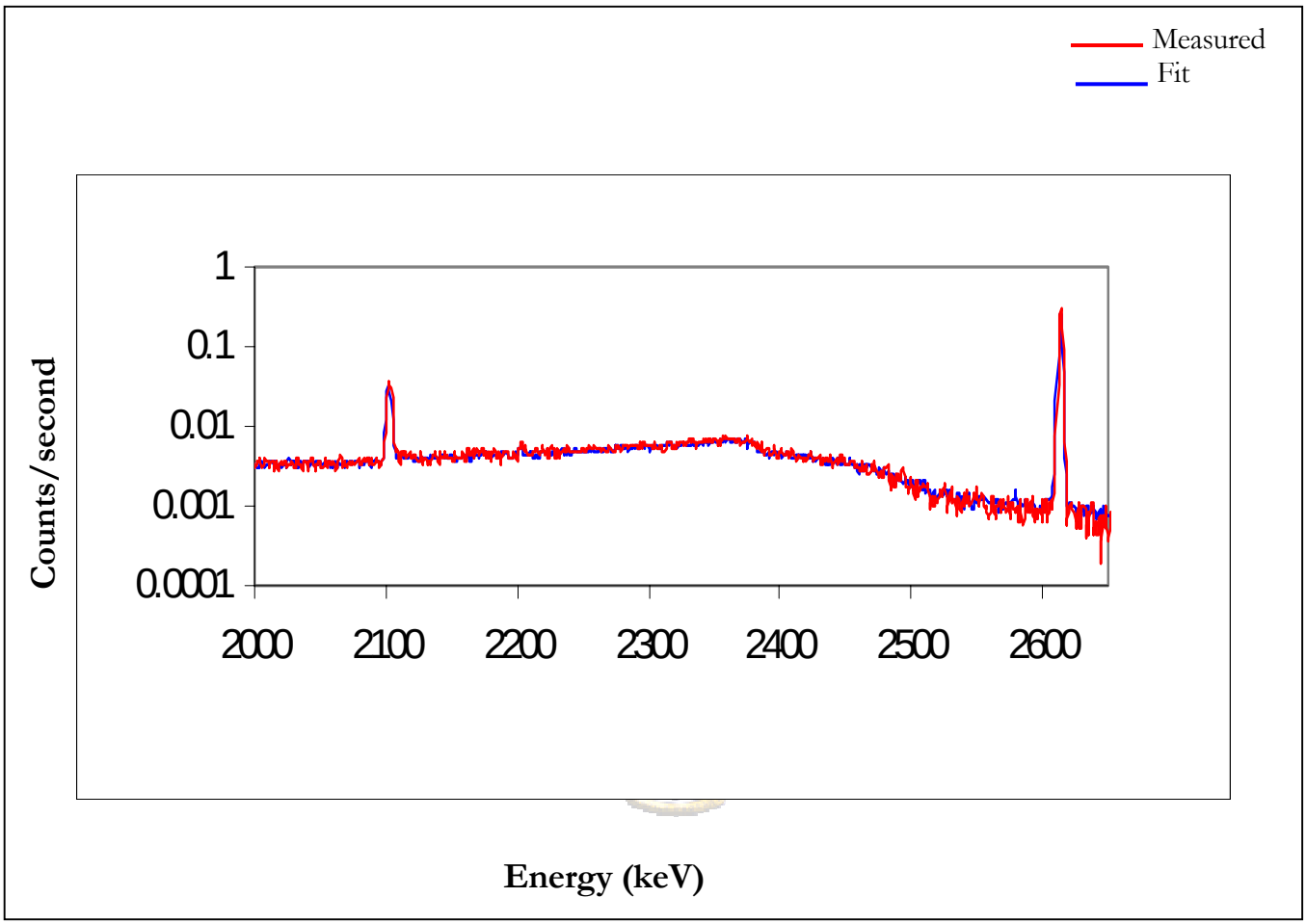

*Figure 3.30: The background subtracted thorium + stearic acid sample spectrum and the fit for a **long measurement** (for energies between 2000 and 2600 keV).*

The fit is not good for the energies ranging from 50 keV to about 300 keV as is witnessed from Figures 3.20 b and 3.21c. This is due to self-absorption effects, a phenomenon to be discussed in the next chapter.

In order to see how good a fit is, two energy lines from two samples of different densities were chosen. The Figure 3.31 shows how good the fit is at the 609 keV (^{214}Bi line) for the Kloof sample, while Figure 3.32 shows the fit for the 583 keV (^{208}Tl line) from the thorium + stearic acid sample.

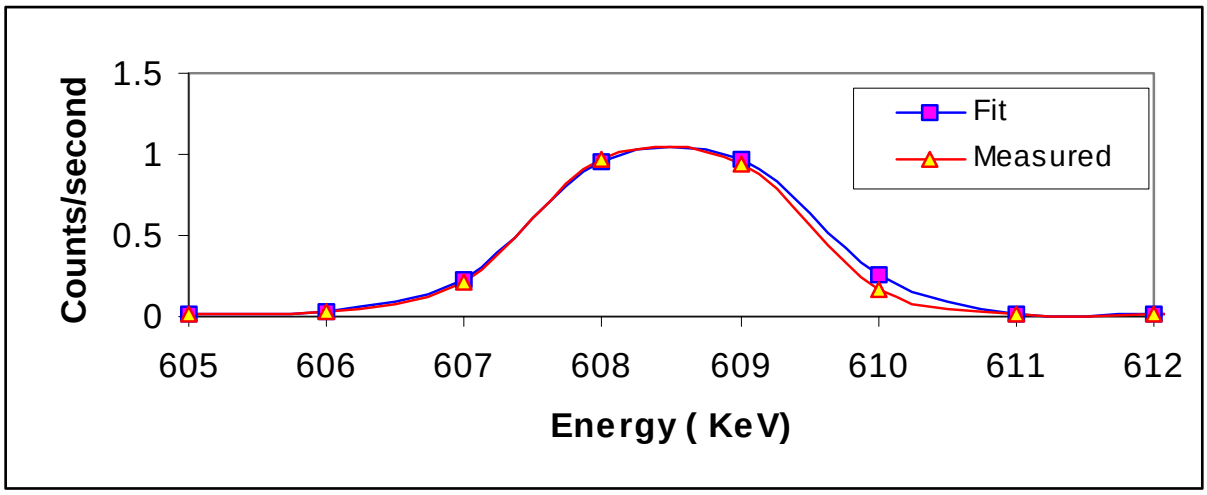

Figure 3.31: A typical 609 keV peak due to ^{214}Bi, (for Kloof sample number 6) with a fit.

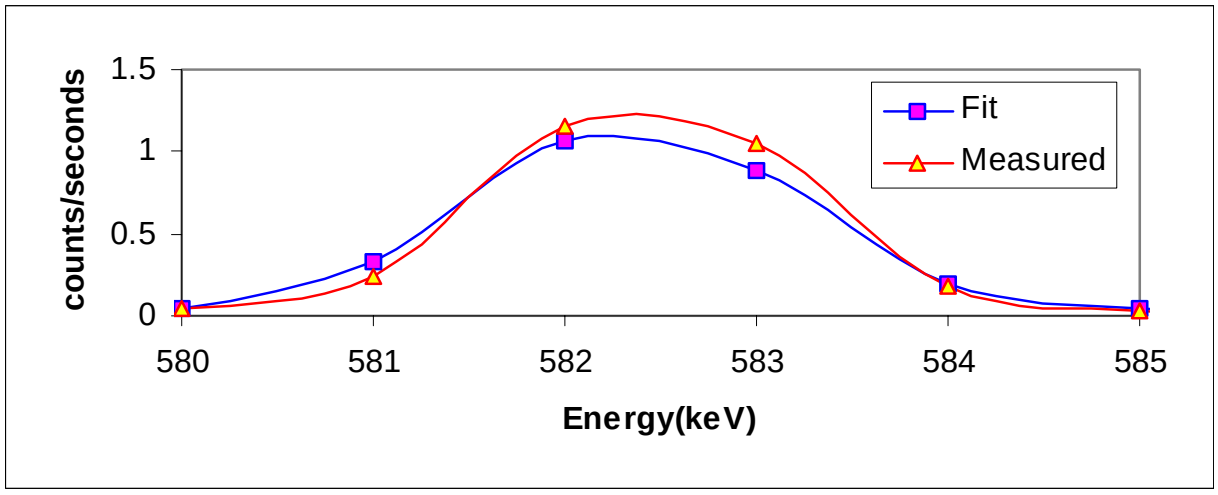

Figure 3.32: A typical 583 keV peak due to ^{208}Tl, (for thorium + stearic acid sample number 5) with a fit.

3.2.3 Treatment of uncertainties for FSA

The uncertainties in C_j from equation 3.16 were obtained using the Gauss-Newton method. This method proceeds by iterative means to calculate ΔC such that

$$C_1 = C_0 + \Delta C \,. \tag{3.23}$$

the aim of this method is to find a ΔC such that C_1 is a better approximation to the best least square fit solution [Chu94,Pre92]. If the method is repeated iteratively the series C_1,C_2 ,C_3…. will converge until the sum of the squares of the differences between the data points and the function being fitted is a minimum.

To accomplish this, the function *f (x,C)* is expanded in a Taylor's series about the point $C = C_0$ and only the first order terms are kept [Chu94].

$$f(x,C) = f(x,C_0) + \frac{\partial f(x,C_0)\Delta C}{\partial C} \tag{3.24}$$

The equation above is an exact equality when f is linear in the parameters C that is all second-order and higher derivatives are zero.

The problem then is to minimize

$$\sum_{k=1}^{N} \delta_k^2 = \sum_{k=1}^{N} w_k \left[y_k - f(x_k, C_0) - \frac{\partial f(x_{k,} C_0)\Delta C}{\partial C} \right]^2$$

for a system with M parameters, this becomes

$$= \sum_{k=1}^{N} w_k \left[y_k - f(x_k, C_0) - \sum_{j=1}^{M} \frac{\partial f(x_{k,} C_0)\Delta C_j}{\partial C_j} \right]^2 \tag{3.25}$$

If the above expression is differentiated with respect to each of the unknowns, ΔC_j, and the resulting expressions are set to zero, the problem reduces to solving the matrix equation

$$A\Delta C = r \quad \text{where } A = (a_{ij}), \qquad r = (r_i)$$

and
$$a_{ij} = \sum_{K=1}^{N} w_k \frac{\partial f(x_k, C_0)}{\partial p_i} \frac{\partial f(x_k, C_0)}{\partial p_j} \qquad \text{for} \qquad i, j = 1,\ldots,M \tag{3.26}$$

$$r_i = \sum_{k=1}^{N} w_k [y_k - f(x_k, C_0)] \frac{\partial f(x_k, C_0)}{\partial c_i} \qquad \text{for} \qquad i = 1,\ldots,M \tag{3.27}$$

$\sum_{k=1}^{N} \delta_k^2$ is zero at the minimum provided the Gauss-Newton method is locally convergent, The advantage of this method is that linear least squares problems are solved in one iteration.

An indication of the accuracy of the fit is displayed in the output of the Physica program as E_1 and E_2 where

$$E_1 = \sqrt{b_{ii}} \quad \text{for} \quad i=1,\ldots,M \tag{3.28}$$

where b_{ii} are the diagonal elements of $B = A^{-1}$, the inverse of the matrix A. B is called the covariance matrix and E_1 is referred to as the root mean square statistical error of estimate. The root mean square total error of estimate, or standard error, is displayed under E_2 where

$$E_2 = E_1 \left[\sum_{K=1}^{N} w_K \delta_k{}^2 (N - M) \right]^{1/2} \quad \text{for } j = 1,\ldots,M \tag{3.29}$$

Therefore the accuracy of the parameters in a linear fit is

$C_i \pm E_{2i}$ *for* $j = 1,\ldots,M$

Chapter 4

Results and Discussion

In this chapter the activity concentrations of ^{238}U, ^{232}Th and ^{40}K, in the samples analysed, as derived from Windows Analysis and Full Spectrum Analysis are presented and compared.

4.1 WA results

The activity concentrations and associated uncertainties as derived using long live time measurements are given in Tables 4.1 - 4.5.

Nuclide	Energies (keV)	Activity Concentration (Bq/kg)	Full-energy peak Absolute efficiency	Weighted Average Activity Concentration (Bq/kg)
^{238}U series				
$^{226}Ra/^{238}U$	186.1	***305.4 ± 5.0***	0.0410	**320 ± 5**
^{214}Pb	295.1	***328.9 ± 2.9***	0.0295	
^{214}Pb	352.0	***333.7 ± 2.7***	0.0260	
^{214}Bi	934.0	***276.8 ± 10.2***	0.0129	
^{214}Bi	1120.3	***295.7 ± 3.5***	0.0113	
^{214}Bi	1238.1	***299.1 ± 6.5***	0.0105	
^{214}Bi	1377.7	***328.9 ± 8.3***	0.00980	
^{214}Bi	1765.5	***322.1 ± 3.8***	0.00821	
^{214}Bi	2204.1	***319.2 ± 6.3***	0.00700	
^{232}Th series				
^{228}Ac	338.4	***25.1 ± 1.5***	0.0267	**21 ± 1**
^{212}Bi	727.3	***19.3 ± 3.0***	0.0154	
^{228}Ac	794.8	***19.5 ± 5.1***	0.0145	
^{208}Tl	860.3	***26.4 ± 6.3***	0.0137	
^{228}Ac	911.2	***18.7 ± 0.9***	0.0131	
^{228}Ac	966.8	***22.8 ± 0.4***	0.0126	
^{40}K Series				
^{40}K	1460.8	***244 ± 4***	0.00940	

Table 4.1: The activity concentration results for the Kloof sample number 6 (long measurement) by WA method.

Nuclide	Energies (keV)	Activity Concentration (Bq/kg)	Full-energy peak Absolute efficiency	Weighted Average Activity Concentration (Bq/kg)
^{238}U series				
^{226}Ra/^{238}U	186.1	**282.1 ± 4.7**	0.0451	**263 ± 4**
^{214}Pb	295.1	**252.0 ± 1.2**	0.0318	
^{214}Pb	352.0	**269.1 ± 1.6**	0.0278	
^{214}Bi	934.0	**235.9 ± 7.8**	0.0132	
^{214}Bi	1120.3	**251.9 ± 2.7**	0.0115	
^{214}Bi	1238.1	**255.2 ± 5.8**	0.0107	
^{214}Bi	1377.7	**299.2 ± 6.4**	0.00983	
^{214}Bi	1765.5	**275.2 ± 2.5**	0.00815	
^{214}Bi	2204.1	**282.2 ± 4.9**	0.00687	
^{232}Th series				
^{228}Ac	338.4	**19.1 ± 0.9**	0.0286	**19 ± 1**
^{212}Bi	727.3	**24.0 ± 2.0**	0.0160	
^{228}Ac	794.8	**23.6 ± 2.7**	0.0149	
^{208}Tl	860.3	**16.5 ± 3.4**	0.0141	
^{228}Ac	911.2	**15.3 ± 0.9**	0.0135	
^{228}Ac	966.8	**21.5 ± 1.2**	0.0129	
^{40}K Series				
^{40}K	1460.8	**230 ± 3**	0.00940	

Table 4.2: The activity concentration results for the Westonaria sample number 17A (long measurement) by WA method.

Nuclide	Energies (keV)	Activity Concentration (Bq/kg)	Full-energy peak Absolute efficiency	Weighted Average Activity Concentration (Bq/kg)
^{238}U series				
^{226}Ra/^{238}U	186.1	***6.4 ± 1.3***	0.0558	**5.3 ± 0.3**
^{214}Pb	295.1	***4.0 ± 0.5***	0.0375	
^{214}Pb	352.0	***5.3 ± 0.3***	0.0321	
^{214}Bi	934.0	***6.3 ± 1.0***	0.0138	
^{214}Bi	1120.3	***4.7 ± 2.7***	0.0118	
^{214}Bi	1238.1	***4.3 ± 1.9***	0.0108	
^{214}Bi	1377.7	***4.5 ± 3.2***	0.00989	
^{214}Bi	1765.5	***5.1 ± 1.0***	0.00799	
^{214}Bi	2204.1	***4.2 ± 2.1***	0.00659	
^{232}Th series				
^{228}Ac	338.4	***2.8 ± 0.6***	0.0333	**3.6 ± 0.3**
^{212}Bi	727.3	***5.1 ± 1.5***	0.0172	
^{228}Ac	794.8	***9.2 ± 1.7***	0.0159	
^{208}Tl	860.3	***10.2 ± 2.4***	0.0148	
^{228}Ac	911.2	***4.3 ± 0.4***	0.0141	
^{228}Ac	966.8	***3.7 ± 0.9***	0.0134	
^{40}K Series				
^{40}K	1460.8	**59.3 ± 1.5**	0.00940	

Table 4.3: The activity concentration results for (long measurement) the West Coast sample number 3 by WA method.

Nuclide	Energies (keV)	Activity Concentration (Bq/kg)	Full-energy peak Absolute efficiency	Weighted Average Activity Concentration (Bq/kg)
^{238}U series				
^{226}Ra/^{238}U	186.1	***31.4 ± 2.9***	0.064	**30 ± 1.4**
^{214}Pb	295.1	***29.7 ± 2.0***	0.0417	
^{214}Pb	352.0	***31.3 ± 2.1***	0.0353	
^{214}Bi	934.0	***22.1 ± 6.5***	0.0143	
^{214}Bi	1120.3	***36.9 ± 3.2***	0.0120	
^{214}Bi	1238.1	***27.3 ± 4.9***	0.0110	
^{214}Bi	1377.7	***36.5 ± 5.8***	0.00993	
^{214}Bi	1765.5	***40.5 ± 3.7***	0.00789	
^{214}Bi	2204.1	***45.0 ± 6.4***	0.00641	
^{232}Th series				
^{228}Ac	338.4	***45.0 ± 3.0***	0.0367	**55 ± 4**
^{212}Bi	727.3	***65.8 ± 5.3***	0.0180	
^{228}Ac	794.8	***62.2 ± 5.8***	0.0166	
^{208}Tl	860.3	***59.9 ± 6.4***	0.0154	
^{228}Ac	911.2	***57.5 ± 4.3***	0.0146	
^{228}Ac	966.8	***61.4 ± 4.7***	0.0138	
^{40}K Series				
^{40}K	1460.8	***216 ± 3***	0.00940	

Table 4.4: The activity concentration results for (long measurement) the brick clay sample number 6 by WA method.

Nuclide	Energies (keV)	Activitiy Concentration (Bq/kg)	Full-energy peak Absolute efficiency	Weighted Average Activity Concentration (Bq/kg)
^{238}U series				
^{226}Ra/^{238}U	186.1	**30.4 ± 7.9**	0.0382	**13 ± 1**
^{214}Pb	295.1	**13.4 ± 2.3**	0.0279	
^{214}Pb	352.0	**13.7 ± 1.7**	0.0248	
^{214}Bi	934.0	**19.4 ± 13.5**	0.0128	
^{214}Bi	1120.3	**12.9 ± 2.7**	0.0112	
^{214}Bi	1238.1	**-0.9 ± -7.8**	0.0105	
^{214}Bi	1377.7	**-0.9 ± -11.7**	0.00978	
^{214}Bi	1765.5	**7.3 ± 14.9**	0.00827	
^{214}Bi	2204.1	**12.9 ± 2.7**	0.00710	
^{232}Th series				
^{228}Ac	338.4	**456.6 ± 4.8**	0.0255	**469 ± 8**
^{212}Bi	727.3	**533.8 ± 8.8**	0.0151	
^{228}Ac	794.8	**434.7 ± 12.1**	0.0142	
^{208}Tl	860.3	**507.1 ± 12.5**	0.0135	
^{228}Ac	911.2	**449.0 ± 3.6**	0.0129	
^{228}Ac	966.8	**441.4 ± 4.6**	0.0125	
^{40}K Series				
^{40}K	1460.8	**31±5**	0.00940	

Table 4.5: The activity concentration results for (long measurement) the thorium + stearic acid sample number 5, by WA method.

The activity concentrations and associated uncertainties as derived using short live time measurements are given in Table 4.6 - 4.9.

Nuclide	Energies (keV)	Activity Concentration (Bq/kg)	Full-energy peak Absolute efficiency	Weighted Average Activity Concentration (Bq/kg)
^{238}U series				
^{226}Ra/^{238}U	186.1	**250.8 ± 13.3**	0.0443	**277 ± 5**
^{214}Pb	295.1	**265.5 ± 5.2**	0.0317	
^{214}Pb	352.0	**288.3 ± 4.0**	0.0278	
^{214}Bi	934.0	**271.0 ± 27.8**	0.0137	
^{214}Bi	1120.3	**241.3 ± 8.7**	0.0120	
^{214}Bi	1238.1	**235.1 ± 18.6**	0.0111	
^{214}Bi	1377.7	**293.4 ± 23.5**	0.0103	
^{214}Bi	1765.5	**283.7 ± 4.3**	0.00859	
^{214}Bi	2204.1	**285.4 ± 16.5**	0.00730	
^{232}Th series				
^{228}Ac	338.4	**20.7 ± 4.2**	0.0369	**21 ± 2**
^{212}Bi	727.3	**25.3 ± 8.8**	0.0287	
^{228}Ac	794.8	**7.9 ± 15.9**	0.0164	
^{208}Tl	860.3	**16.2 ± 18.4**	0.0154	
^{228}Ac	911.2	**18.8 ± 2.6**	0.0145	
^{228}Ac	966.8	**26.4 ± 4.9**	0.0139	
^{40}K Series				
^{40}K	1460.8	**244 ± 11**	0.00986	

Table 4.6: The activity concentration results (short measurement) for the Kloof sample number 6 by WA method.

Nuclide	Energies (keV)	Activitiy Concentration (Bq/kg)	Full-energy peak Absolute efficiency	Weighted Average Activity Concentrations (Bq/kg)
^{238}U series				
^{226}Ra/^{238}U	186.1	**263 ± 13**	0.0451	**257 ± 6**
^{214}Pb	295.1	**247 ± 5**	0.0318	
^{214}Pb	352.0	**270 ± 4**	0.0278	
^{214}Bi	934.0	**260 ± 26**	0.0132	
^{214}Bi	1120.3	**222 ± 8**	0.0115	
^{214}Bi	1238.1	**232 ± 16**	0.0107	
^{214}Bi	1377.7	**204 ± 24**	0.00983	
^{214}Bi	1765.5	**268 ± 7**	0.00815	
^{214}Bi	2204.1	**283 ± 15**	0.00687	
^{232}Th series				
^{228}Ac	338.4	***4.8 ± 4.2***	0.0286	**14 ± 2**
^{212}Bi	727.3	***18.4 ± 7.8***	0.0160	
^{228}Ac	794.8	***4.8 ± 15.0***	0.0149	
^{208}Tl	860.3	***15.1 ± 3***	0.0141	
^{228}Ac	911.2	***21.3 ± 5***	0.0135	
^{228}Ac	966.8	***5.0 ± 14***	0.0129	
^{40}K Series				
^{40}K	1460.8	**216 ± 11**	0.00940	

Table 4.7: The activity concentration results for the Westonaria sample number 17A (short measurement) by WA method.

Nuclide	Energies (keV)	Activitiy Concentration (Bq/kg)	Full-energy peak Absolute efficiency	Weighted Average Activity Concentration (Bq/kg)
^{238}U series				
^{226}Ra/^{238}U	186.1	***8.0 ± 2.7***	0.0450	**5.2 ± 0.5**
^{214}Pb	295.1	***4.2 ± 1.0***	0.0317	
^{214}Pb	352.0	***4.7 ± 0.7***	0.0277	
^{214}Bi	934.0	***7.5 ± 6.0***	0.0132	
^{214}Bi	1120.3	***5.6 ± 1.4***	0.0115	
^{214}Bi	1238.1	***-0.4 ± -6.2***	0.0107	
^{214}Bi	1377.7	***-0.4 ± -6.9***	0.00982	
^{214}Bi	1765.5	***6.7 ± 1.1***	0.00814	
^{214}Bi	2204.1	***1.1 ± 5.1***	0.00688	
^{232}Th series				
^{228}Ac	338.4	***4.2 ± 1.0***	0.0286	**4.6 ± 0.5**
^{212}Bi	727.3	***4.4 ± 2.0***	0.0160	
^{228}Ac	794.8	***1.5 ± 4.8***	0.0149	
^{208}Tl	860.3	***4.9 ± 4.8***	0.0140	
^{228}Ac	911.2	***4.6 ± 0.8***	0.0134	
^{228}Ac	966.8	***5.6 ± 1.3***	0.0129	
^{40}K Series				
^{40}K	1460.8	**54 ± 4**	0.00940	

Table 4.8: The activity concentration results for the West Coast sample number 3 (short measurement) by WA method.

Nuclide	Energies (keV)	Activitiy Concentration (Bq/kg)	Full-energy peak Absolute efficiency	Weighted Average Activity Concentration (Bq/kg)
^{238}U series				
^{226}Ra/^{238}U	186.1	***32.9 ± 6.5***	0.0532	**32 ± 2**
^{214}Pb	295.1	***32.0 ± 2.3***	0.0365	
^{214}Pb	352.0	***34.0 ± 1.7***	0.0318	
^{214}Bi	934.0	***28.8 ± 15.9***	0.0142	
^{214}Bi	1120.3	***21.4 ± 3.0***	0.0123	
^{214}Bi	1238.1	***42.3 ± 9.7***	0.0113	
^{214}Bi	1377.7	***59.0 ± 3.5***	0.0103	
^{214}Bi	1765.5	***37.8 ± 4.0***	0.00845	
^{214}Bi	2204.1	***19.9 ± 14.4***	0.00704	
^{232}Th series				
^{228}Ac	338.4	***41.6 ± 3.2***	0.0326	**55 ± 3**
^{212}Bi	727.3	***61.8 ± 7.0***	0.0174	
^{228}Ac	794.8	***31.8 ± 5.8***	0.0162	
^{208}Tl	860.3	***46.9 ± 11.8***	0.0152	
^{228}Ac	911.2	***58.3 ± 1.4***	0.0145	
^{228}Ac	966.8	***58.5 ± 3.0***	0.0138	
^{40}K Series				
^{40}K	1460.8	***220 ± 9***	0.00986	

Table 4.9: The activity concentration results for the brick clay sample number 6 (short measurement) by WA method.

4.2 FSA results

The FSA results were obtained using a low-energy cut-off of 300 keV for long measurements and 400 keV for short measurements (see also Figure 3.19). The fits on which results are based are shown in Figures 3.20 to 3.32. The derived activity concentrations from long and short measurement are given in Tables 4.10 to 4.11 respectively.

Sample description		**Activity Concentration in (Bq/kg) (for long measurement) with a cut off energy of 300 keV**			
S #	**Type of Sample**	**Full Spectrum Analysis (FSA)**			
		^{40}K	^{238}U	^{232}Th	χ^2/ν
D3	West Coast sand	61 ± 3	4.0 ± 0.1	2.2 ± 0.3	1.6
17A	Westonaria sand	227 ± 4	232 ± 1	18 ± 0.2	3.5
6B	Kloof mine sand	242 ± 4	272 ± 1	19.4 ± 0.2	2.3
D6	Brick clay	222 ± 5	28.8 ± 0.4	54.2 ± 0.5	1.9
5	thorium+stearic acid	1 ± 4	0.8 ± 0.5	395.4 ± 0.3	19.6

Table 4.10: The FSA results (long measurement), uncertainties and the associated chi-square per degree of freedom obtained using cut-off energy of 300 keV for the samples indicated.

Sample description		Activity Concentration in (Bq/kg) (for short measurements) with cut off energy of 400 keV			
S #	Type of Sample	Full Spectrum Analysis (FSA)			
		^{40}K	^{238}U	^{232}Th	χ^2/ν
D3	West Coast sand	35.6± 3.3	0.7± 0.3	3.3± 0.3	1.9
17A	Westonaria sand	250 ± 10	241 ± 2	21± 1	2.2
6B	Kloof mine Sand	240 ± 9	237± 2	20± 1	1.8
D6	Brick clay	220 ± 7	31 ± 1	59± 1	1.4

Table 4.11: The FSA results (short measurements), uncertainties and the associated chi-square per degree of freedom obtained using a cut off energy of 400 keV for the samples indicated

4.3 Comparison of WA and FSA results

The weighted average WA results and FSA results are tabulated and juxtaposed in Tables 4.13 and 4.14 for long and short measurements, respectively. A comparison of the results is shown graphically in Figures 4.1 to 4.12.

iThemba LABS ERL Soil Measurements		**Activity Concentration in (Bq/kg) for long measurements with cut-off energy of 300 keV**						
Ref no.	Sample Type	Window's Analysis (WA)			Full Spectrum Analysis (FSA)			χ^2_{red}
		^{40}K	^{238}U	^{232}Th	^{40}K	^{238}U	^{232}Th	
D3	West Coast sand	59.3 ± 1.5	5.3 ± 0.3	3.6 ± 0.3	61 ± 3	4.0 ± 0.1	2.2 ± 0.3	1.6
17A	Westonaria sand	230 ± 3	263 ± 4	19 ± 1	227 ± 4	232 ± 1	18 ± 0.2	3.5
6B	Kloof mine sand	244 ± 4	320 ± 5	21± 1	242 ± 4	272 ± 1	19.4 ± 0.2	2.3
D6	Brick clay	216 ± 3	30 ± 1.4	55 ± 4	222 ± 5	28.8 ± 0.4	54.2 ± 0.5	1.9

Table 4.12: The activity concentrations from the two methods of analysis for long measurement.

iThemba LABS ERL Soil Measurements		**Activity Concentration in (Bq/kg) for short measurements at the cut-off energy 400 keV**						
Ref no.	Sample Type	Window Analysis (WA)			Full Spectrum Analysis (FSA)			χ^2_{red}
		^{40}K	^{238}U	^{232}Th	^{40}K	^{238}U	^{232}Th	
D3	West Coast Sand	54 ± 4	5.2 ± 0.5	4.6 ± 0.5	35.6± 3.3	0.7± 0.3	3.3± 0.3	1.9
17A	Westonaria Sand	216 ± 11	257 ± 6	14 ± 2	250 ± 10	241 ± 2	21± 1	2.2
6B	Kloof mine Sand	244 ± 11	277 ± 5	21 ± 2	240 ± 9	237± 2	20± 1	1.8
D6	Brick clay	220 ± 9	32 ± 2	55 ± 3	220 ± 7	31 ± 1	59± 1	1.4

Table 4.13: The activity concentrations from the two methods of analysis for short measurements.

The long measurement results of these two methods (WA and FSA) were plotted on the histograms to show the variations in activity concentrations for various samples. The percent uncertainties were also shown see Figures 4.1 to 4.12. The notations WAL, WAS, FSAL, and FSAS are defined as follows:

WAL = Window Analysis Long, (for long measurement),

WAS = Window Analysis Short (for short measurement),

FSAS = Full Spectrum Analysis (for short measurement),

FSAL = Full Spectrum Analysis (for long measurement).

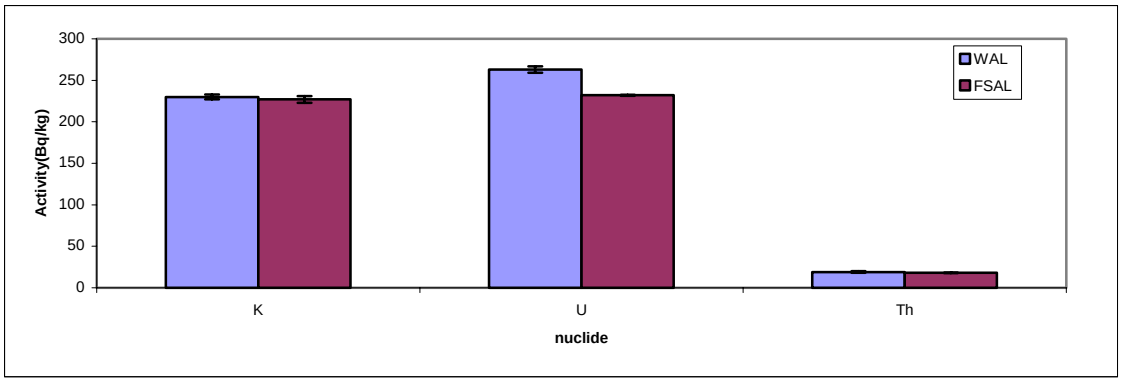

Figure 4.1: The comparison of the three nuclides for Westonaria sand (long measurement) in both window and FSA analyses.

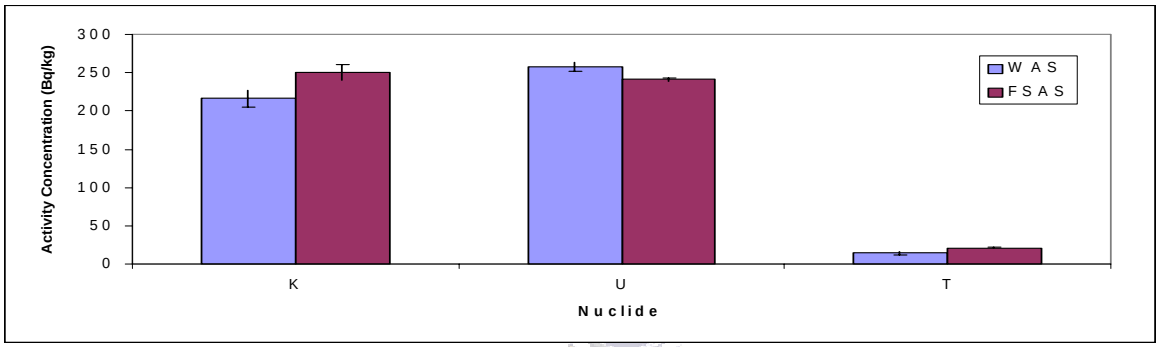

Figure 4.2: The comparison of the three nuclides for Westonaria sand (short measurement) in both window and FSA analyses.

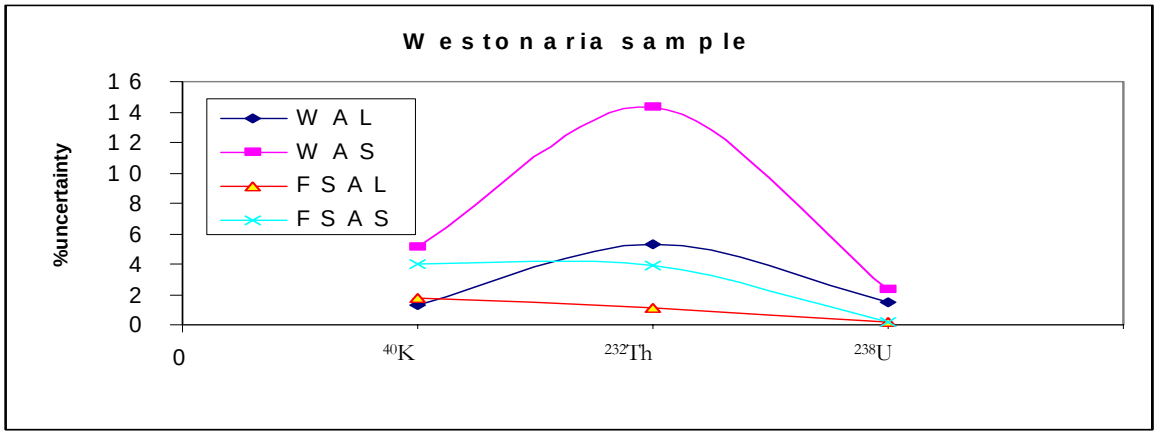

Figure 4.3: The percentage uncertainties for activity concentrations as a function of nuclide for Westonaria sand sample.

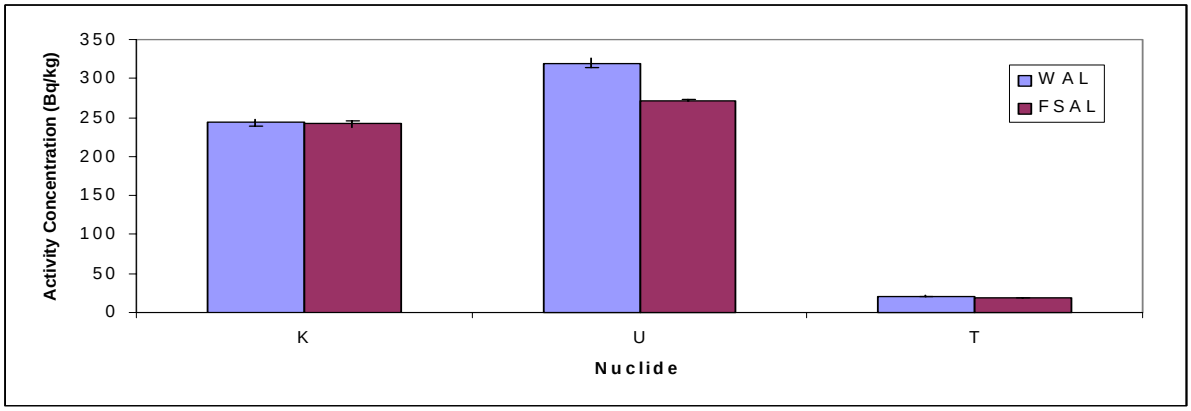

Figure 4.4: The comparison of the three nuclides for Kloof sand (long measurement) in both window and FSA analyses.

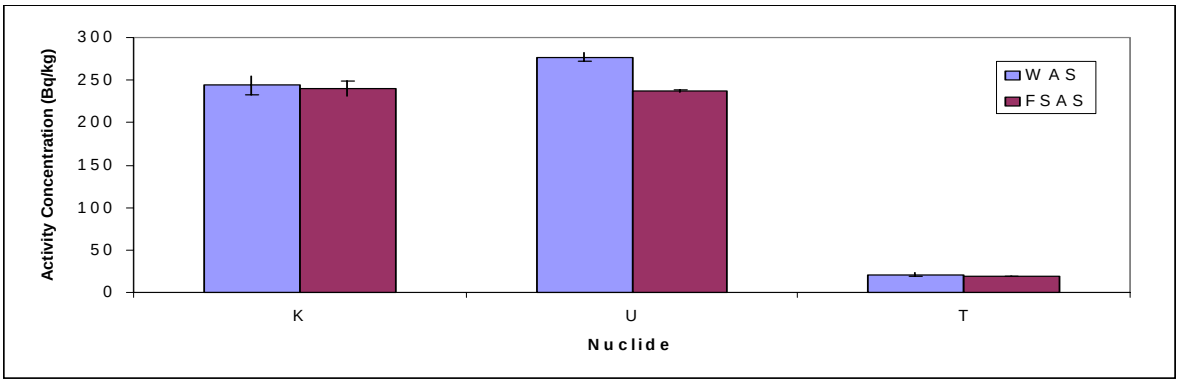

Figure 4.5: The comparison of the three nuclides for Kloof sand (short measurement) in both window and FSA analyses

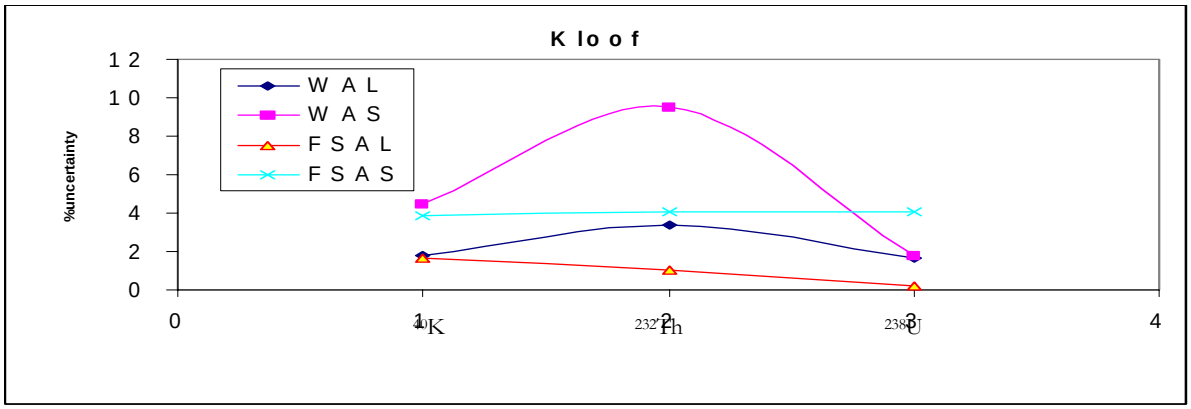

Figure 4.6 : The percentage uncertainties for activity concentrations as a function of nuclide for Kloof sand sample.

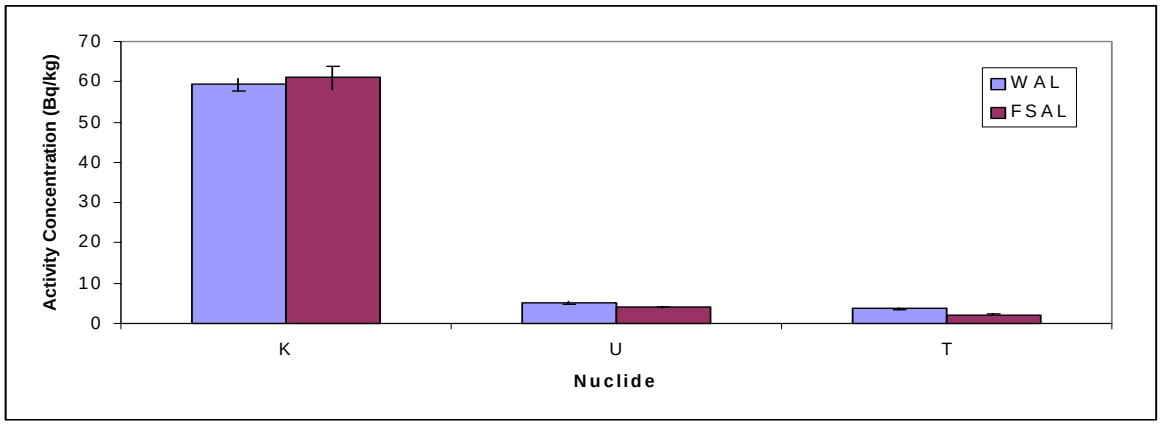

Figure 4.7: The comparison of the three nuclides for west coast (long measurement) in both window and FSA analyses.

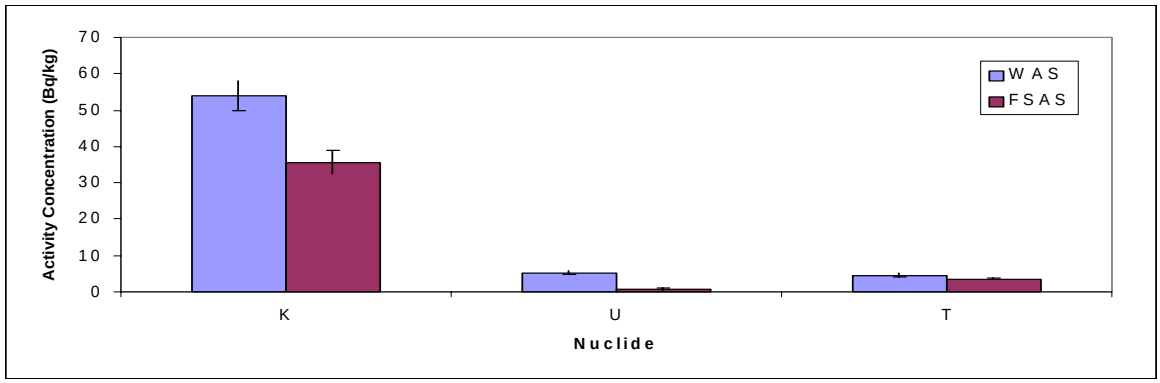

Figure 4.8: The comparison of the three nuclides for West coast (short measurement) in both window and FSA analyses.

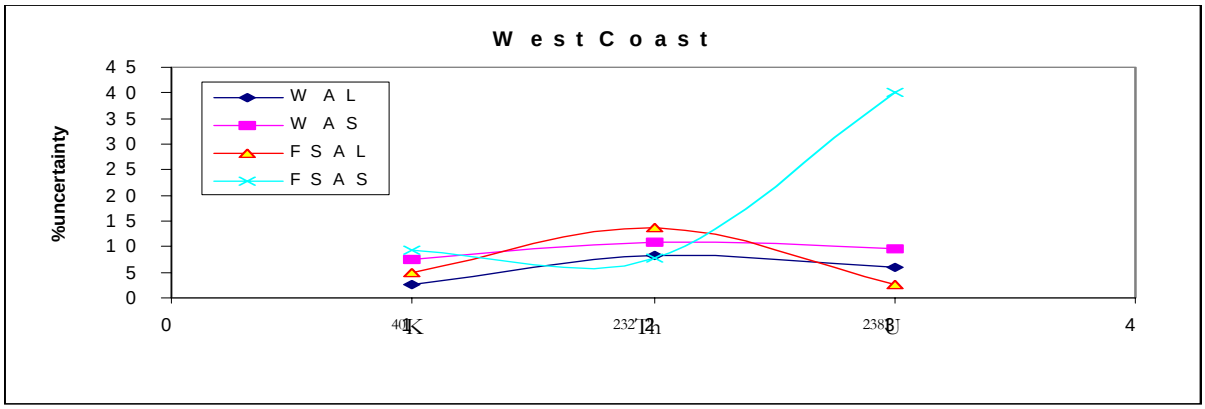

Figure 4.9: The percentage uncertainties for activity concentrations as a function of nuclide for West Coast sand sample.

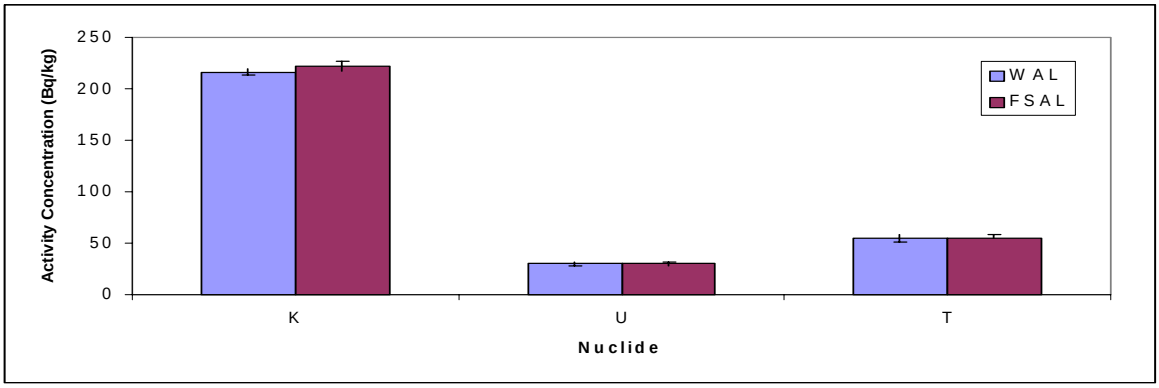

Figure 4.10: The comparison of the three nuclides for brick clay for long measurement in both window and FSA analyses

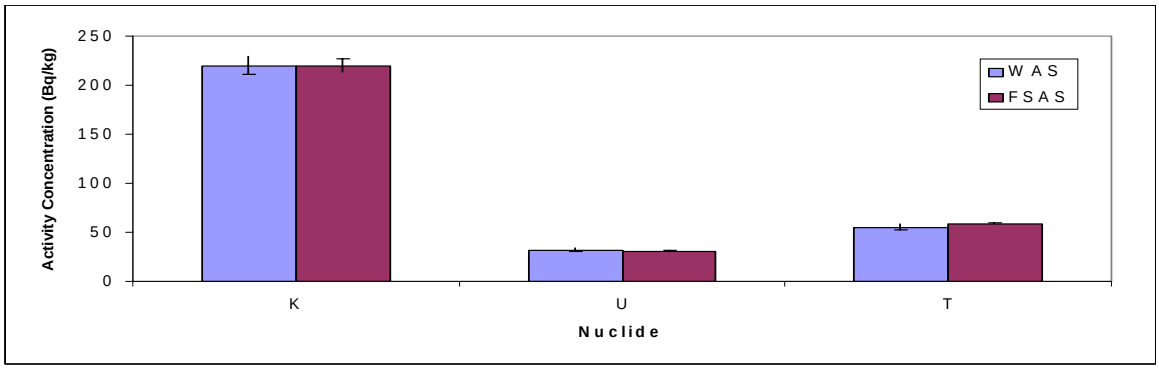

Figure 4.11: The comparison of the three nuclides for brick clay for short measurement in both window and FSA analyses

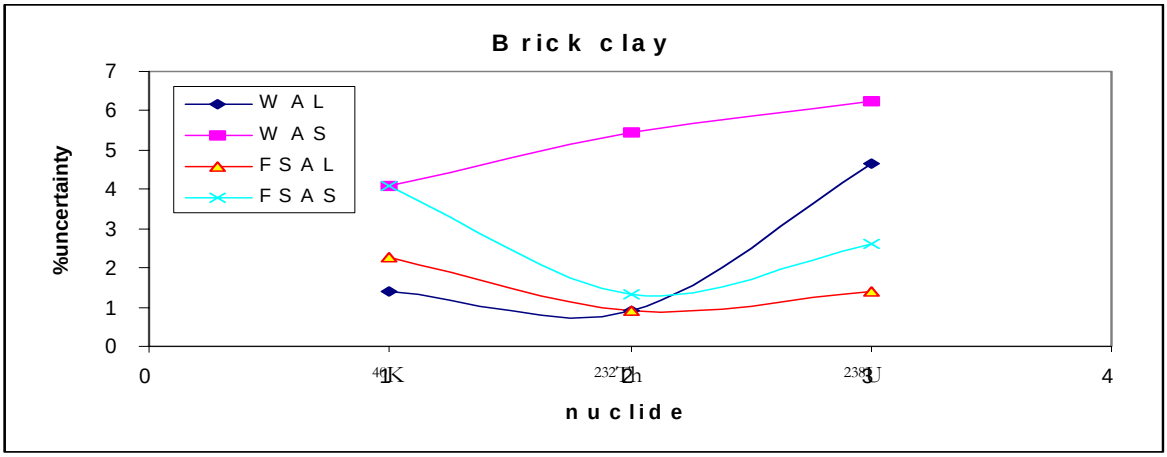

Figure 4.12: The percentage uncertainties for activity concentrations as a function of nuclide for brick clay sample.

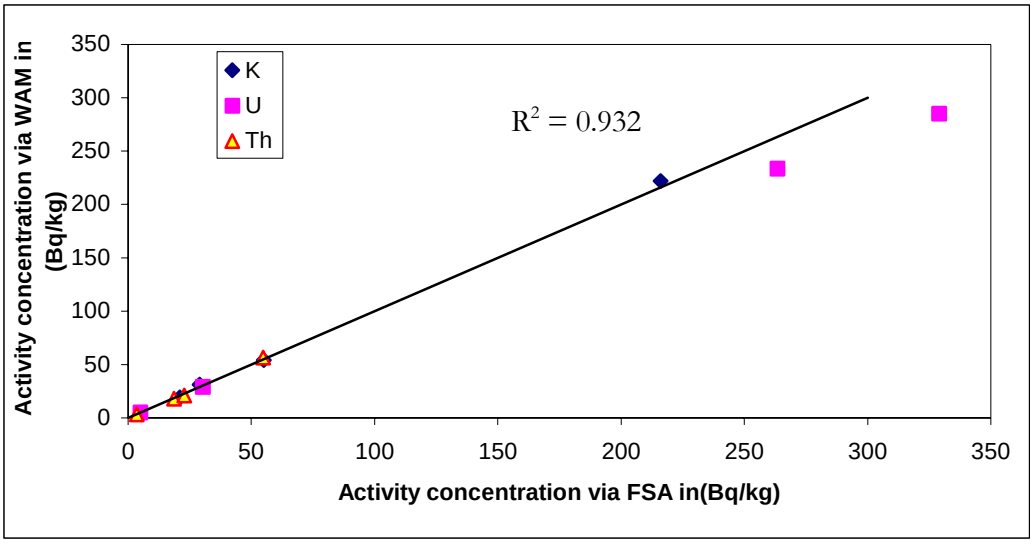

Figure 4.13: A graph showing correlation of activity concentration determined using the WAM vs FSA, on average the two methods agree well within the correlation coefficient of 0.932 as depicted on Figure.

The deviation between results from the two methods for ^{238}U concentrations (long measurements) was found to be about 18% for the Kloof, 13% for Westonaria, 4% for brick clay and 25% for West coast sand (see Figure 4.14). The deviations between results from long measurement for ^{232}Th yielded 6% for Kloof sample, 5% for Westonaria sample, 1% Brick clay; and 63% for West coast sand (see Appendix E for the ratios presented). The deviations are consistently higher by these percentages for WA than FSA. This trend has to do with the fact that the uranium and thorium sources (used for FSA method) did not fill 1 litre Marinelli beaker. This could be attributed to the self-absorption effects, which vary as a function of volume. The evidence of this is presented later in section 4.5. An attempt to study the volume and density effects was made through the use of the Sima model [Sim92] and the results from this modelling are presented in section 4.5 (see also appendix D).

The low activity West coast sample resulted in very high uncertainty in ^{238}U activity concentrations (see Figure 4.9 and 4.15). This was especially true for the FSA method, which has proved to find it difficult to determine the activity concentrations of low activity nuclides. This is because of the contribution of the background counts, which at times are higher than net counts, especially in short measurements, thus yielding a poor fit.

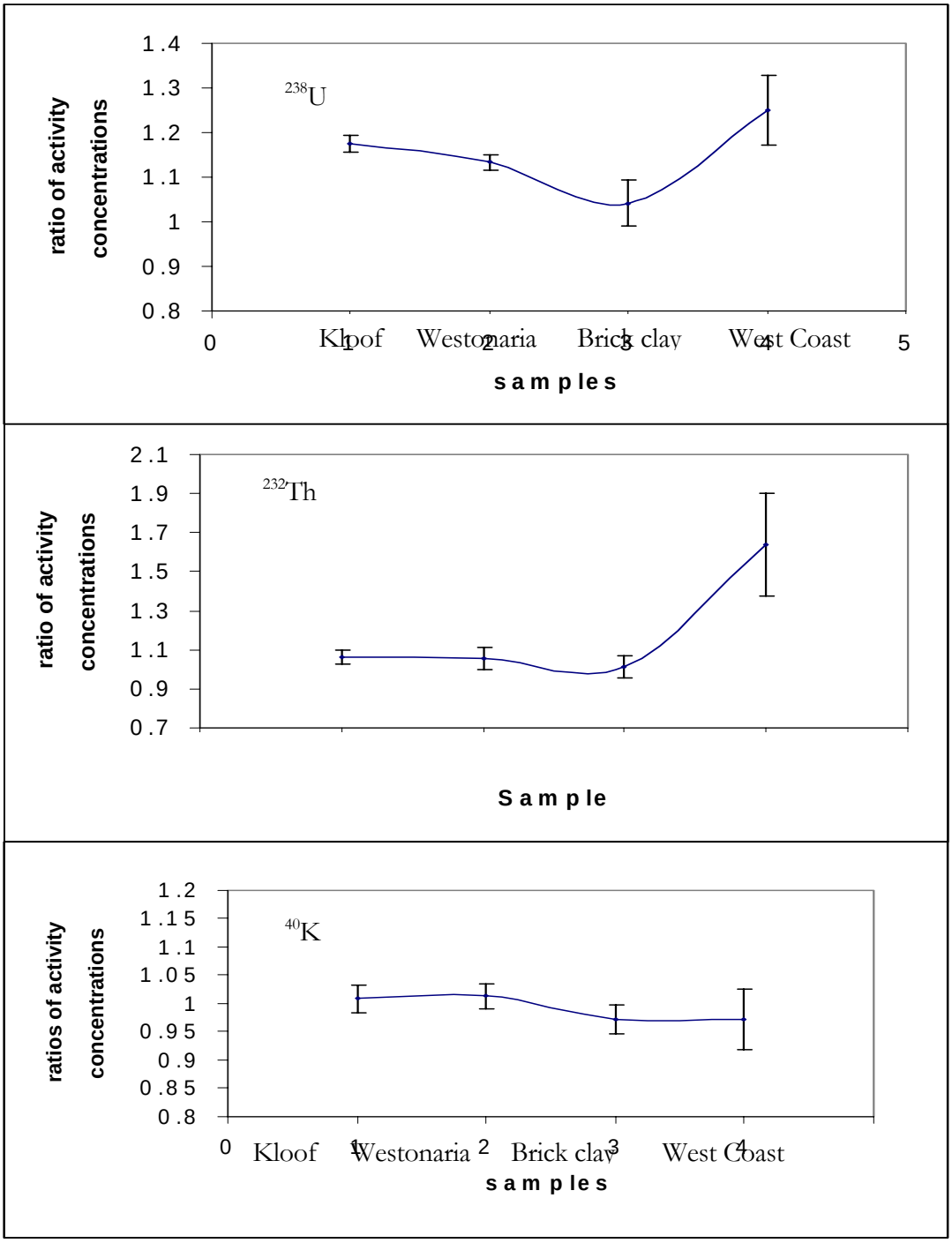

Figure 4.14: The activity concentration ratios (WA/FSA) of uranium, thorium and potassium ***long measurement*** *for various samples.*

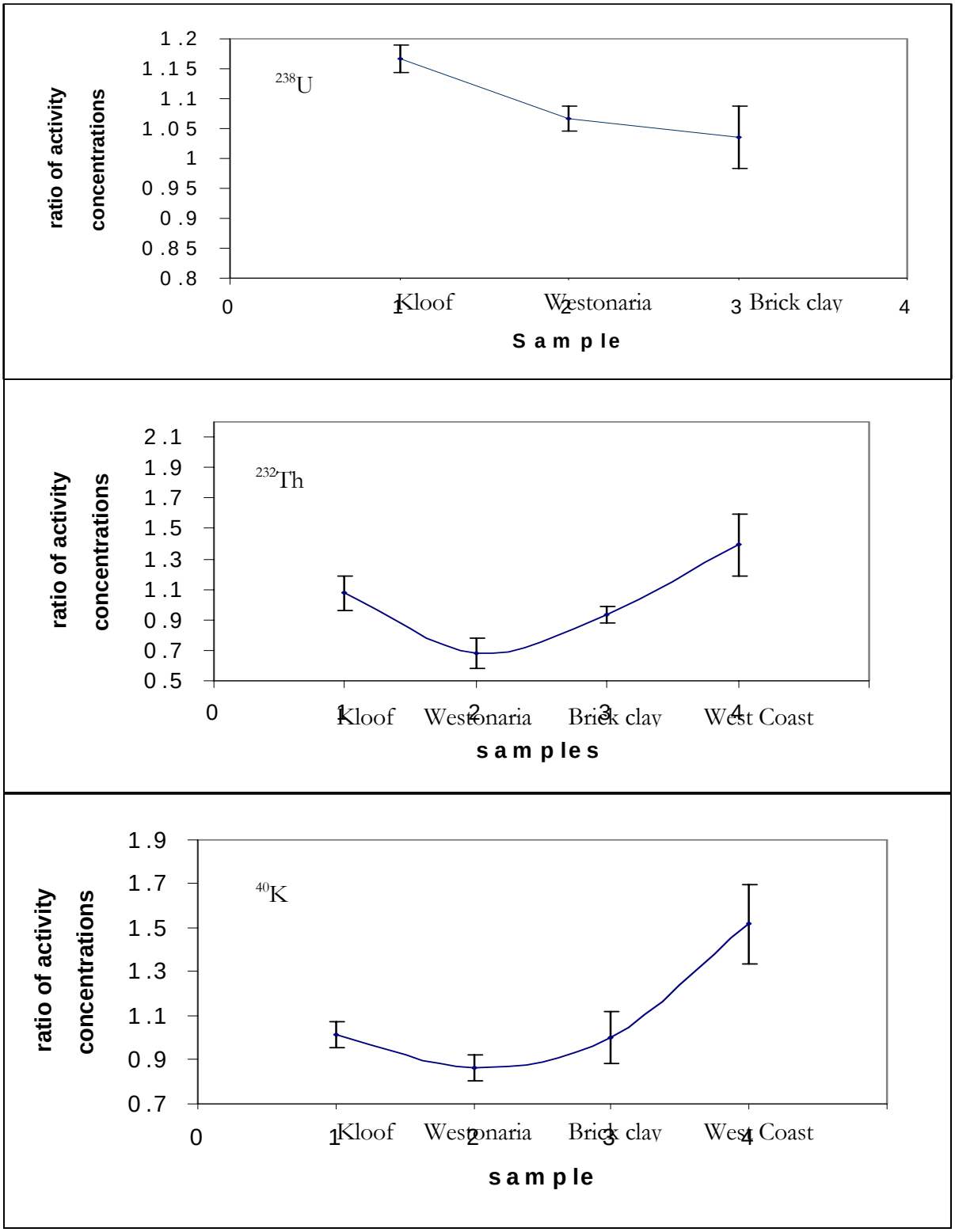

Figure 4.15: The activity concentration ratios (WA/FSA) of uranium, thorium and potassium from ***short measurements*** *for various samples. The ratio for the ^{238}U (West coast sample) is not shown.*

Method	Advantages	Disadvantages	Significant source of uncertainty
WA	No correction for self-absorption effects needed and one standard source required (i.e. KCl)	Some lines prone to summing effects	Short time measurements
FSA	Short Measurements and No worry about Summing effects	Three standard sources required	Some resolution may be lost during the rebinning of the spectrum

Table 4.14: Advantages and disadvantages for the two methods including the best measurement times required for the activity concentration determination.

For samples where ^{40}K and ^{232}Th have the same activity concentration, the ^{40}K line is ten times stronger than the ^{232}Th line [Dem97]. In case the ^{232}Th content is several orders of magnitude larger, it becomes virtually impossible to determine the ^{40}K content accurately, since the peaks are very close to each other.

The results of the high thorium content are tabulated in Table 4.15, for the evidence of that. For the FSA this summing effect is not a problem, since all the peaks are considered for the determination of the content of these two nuclides, that is the ^{40}K and ^{232}Th. In the WA the 1460.8 keV peak is confused with the 1459.2 keV one.

Nuclide	FSA activity concentrations (Bq/kg)	WA activity concentrations (Bq/kg)
^{40}K	1 ± 4	31 ± 5
^{238}U	0.8 ± 0.5	12 ± 1
^{232}Th	395.4 ± 0.3	469 ± 8

Table 4.15: The results of sample 5, a high thorium content sample.

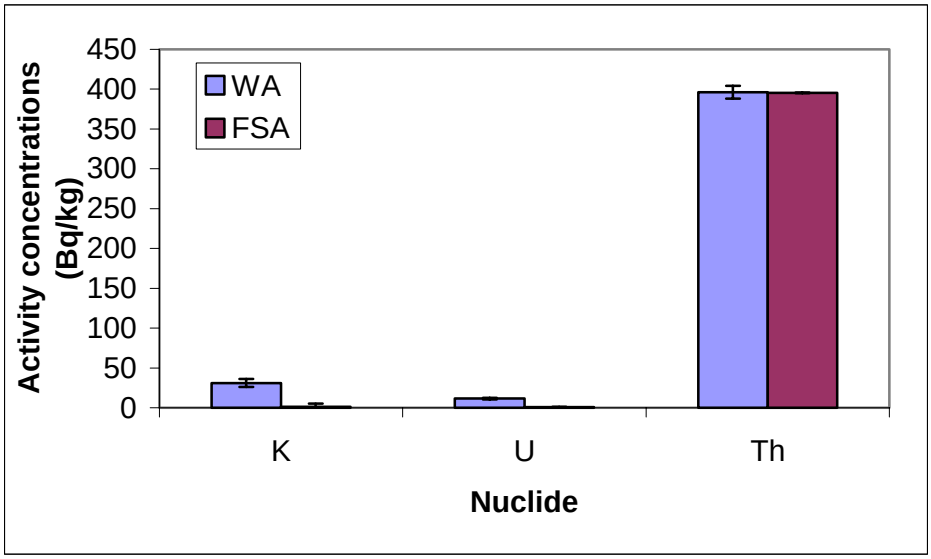

Figure 4.16: Activity concentration of nuclides for the high thorium content sample.

- **Thorium sample**

As discussed in chapter 2 the thorium + stearic sample was made up using stearic acid and IAEA reference material (RGTh-1) having an activity concentration of 3250 Bq/kg (see Table 2.4). The sample was prepared in such a way that the activity concentration of ^{232}Th in the sample was 500.0 ± 0.5 Bq/kg [Jos04].

The WA and FSA results for this sample allow us to compare WA and FSA derived ^{232}Th concentrations, with what is expected. As can be seen in Table 4.15, the WA yields a result of 469 Bq/kg, which is 9% smaller than expected. The FSA gives the result of 395 Bq/kg, which is 21% smaller than expected. It is clear from Figure 3.31 that the counts in FSA fit spectrum are generally higher than in the measured spectrum in regions outside photo peaks. This happens since the full-energy peak efficiency (also termed the photopeak efficiency) is higher in the case of thorium sample, since it has such a low density (~0.7 g/cm^3) resulting in a higher peak to total ratio (i.e. relatively more counts inside than outside the photopeak). Since the FSA procedure involves the minimisation of reduced chi-square, the photopeaks are fitted preferentially since a misfit in the region of a photopeak contributes significantly to reduced chi-square.

4.4 Discussion of WA Results

Counting uncertainties in environmental measurements are usually high such that coincident summing corrections might be neglected [Gar01]. But the lines that are prone to coincident-summing[6] such as the 609 keV were still avoided for purpose of reducing the systematic error. At present the ERL at iThemba LABS has a study going on about the prominent lines that are prone to the coincidence-summing problem. Other lines that are prone to the coincident-

[6] This is when γ-rays are emitted in cascades from a nucleus and thus detected as one peak

summing like the 911.2 keV, 969.0 keV from ^{228}Ac and 727.3 keV due to ^{212}Bi might in future be omitted [Gar01].

Accumulation of good statistics is required for the reliability of this method. This was demonstrated by comparing the uncertainties associated with measurements of varying duration. Results from shorter measurements were more uncertain than those from long ones (see Figures 4.3,4.6,4.9 and 4.12).

4.5 Discussion of FSA Results

Contrary to WA, which only uses the data in a number of peaks for analysis, FSA includes all the spectral information in the data analysis. The increased amount of information will decrease the statistical uncertainties in the method, thus giving this method an advantage.

A practical problem of the FSA method might be the fact that small gain drifts may occur, resulting in the slight shifts and broadening of peaks.

The results for this method are given for the cut-off energy of 300 keV for the long measurement and for shorter measurement a lower cut-off energy of 400 keV and higher cut-off energy of 1600 keV were used to exclude high energy background counts.

This particular cut-off energy was chosen because of the poor fit, as observed for low energies (see Figures 3.20 and 3.21). This is reflected by the high values of χ^2/ν. Figure 3.20 shows an under-estimation of the measured spectrum with a chi-square 2.5 at the cut-off energy of 300 keV for a typical spectrum of Kloof sample #6. This under prediction at lower energies is attributed to the self-absorption effects.

From Table 2.4 it is clear that the Marinelli beakers fillings were not the same in volume; therefore this has a consequence on the measurement result due to these volume effects, which are related to self-absorption effects. Figures 4.17, 4.18 are the results showing the transmission factors from the Sima calculations for various samples with different densities as

discussed in Appendix D, while Figure 4.19 illustrates the volume effects for the uranium source. Debertin and Ren did a similar study [Deb89].

The poor reproduction of the FSA at energies less than 300 keV led to the studying of self-absorption effects based on the Sima model.

Self-absorption is the removal of γ-ray by material in the sample itself. The effect increases for lower energies (< 300 keV) and with the atomic number of an element [Dem97].

Figures 4.17 and 4.18 show the results of the effect of density on the transmission factors (see Appendix D for discussion on this), while Figure 4.19 shows the volume effect on the transmission factors.

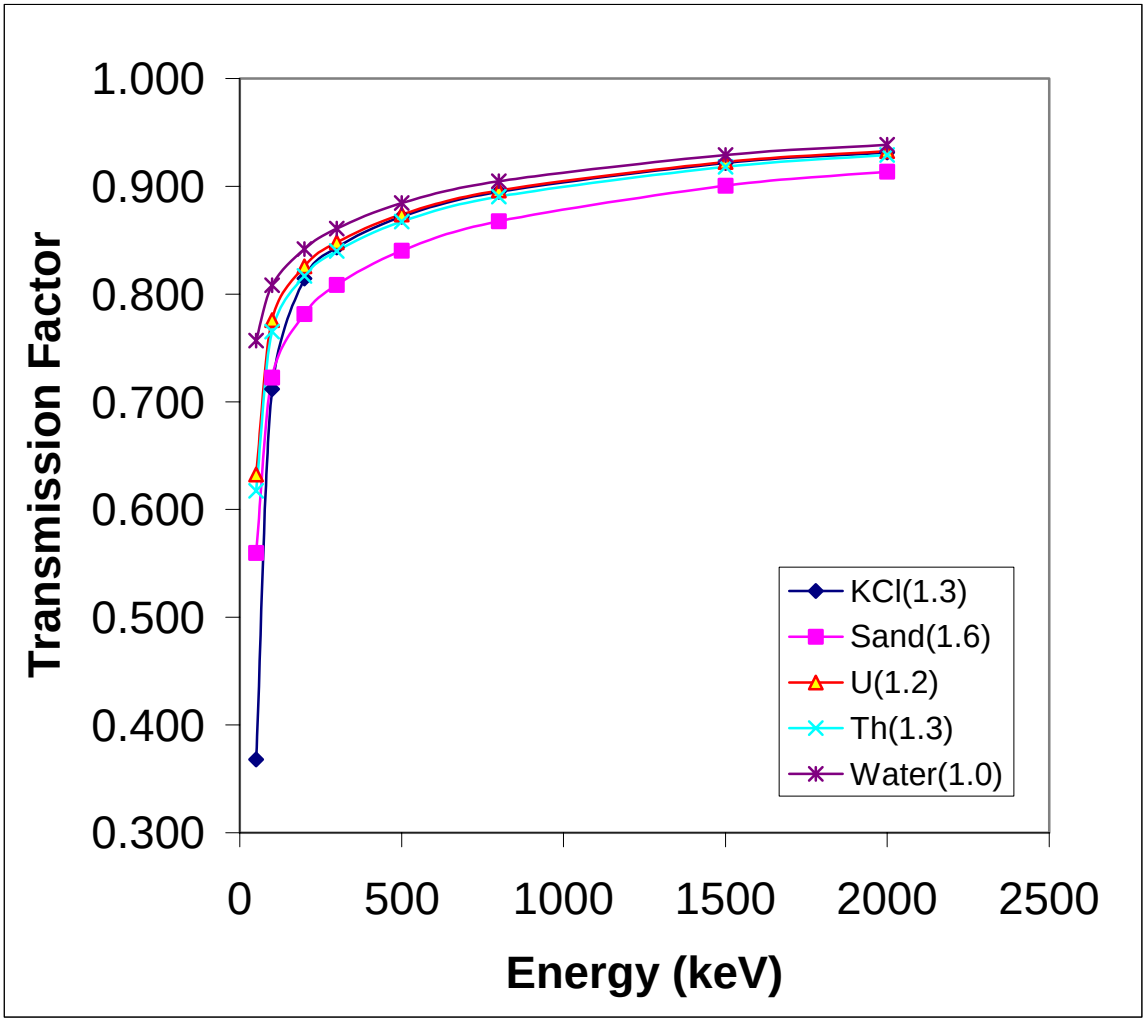

Figure 4.17: Calculated transmission factors for different densities for a 1000 cm^3 Marinelli as a function of γ-ray energy, the legends shows the three reference sources, which are Potassium Chloride (KCl), uranium, and thorium together with water and sand at various densities (densities are shown by the numbers in brackets in the legends).

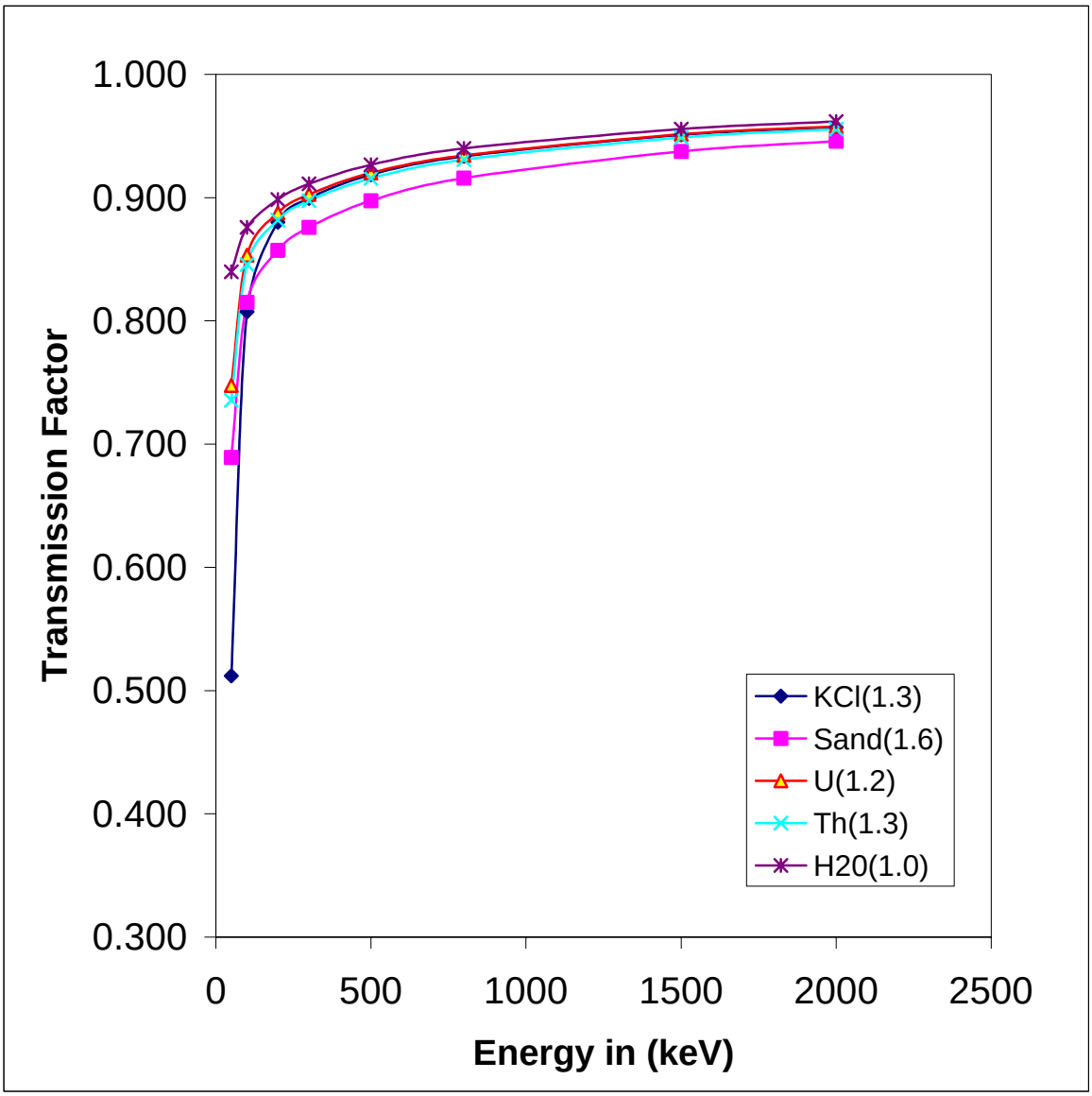

Figure 4.18: The transmission factor for a 500 cm^3 Marinelli at different densities as a function of γ-ray energy.

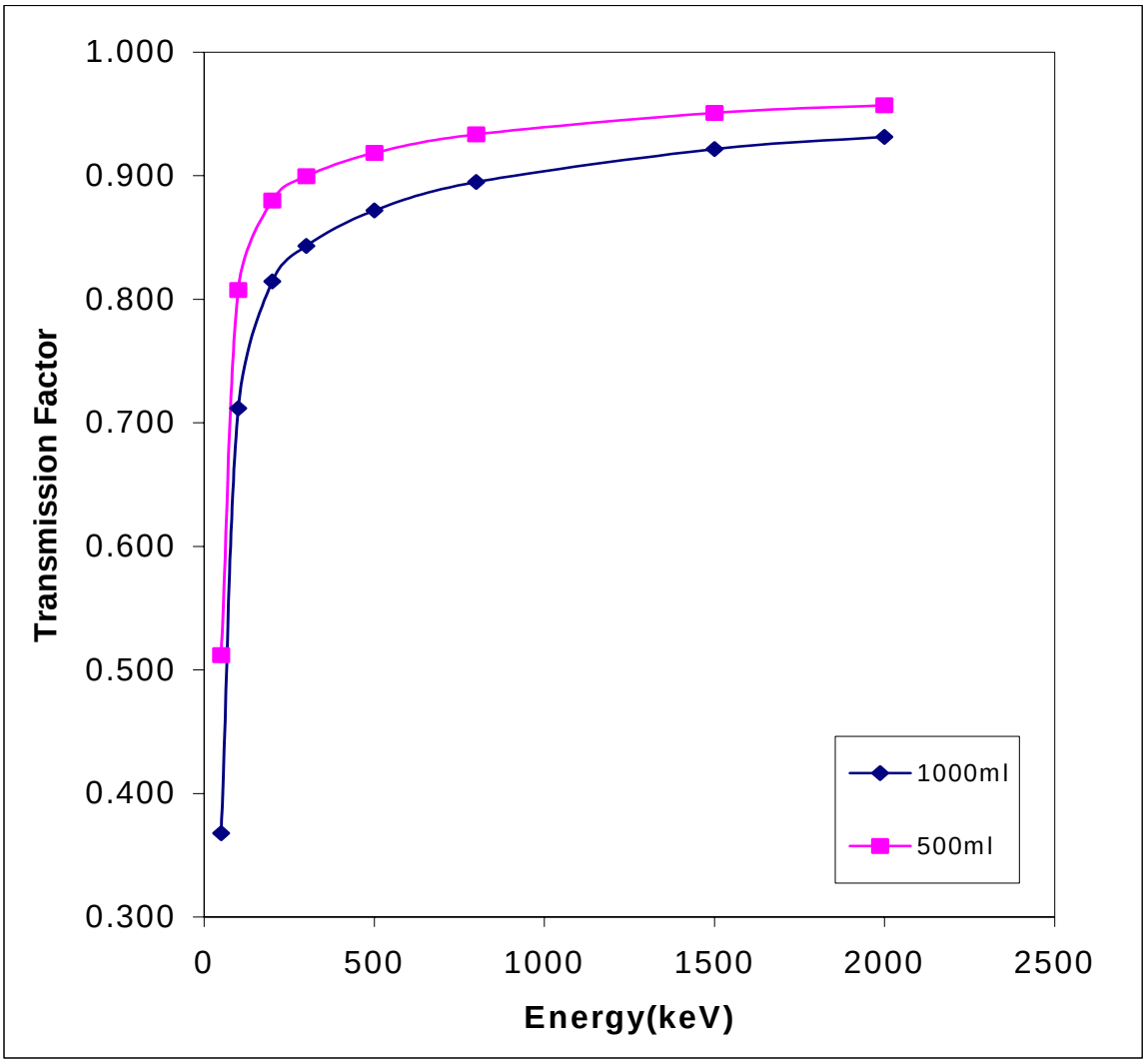

Figure 4.19: The volume effect on the transmission factor for different fillings (with sand of density 1.6 g/cm^3) of Marinelli as a function of γ-ray energy.

During the determination of the detection efficiency an error may occur due to the difference in the densities of the standard source and the sample. This effect can be verified from the Figure 4.17. In this Figure it is clear that at lower energies samples with high densities such as that of sand at 1.6 g/cm^3 get attenuated even more, while the less dense samples such as water at a density of 1 g/cm^3 get attenuated even less. This trend is strong at energies less than 300 keV, and at higher energies is almost negligible. The other difference is due to the atomic number; this difference can be witnessed by the KCl, which gets attenuated more at lower energies than sand even if its density is less than that of sand. This is simply because KCl has an effective atomic number Z greater than that of SiO_2 which is a major constituent of sand.

Most of the photon attenuation occurs at low energy with Marinelli beaker filled to its full capacity, while at lower volumes there is less attenuation, this is because it takes photons far away from the detector even more time to arrive at the detection point and hence they get attenuated on their path, see Figure D.1 (Appendix D) for the variations in the filling of the beaker.

The under prediction of the fit at the continuum for the FSA method of analysis is attributed to this concept, especially because the source volumes were ± 400ml, for thorium and uranium; while samples had volumes close to 100 ml, see Tables 2.3 and 2.4 for details.

Different filling heights of the Marinelli beaker yield different effective thickness, which were used to calculate the transmission factors as in the Figure D.1 (see also Table D.1 in Appendix D). The percentage difference according to these volume differences was calculated for full (1000 ml) and half-full (500 ml) Marinelli beaker. These percentage differences are plotted in Figure 4.20.

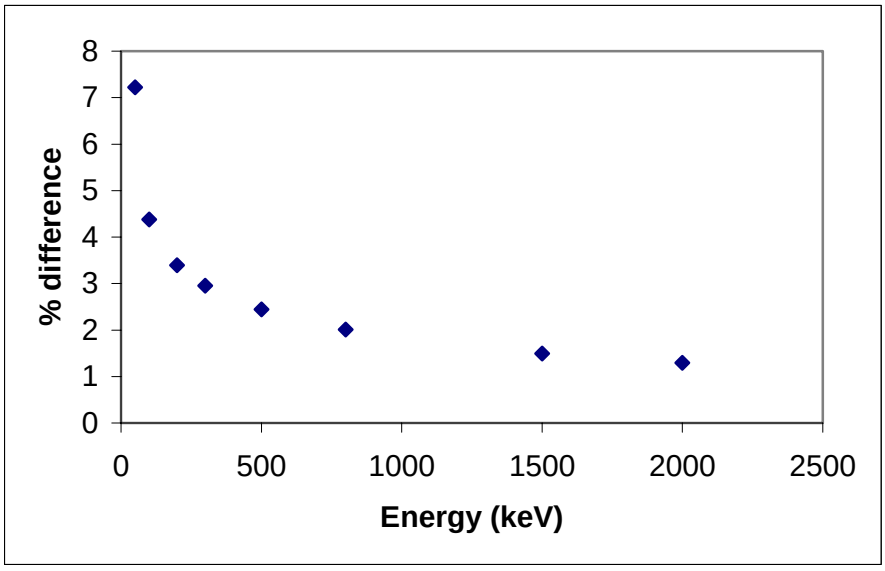

Figure 4.20: The differences in the transmission factors of (Westonaria sand) with regard to full and half full Marinelli beaker as a fuction of energy.

On interpolation the percent difference due to volume for the 1460.8 keV line was found to be about 1.5 %. The percent difference %D was calculated as follows:

$$\%D = \frac{T_{full} - T_{half}}{T_{full}} \times 100 \qquad (4.1)$$

where T_{full} and T_{half} are transmission factors for a full and half-full Marinelli beakers respectively. These self-absorption effects are of major concern; this can be seen in Figure 3.19 for energies below 300 keV; therefore another approach of defining these effects will be to describe the probabilities of the interaction of γ-ray with matter inside both the detector and Marinelli beaker. This will be done by following a γ-ray photon of a particular energy inside the Marinelli beaker until the detector absorbs it. Two possibilities were taken into consideration, in particular photoelectric absorption and Compton scattering.

Consider the Figure 4.21

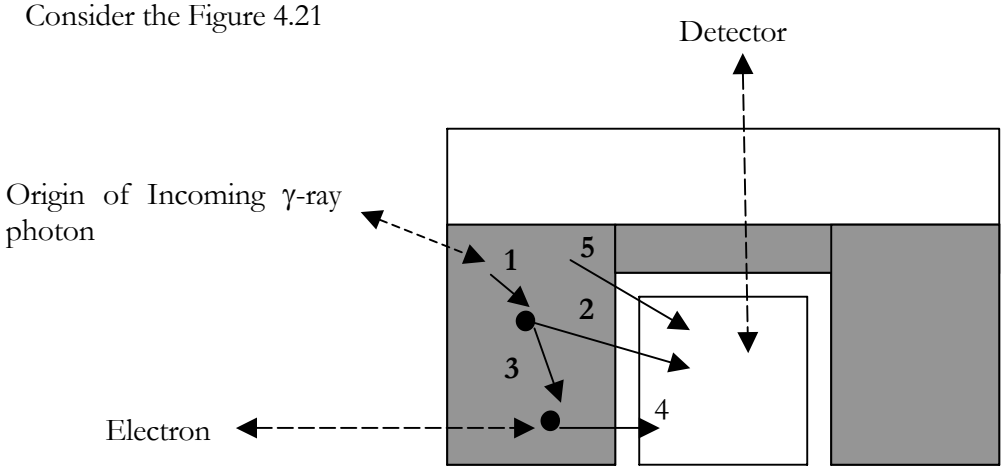

Figure 4.21: A filled Marinelli beaker showing an incoming photon and possibilities of interaction in both the beaker and detector.

The incoming γ-ray of a particular energy interacts with an electron of the sample in the Marinelli beaker and there are several possibilities by which it can interact. These are photoelectric absorption (1), and Compton scattering (2) and another Compton scattering (3). The scattering photon could get deviated again leading to photoelectric absorption in the detector as in (4). Process (3) is more dominant when the sample is denser, while process (2) is most likely when the sample is less dense. The incoming γ-ray photon in (4) will lose some energy proportional to the density of the sample and thus contributing more to low energy photons at the Compton continuum. This explains the reason why the fit at the region from 50 keV to 300 keV is underestimated at the continuum, for sample of higher density such as in Figure 3.20 (a). Process (4) explains the overestimation of the lower density sample in Figure 3.20 (b). Another process is direct photoelectric absorption (5) on a crystal.

CHAPTER 5

Conclusion

This chapter reviews the results of this study and future work on the study is suggested.

5.1 Outlook

This study introduced a novel technique, that is the FSA method of analysis to the analysis of soil spectra using HPGe detector in the ERL at iThemba LABS to complement the conventional Window Analysis method.

Although a correlation was obtained between these two methods of analysis, the interpretation of the results was found to be difficult since the volume of reference ^{238}U and ^{232}Th material used to obtain standard spectra were only 400 ml, whereas the samples to be measured were all close to the full capacity of Marinelli beakers (volume ~ 900 ml). This resulted in the different self-absorption effects during the measurement of standard spectra than during the measurement of sample spectra.

Furthermore, the difference in volume also leads to the different efficiencies caused by the change in the geometry. For a full Marinelli beaker the average distance from the sample to the detector is larger than in the 400 ml case. In order to avoid the systematic error associated with this volume effect, it is recommended new standard spectra be obtained by measuring Marinelli beakers filled with reference ^{238}U and ^{232}Th material to obtain constant geometry. In order to accomplish this, additional reference material will have to be purchased. After these new standard spectra are obtained the only significant remaining effects that need to be considered is that associated with density and the effective charge of the material.

The model of Sima et al. [Sim92] used to calculate the self-absorptions in Marinelli beakers was found to under-predict the volume effect observed in this work. There is therefore scope to improve this model. An alternative to this is to use a Monte Carlo simulation approach.

The FSA method has shown some difficulty in determining activity concentrations of low activity samples; especially if the background counts are higher than the net counts. From Figures 4.3, 4.6, 4.9 and 4.12 in Chapter 4, it is clear that measuring times have to be increased for WA and FSA short measurements in order to obtain good counting statistics with these methods. The uncertainties increase with a decrease in activity concentrations, and this is due to the contribution of the background counts. This can be witnessed in the results of low activity samples, such as the West coast sand sample in Figure 4.9, where uncertainties presented for both methods are high.

In the FSA method of analysis all the information is included in the spectrum in contrast to the choosing of regions of interest of prominent peaks in the WA. Ignoring the Compton continuum in the WA simply implies throwing away some counts that can be used for data analysis.

In order to minimise the inevitable self-absorption effects in an attempt to obtain optimal results in this study, the cut-off energy of 300 and 400 keV, which gave best least square fit were therefore chosen.

In future if more focus could be put on the absorption effects at low energies for the FSA method, then the accuracy and precision of this technique could improve even further. Perhaps with the help of simulations from software programs such as the Monte Carlo N Particle extension transport code (MCNPX), which the ERL has at the moment introduced, an effort could be made in the future to understand these effects even better.

Appendix A

A-1: Some Formulae for combining uncertainties

Type of equation from which Result R is to be calculated	**Formula for calculating the uncertainty ΔR**
$R = A \pm B$	$\Delta R = \sqrt{(\Delta A)^2 + (\Delta B)^2}$
$R = aA \pm bB$ Where a and b are constants	$\Delta R = \sqrt{(a\Delta A)^2 + (b\Delta B)^2}$
$R = A^p$ Where p is a constant	$\frac{\Delta R}{R} = P\frac{\Delta A}{A}$
$R = aA^p$ Where a and p are constants	$\frac{\Delta R}{R} = P\frac{\Delta A}{A}$
$R = A^p B^q$ Where p and q are constants	$\frac{\Delta R}{R} = \sqrt{\left(p\frac{\Delta A}{A}\right)^2 + \left(q\frac{\Delta B}{B}\right)^2}$

Table A1: the table shows some of the equations used in the calculation of the uncertainty ΔR, derivation from [Kno79].

A-2: Means and Standard deviation

The mathematical operation commonly applied to a set of measured or deduced values $x_i\,(i=1,2,...n)$ of a quantity X is to derive an average or mean value $\bar{x}$ and an estimate of the uncertainty of $\bar{x}$,s($\bar{x}$). If the values to be averaged have no associated uncertainties the arithmetic mean is simply given as

$$\bar{x} = \frac{1}{n}\sum_{i=1}^{n} x_i \qquad \text{(A1)}$$

or otherwise the average is calculated as the weighted mean

$$\bar{x} = (\sum_{i=1}^{n} w_i x_i) / (\sum_{i=1}^{n} w_i) \qquad \text{(A.2)}$$

were w_i is a weighting factor, defined as the inverse of the squared standard deviation.

If the parent distribution is a Gaussian or Poisson distribution and if the sample of the *n* values $x_{i,} x_2 ... x_n$ has been obtained from repeated measurements under identical measuring conditions, the arithmetic mean of equation (A1) is the best estimate of the expectation value m of the parent distribution. With increasing sample size n the arithmetic mean $\bar{x}$ approaches m.[Deb88].

The variance σ^2 of the parent ditribution is estimated by the experimental or sample varience

$$s^2(x) = \frac{1}{n-1}\sum_{i=1}^{n}(x_i - \bar{x})^2 \qquad \text{(A3)}$$

The relative standard deviation s(x) / $\bar{x}$ is also called the variation coefficient υ.

The experimental variance of the mean, $s^2(\bar{x})$, denoted by var($\bar{x}$), is smaller than $s^2(x)$ by a factor $1/n$ i.e,

$$s^2(\bar{x}) = \frac{s^2(x)}{n} = \frac{\sum_{i=1}^{n} (x_i - \bar{x})^2}{n(n-1)} \qquad \text{(A4)}$$

Many counting experiments produce only a single result, say N counts. In these cases we take N as the estimate of m. since $m = \sigma^2$ for a Poisson distribution, $\sqrt{N}$ is taken as experimental standard deviation s(N).

If we have a set of values x_i each of which has an associated variance $s^2{}_i$ and if these variances are not equal, the weighted mean defined in (A1) is a better estimate for m than the arithmetic mean. For the weighting factors the reciprocals of the variances are taken, i.e., $w_i = 1/s^2{}_i$.

The variance of $\bar{x}$ may be derived in two ways. The external variance is obtained in analogy to equation (A3) with weighting factors included; i.e.

$$s^2(\bar{x},1) = \frac{\sum_{i=1}^{n} w_i (x_i - \bar{x})^2}{(n-1)\sum_{i=1}^{n} w_i} \qquad \text{(A5)}$$

The internal variance, is

$$s^2(\bar{x},2) = \frac{1}{\sum_{i=1}^{n} w_i} \qquad \text{(A6)}$$

The magnitude of χ^2_R , the reduced chi-square, which is the measure of the goodness of fit to the data, is given by

$$\chi_R^{\,2} = \frac{1}{n-1}\sum_{i=1}^{n} w_i (x_i - \bar{x})^2 \qquad \text{(A7)}$$

where $\chi_R^{\,2}$ is expected to be of the order of unity for a perfect fit to the data [Deb88].

Appendix B: FORTRAN program

(program used for converting channel numbers to equivalent energy in keV)

```
c    Note that E = a + b * Ch   or Ch = E/b - a/b
c
c     therefore the channel that corresponds to energy i keV
c
c     is given by Ci=i/b - a/b
c             and C(i+1) = (i+1)/b - a/b
c     Here Ci and Ci+1 are floating point numbers.
c     When we transform to the integer value, one will still
c     get that Ci and Ci+1 may cover two or three channels.
c
c     change energy scale
c     note that n KeV is in ch n+1
       dimension eold(5000),ich(5000),countn(5000),cntnew(5000)

       open(unit=5,file='inputfile.txt')
       open(unit=7,file='outputfile.dat')
       do 50 i=1,7
c       read(5,*)
c  50  continue
c  read livetime
        read(5,45)time
   45      format (26x,le16.7)
             read(5,*)
       read(5,55) a
       read(5,55)b
       read(5,55)c
 55    format (55x,le16.7)
 c
       imax=4100
       write(*,*) imax,a,b,c
       do 70 k=1,4
       read(5,*)
 70    continue
       do 200 i=1,imax
       read(5,*)ich,countn(i)
 200   continue
       write(*,*)(iCH(i),eold(i),countn(i))
  300  continue

c now change the energy scale for b=0.6471

         newmax=imax*b+10

       do 1000 i=0,newmax
```

```
        Epold1=i/b - a/b
        Epold2=(i+1)/b - a/b
         Else
         Epold1=(-b+sqrt(b*b-4.*c*(a-i)))/(2.0*c)
         Epold2= (-b+sqrt(b*b-4.*c*(a-i-1.)))/2.0*c)
         endif
c
        j=int(Epold1)
        jp1=j+1
        jp2=j+2
        jp3=j+3
        jprime=int(Epold2)
        cntnew(i)=(jp1-Epold1)*countn(jp1)
c
        if ((jprime-j).eq.1)       then
            cntnew(i)=cntnew(i)+(epold2-jp1)*countn(jp2)
         else
c if it spans 3 channels
         cntnew(i)=cntnew(i)+countn(jp2)+(Epold2-jp2)*countn(jp3)
        endif

 1000   continue
c print
         do 2000 i=1,newmax
         write(7,*)i,cntnew(i)
 2000  continue
      end
```

Appendix C: Background Spectrum

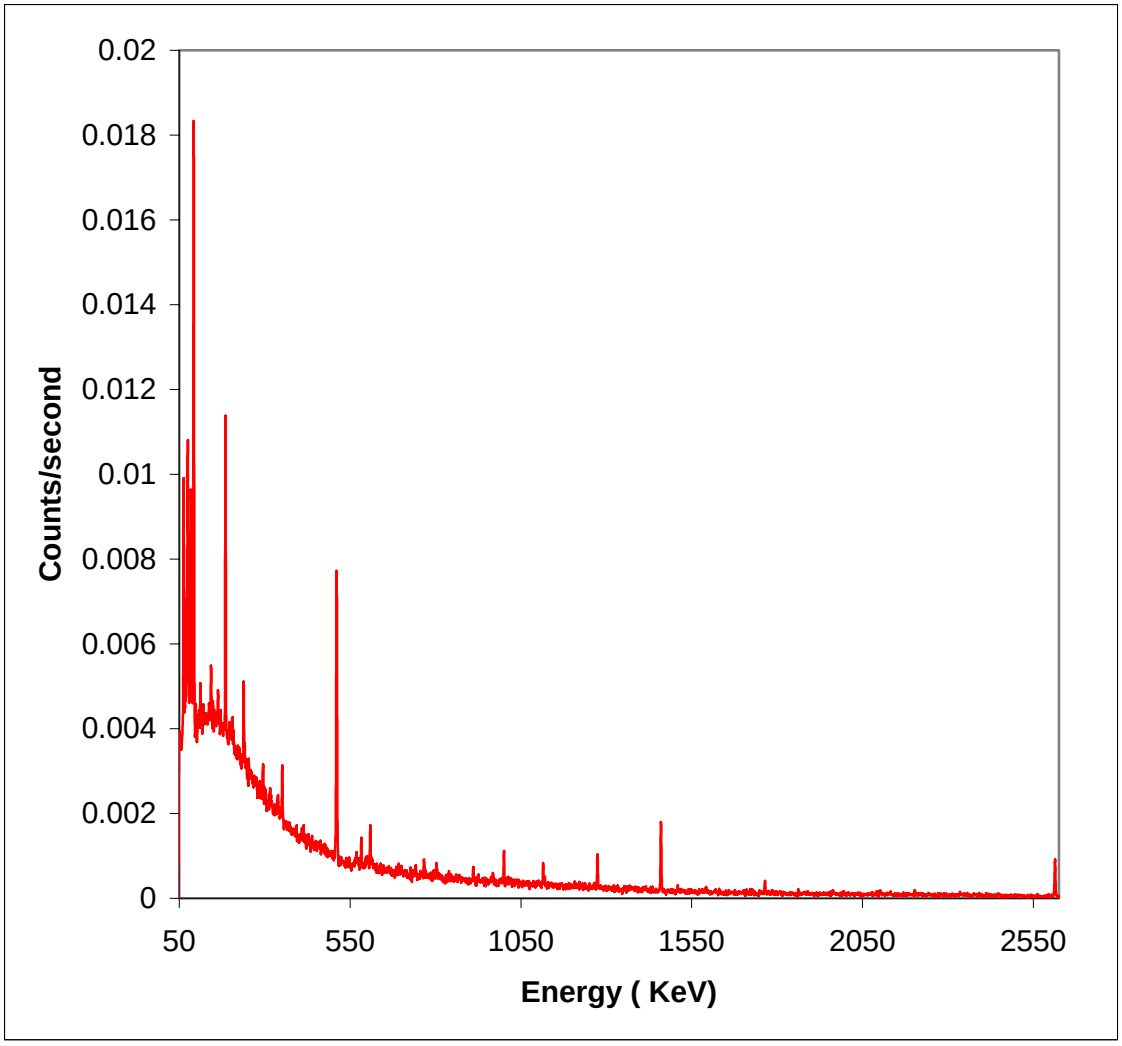

Figure C-1: The background spectrum used in this study. It was obtained by measuring a Marinelli beaker filled with tap water.

Appendix D: Self-absorptions effects (by Modelling of the γ-ray transmission through a Marinelli beaker)

According to the model developed by Sima [Sim92] and used here, the γ-ray transmission through a sample-filled Marinelli beaker can be calculated using the expression:

$$F_a(\mu) = \frac{1 - e^{-\mu t}}{\mu t} \qquad \text{(D.1)}$$

where F is the transmission factor which is a function of the γ-ray linear attenuation coefficient and the γ-ray energy ; t is the effective thickness (of the sample being measured) as viewed from a small, spherical detector. This detector is placed in relation to the Marinelli beaker as shown in Figure D.1. The model assumes the detector to be a spherical point.

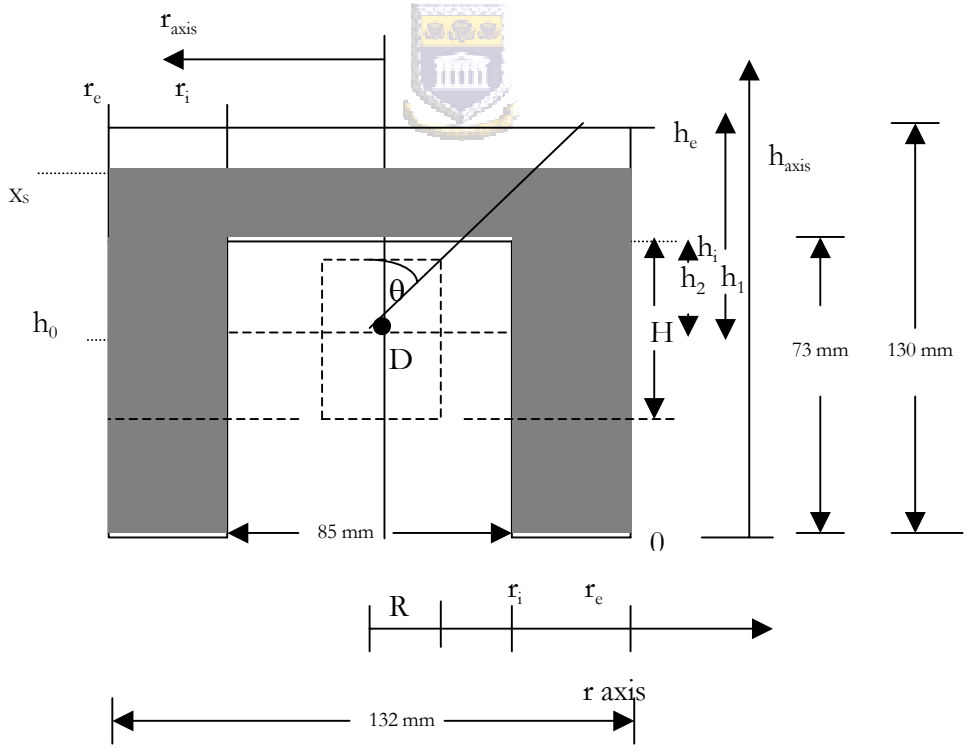

Figure D1: The Marinelli Beaker with a spherical detector model at the center.

The filling of the re-entrant hole h_e-h_i approximately equals the thickness r_e-r_i. This thickness was determined according to the model developed by Sima [Sim92], and the value of this thickness was recorded for different filling heights. These dimensions are tabulated in Table D.1.

The effective thickness, t, can then in principle be determined as follows:

$$t = \frac{\int l(\theta) d\Omega}{\int d\Omega} \tag{D.2}$$

where $l(\theta)$ is the thickness of the sample corresponding to the angle θ (see Figure D.1) and $\int$ denotes integration over the solid angle subtended by the sample.

Sima showed that t can then be calculated from the expression:

$$t = \frac{1}{\mathrm{P}}[f(r_e, h_1) + f(r_e, h_0) - f(r_i, h_2) - f(r_i, h_0)] \tag{D.3}$$

where

$$\mathrm{P} = \frac{\Delta\Omega}{2\Pi} \tag{D.4}$$

$$= 1 + \frac{h_0}{\sqrt{{h_0}^2 + {r_i}^2}} \tag{D.4}$$

with

$$f(r,h) = r\tan^{-1} g(h/r) + \frac{h}{2}\ln[(r/h)^2 + 1] \tag{D.5}$$

with *r* and *h* being the dimensions of the model Marinelli beaker shown in Figure D.1. The values of r and h for the Marinelli beaker used here are given in Table D.3. For a fully filled Marinelli beaker the effective thickness, *t*, of the sample was found to be 2.6 cm. The effective thickness for the beaker filled to 500 ml was also calculated (see Table *D.1*).

Volume of sand in Marinelli beaker (ml)	h_e= height of sand Marinelli beaker dimension (mm)	Effective thickness t (mm)
1000	111	25.9
500	73	15.9

Table D.1: Results of calculations of the effective thickness t for two Marinelli volumes.

γ-ray mass attenuation (μ/ρ)coefficients in various materials can be found in compilation of Hübbel [Hub82]. In the use of a generic compound XY, where X and Y are two different elements, one can calculate the attenuation coefficient for the sample using the expression:

$$(\mu/\rho)_{XY} = \frac{(\mu/\rho)_X}{(\mu/\rho)_X + (\mu/\rho)_Y)} + \frac{(\mu/\rho)_Y}{(\mu/\rho)_X + (\mu/\rho)_Y)} \qquad \text{(D.5)}$$

An example in this case is silicon oxide (SiO_2), which is a major constituent of soil. We used the Sima formula to calculate the transmission through a Marinelli beaker filled with water, KCl, generic sand, ^{232}Th and ^{238}U sources. Calculations were made from 50 keV to 2 MeV in steps of 50 keV. The assumed elemental composition of the ^{238}U and ^{232}Th are given in the

IAEA manual [RL148], however we assumed the SiO_2 to be the major constituent for these two elements.

The calculated transmission factors are shown in Table D.2.

Energy (keV)	Water		KCl Density 1.3 g/cm³		Sand Density 1.6 g/cm³		U (Source) Density 1.2 g/cm³		Th (source) Density 1.3 g/cm³	
	Mass attenuation (μ/ρ) in (cm²/g)	Transmission Factor F_{water}	Mass attenuation (μ/ρ) in (cm²/g)	Transmission Factor F_{KCl}	Mass attenuation (μ/ρ) in (cm²/g)	Transmission Factor F_{sand}	Mass attenuation (μ/ρ) in (cm²/g)	Transmission Factor $F_{U(source)}$	Mass attenuation (μ/ρ) in (cm²/g)	Transmission Factor $F_{Th(source)}$
50	0.2262	0.740	0.7568	0.345	0.3165	0.536	0.3165	0.611	0.3165	0.595
100	0.1707	0.794	0.2196	0.693	0.1682	0.704	0.1682	0.760	0.1682	0.749
200	0.137	0.830	0.1292	0.801	0.1255	0.766	0.1255	0.813	0.1255	0.804
300	0.1187	0.850	0.1066	0.832	0.1076	0.795	0.1076	0.837	0.1076	0.828
500	0.0969	0.875	0.0852	0.862	0.0874	0.828	0.0874	0.864	0.0874	0.857
800	0.0787	0.897	0.0688	0.887	0.0709	0.858	0.0709	0.888	0.0709	0.882
1500	0.0576	0.923	0.0503	0.915	0.0519	0.893	0.0519	0.916	0.0519	0.912
2000	0.0494	0.934	0.0436	0.926	0.0447	0.907	0.0447	0.927	0.0477	0.923

Table D.2: A table of the mass attenuation coefficients and the transmission factors.

Beaker Dimensions

r_e	r_i	r	h_i	h_2	h_e	h_1	h_0
66 mm	44.3 mm	48 mm	75 mm	37.5 mm	111 mm	73.5 mm	37.5 mm

Table D.3: *The dimensions of the full Marinelli Beaker used in the iThemba ERL; (for a half full Marinelli (500ml), h_e = 73 mm)*

Appendix E: Ratios of activity concentrations

Sample type	Nuclide	Long measurement activity concentration ratios (WA/FSA)	Short measurement activity concentration ratios (WA/FSA)
West Coast sand	^{40}K	0.97 ± 0.05	1.5 ± 0.2
	^{232}Th	1.6 ± 0.3	1.4 ± 0.2
	^{238}U	1.25 ± 0.08	7.4 ± 3.0
Westonaria sand	^{40}K	1.01 ± 0.02	0.86 ± 0.06
	^{232}Th	1.06 ± 0.06	0.7 ± 0.1
	^{238}U	1.13 ± 0.02	1.07 ± 0.02
Kloof mine Sand	^{40}K	1.01 ± 0.02	1.02 ± 0.06
	^{232}Th	1.06 ± 0.04	1.08 ± 0.1
	^{238}U	1.18 ± 0.02	1.17 ± 0.1
Brick clay	^{40}K	0.97 ± 0.03	1.00 ± 0.1
	^{232}Th	1.01 ± 0.06	0.93 ± 0.05
	^{238}U	1.04 ± 0.05	1.04 ± 0.05

Table E.1: The ratios of the activity concentrations (WA/FSA) and the associated uncertainties for samples used in the study. The ratios are shown for both short and long measurements.

References:

[Ame00] Amersham QSA catalogue (2000).

[Bei87] Beiser A.,*"Concepts of Modern Physics"*, fourth edition, McGraw-Hill Book Co., Singapore, (1987).

[Chu94] Chuma J.L., *"Physica Reference Manual"*, 4004 Wesbrook Mall, Vancouver, B.C., Canada V6T 2A3 (1994).

[Cre87] Creagh D.C., "*The Resolution of Discrepancies in Tables of photon Attenuation Coefficients"*. Radiation Physics proceedings of the International Symposium on Radiation Physics. University di Ferrara, Ferrara, Italy (1987).

[Deb88] Debertin K., Helmer R..G., "*Gamma - and X -Ray Spectroscopy with semiconductor detectors"*. Elsevier science publishers B.V., Amsterdam. (1988).

[Deb89] Debertin K. and Ren J.,*"Measurement of Activity of Radioactive Samples in Marinelli beakers"*. Nucl. Instrum. Meth. **278**: 541, (1989).

[Dem97] De Meijer R.J., Stapel C, Jones D.G., Roberts P.D, Rozendaal A., MacDonald W.G. "*Improved and New Uses of Radioactivity in Mineral Exploration and Processing"*, Explor. Mining Geology **6** :105-117; (1997)

[Dem98] De Meijer R.J., "*Heavy Minerals: From Edelstein to Einstein"*, J. Geochemical Exploration **62,** 81 (1998).

[Dry89] Dryak. P., Kovar P., Plchova L, Suran J., "*Correction for the marinelli geometry"*, J. Radioanal. Nucl. Chem., letters **135** 281 (1989).

[EML97] Environmental Measurements Laboratory, Dept. of Energy (USA), HASL-300,28th edition (1997).

[Eva55] Evans R.D.,"*The Atomic Nucleus"*, McGraw-Hill, New York (1955).

[Fel92] Felsmann M., Denk H.J., "*Efficiency Calibration of Germanium Detectors with Internal Standards",* J. Radioanal.Nucl. Chem. **157,** 47 (1992).

[Fül99] Fülöp M., *"Portable gamma spectrometers for environmental and industrial applications at the institute of preventative and clinical medicine in Bratislava"*, Bratislava, Slovakia, Industrial and environmental applications of nuclear techniques, report of a workshop held in Vienna, 7-11 September 1998, International Atomic Energy Agency (IAEA), (1999).

[Gar01] Garcia-Talavera M., Laedermann J.P., Decombaz M., Daza M.J., Quintana B., *"Coincidence summing corrections for the natural decay series in γ-ray spectrometry",* Journal of Radiation and Isotope **54 ,**769, (2001)

[Gil95] Gilmore G., Hemingway J.D, "*Practical gamma-ray spectrometry"*, John Wiley & Sons, New York (1995)

[Hew85] Hewitt P.G., "*Conceptual Physics"*, Fifth edition, City College of San Francisco (1985)

[Hen01] Hendriks P.H.G.M., Limburg J., de Meijer R.J., "*Full-spectrum analysis of natural gamma-ray spectra"*, J. Environmental Radioactivity **53,** 365 (2001).

[Hen03] Hendriks P. "*In-depth γ-ray studies"* Borehole measurements, Rijksuniversiteit Groningen, Published, Ph.D Thesis, (2003).

[IAE89] International Atomic Energy Agency, Measurement of radionuclides in food and environment (Technical report series No.295) (1989).

[ISO03] Draft international standard. ISO/Dis 18589-1, "*Measurement of radioactivity in the environment-soil-part 1"*, general guide and definition International Organisation for Standardisation (2003).

[Jos04] Joseph A.D., iThemba LABS, South Africa, (Private communication) (2004).

[Kno79] Knoll G.F., "*Radiation detection and measurement"*, John Wiley & Sons, New York (1979).

[Kno00] Knoll G.F., "*Radiation detection and measurement"*, third edition John Wiley & Sons, New York, (2000).

[Kra88] Krane K.S., "*Introductory Nuclear Physics"*, John Wiley & Sons, Inc , New York, 10158 (1988).

[Leo87] William R. Leo, "*Techniques for nuclear and particle physics experiments",* Springer-Verlag Berlin (1987).

[Lil01] Lilley J., "*Nuclear Physics*, *Principles and Applications",* John Wiley & Sons, New York (2001).

[Mal01] Maleka P.P., "*Calibration of germanium detector for applications of radiometric methods in South Africa",* University of the Western Cape, RSA. Unpublished M.Sc. thesis (2001).

[Mer97] Merril E., Thomas G., "*Environmental Radioactivity: from natural, industrial and military sources"*, fourth edition, Academic press, publishers San Diego (1997).

[Mil94] Miller K.M., Shebell P., Klemic G.A. "*In situ gamma-ray spectroscopy for the measurement of uranium in surface soils",* Health Physics **67,** 140, (1994).

[Par95] Park T.S., Jeon W.J., "*Measurement of Radioactive Samples in Marinelli Beakers by Gamma-ray Spectroscopy"*, Journal of Rad.Anal. and Nucl. Chem. **193** 133 (1995).

[Pre92] Press W.H., Teukolsky S.A.; Vetterling W.T., Flannery B.P., "*Numerical Recipes in Fortran"*, second edition, (1992).

[Qui72] Quittner P., *"Gamma-ray spectroscopy, with particular reference to detector and computer evaluation techniques",* Akademia Kiado, Budapest (1972).

[RL148] "*Preparation and Certification of IAEA Gamma Spectrometry Reference Materials"* RGU-1, RGTh-1 and RGK-1, AQCS Intercomparison Runs Reference materials, IAEA.

[Ral72] Ralph E. Lapp & Howard L. Andrews, *"Nuclear Radiation Physics*" fourth edition, Prentice- Hall Inc., Englewood Cliffs, New Jersey (1972).

[Sha72] Shapiro J., *"Radiation Protection"*, A guide for scientists and physicists, Harvard University press, Cambridge, Massachusetts (1972).

[Sim92] Sima O., "*Photon Attenuation for samples in Marinelli beaker geometry":* An analytical computation, Health Physics, **62**: 445, (1992).

[Sta97] Stapel C., Limburg J., de Meijer R.J, "*Calibration of BGO scintillation detectors in a bore – hole geometry"*, Nuclear Geophysics Division (NGD), Kernfysinch Versneller Instituut (KVI), Rijksuniversiteit, Gronigen (1997).

[USR98] Germanium detectors User's Manual, Canberra industries, 800 Research Parkway, Meriden, CT 06450 (1998).

[Van02a] Van Wijngaarden L.B., Venema R.J., De Meijer R.J., Zwasman J.J.G., Van Os G., Gieske J.M.J., "*Radiometric Sand-mud characterization in the Rhine-Meuse estuary part A. fingerprinting*", Geomorphology **43**, 87 (2002).

[Van02b] Van Rooyen T.J., Lecture notes *"The science of radiation protection"*, iThemba LABS, unpublished, (2002).

[Ven01] Venema L.B., de Meijer R.J., *"Natural radionuclides as tracers of the dispersal of dredge spoil dumped at sea"*, J. Environmental Radioactivity **55,** 221 (2001).

[Ver92] Verplancke J., "*Low-level gamma spectroscopy: low, lower, lowest",* Nuclear Instruments and Methods in Physics Research **312**, 174 (1992).

[www01] www.scescape.net/~woods/elements/potassium.html taken on 17/08/2004

[www02] www.doh.wa.gov/ehp/rp/air/Fact% taken on 4/09/2003